Flight Test Results for the Daedalus and Light Eagle Human Powered Aircraft

R. Bryan Sullivan   Siegfried H. Zerweckh

Flight Test Results for the Daedalus and Light Eagle Human Powered Aircraft

R. Bryan Sullivan **Siegfried H. Zerweckh**

Massachusetts Institute of Technology
Cambridge, MA

October 1988

Prepared for
Langley Research Facility

Grant NAG-1-836
"Low Speed Flight Research with the MIT
Daedalus and Light Eagle Aircraft"

Notice

This report documents work sponsored by the United States Government. Neither the United States nor its agents, the National Air and Space Administration, nor any of the contractors, subcontractors or their employees makes any warranty, expressed or implied, liability or responsibility for the accuracy, completeness, or usefulness of any information, or represents that its use would not infringe privately owned rights.

Preface

The Light Eagle and Daedalus human powered aircraft were designed and constructed by a group of students, professors, and alumni from the Massachusetts Institute of Technology within the context of the Daedalus Project. The construction of the Light Eagle and Daedalus aircraft was funded primarily by the Anheuser Busch and United Technologies Corporations, respectively, with additional support from the Smithsonian Air and Space Museum, the Massachusetts Institute of Technology, and a number of other sponsors. The flight research reported here was done at the NASA Dryden Flight Research Center between December 1987 and March 1988. Funding for these tests was provided under Grant NAG-1-836 from NASA Langley. Mr. John F. Royall was the NASA Technical Monitor; the contractor's Principal Investigator was Professor Jack L. Kerrebrock.

Abstract

This report describes the results of the flight test program of the Daedalus and Light Eagle human powered aircraft in the winter of 1987/88. The results from experiments exploring the Light Eagle's rigid body and structural dynamics are presented. The interactions of these dynamics with the autopilot design are investigated. Estimates of the power required to fly the Daedalus aircraft are detailed. The system of sensors, signal conditioning boards, and data acquisition equipment used to record the flight data is also described.

In order to investigate the dynamics of the aircraft, flight test maneuvers were developed to yield maximum data quality from the point of view of estimating lateral and longitudinal stability derivatives. From this data, structural flexibility and unsteady aerodynamics have been modeled in an ad hoc manner and are used to augment the equations of motion with flexibility effects. Results of maneuvers that were flown are compared with the predictions from the flexibility model.

To extend the ad hoc flexibility model, a fully flexible aeroelastic model has been developed. The model is unusual in the approximate equality of many structural natural frequencies and the importance of unsteady aerodynamic effects. Since no clear spectral separation between low-frequency and high-frequency modes has been identified, it is difficult to justify inclusion or exclusion of any particular mode.

The performance of the autopilot design is evaluated in light of the dynamics observed during the flight test program. Degradations in performance are observed when the flexibility effects are included; however, adequate performance can be achieved by proper augmentation of the feedback compensation.

Power measurements from the Daedalus 88 aircraft indicate that the power required to fly the aircraft actually decreases with altitude. This is opposite of the trend predicted by the classical ground effect theory; however, it does agree with subjective observations by Kanellos Kanellopoulos during his 119 km flight from Crete to Santorini, Greece and by Bryan Allen during his flight across the English Channel in the Gossamer Albatross. It is hypothesized that this inverse ground effect is caused by turbulence in the Earth's boundary layer. The diameters of the largest boundary layer eddies (which represent most of the turbulent kinetic energy) are proportional to altitude; thus, closer to the ground, the energy in the boundary layer becomes concentrated in eddies of smaller and smaller diameter. Eventually the eddies become sufficiently small (approximately 0.5 cm) that they trip the laminar boundary layer on the wing. As a result, a greater percentage of the wing area is covered with turbulent flow. Consequently the aircraft's drag and the power required both increase as the aircraft flies closer to the ground.

The results of the flight test program are examined critically, especially with respect to future applications. Maneuvers that allow the observation of stability derivatives for flexible aircraft are detailed. Considerations for the design of autopilots for future human powered aircraft and high-altitude RPV's are discussed. Techniques useful in estimating the power required to fly aircraft of very high lift to drag ratio are described.

Acknowledgements

The authors and the entire Daedalus Project are deeply indebted to John F. Royall of NASA Langley, and to Dr. Jack Kerrebrock, Dr. John Langford, Harold Youngren, Dr. Mark Drela, Dr. Steve Bussolari, and Dr. Andy von Flotow, all of MIT, for their support of this research.

The authors are deeply indebted to Jim Murray, Ken Iliff, and Richard Maine of NASA Dryden for their assistance with the flight tests, especially for providing the pEst analysis software and the expertise to use it prudently.

Special thanks go to Steve Finberg, Tom Clancy, and Tom Schmitter for their technical expertise that was invaluable in assembling the data acquisition system.

The success of the data acquisition system was due in part to Onset Computers for their loan of the onboard computer and to General Precision Industries for their loan of the rate gyros.

Finally, our deepest thanks to the entire team that devoted years to the painstaking construction of the Daedalus and Light Eagle aircraft. This research would truly have been impossible without your help.

This research was conducted under NASA Grant NAG-1-836.

Table of Contents

List of Figures

List of Tables

1.0 Introduction

Greek mythology describes a man, Daedalus, who, 3500 years ago, constructed wings of wax and feathers and used them to fly under his own power. With these wings, he escaped imprisonment under King Minos on Crete, Greece and flew northward past the island of Santorini. To celebrate this myth, the Daedalus Project began over three years ago with the goal of designing, building, and testing a human powered aircraft that could fly farther than 115 km. On April 23, 1988, the mythical flight route from Crete to Santorini was retraced by the Daedalus human powered aircraft, thus symbolizing the realization of Man's ancient dreams through modern technology.

On the way to this goal, three human powered aircraft were constructed. The Light Eagle was the prototype aircraft, weighing 92 pounds. It set a closed course distance record of 59 km on January 22, 1987. Following this success, two more aircraft were built, the Daedalus 87 and the Daedalus 88. Each aircraft weighed approximately 69 pounds. The Daedalus 88 aircraft was the ship that flew the 119 km from the Iraklion Air Force Base on Crete, Greece to the island of Santorini in 3 hours, 54 minutes. In the process, the aircraft set new records in distance and endurance for a human powered aircraft.

Research on the technologies of human powered flight, and education have been as important objectives of the Daedalus Project as the flight itself. To further these objectives, a flight test program was carried out at the NASA Dryden Flight Research Center between November 1987 and March 1988. The purpose of the flight test program was to expand the knowledge of human powered flight. Specific goals were to determine the power required to fly the Daedalus aircraft, to explore the dynamics of low Reynolds numbers aircraft and their autopilots, and to investigate the aeroelastic behavior of lightweight aircraft (Figure 1-1). The information attained in this program should have direct applications to the design of high altitude, long endurance aircraft.

© Steve Finberg

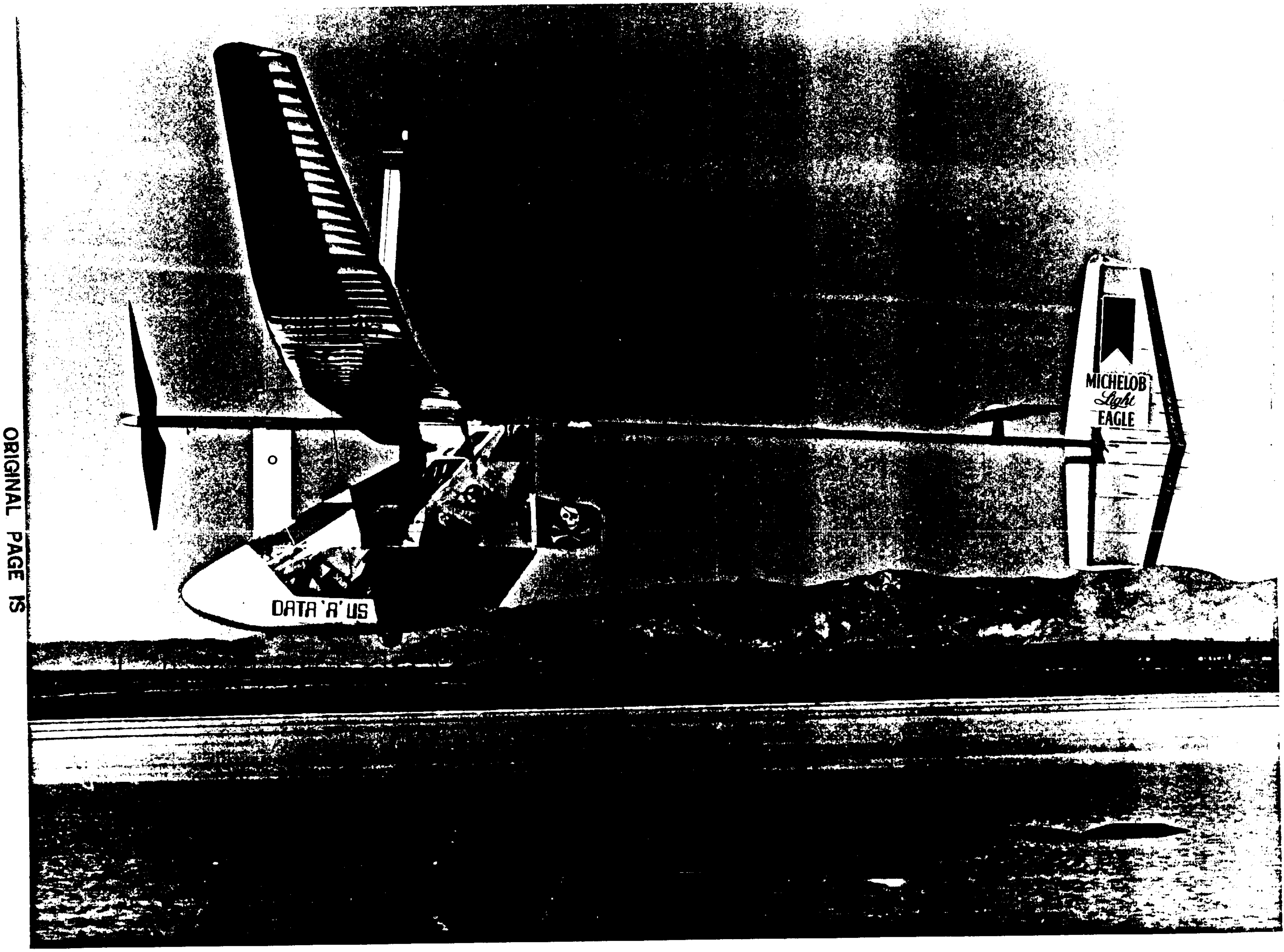

Figure 1-1 The Light Eagle During a Test Flight at the Dryden Flight Research Center

2.0 Flight Testing

The specific areas of flight research included characterizing the rigid body and flexible dynamics of the Light Eagle, investigating sensors for an autopilot that could be used on high altitude or human powered aircraft, and determining the power required to fly the Daedalus aircraft. The research flights started in late December 1987 with a shake-down of the Light Eagle instrumentation and the data transfer links. The first flight of the Daedalus 87 also occurred during this time. On February 7, 1988, the Daedalus aircraft crashed on Roger's Dry Lakebed due to inadequate lateral controllability which has subsequently been attributed to insufficient dihedral and excessive elasticity in the rudder control lines. This incident caused emphasis to be placed on determining the lateral stability and control characteristics of the Light Eagle in preference to the longitudinal dynamics. Due to the accident, flight testing was extended four weeks and thus ended in mid-March 1988 after having achieved the major goals of the program.

2.1 The Aircraft

2.1.1 Unique Features of the Light Eagle

The Light Eagle is an unique aircraft, as shown in Figure 2-1. Its design flight speed is approximately 7.8 m/s (15 mph, Re = 500,000 - 200,000), at a lift to drag ratio of 36. Its aspect ratio of 39.4 is one of the highest ever flown, yet the aircraft has a very low empty weight of 42 kg (88 lbs). The structure, based on graphite-epoxy spars, foam leading edge inserts, and a mylar skin, is designed as much by stiffness requirements as it is by strength requirements. Instead of a purely cantilevered wing structure, a lift wire runs from the half-span points to the bottom of the fuselage. This wire resulted from a compromise between

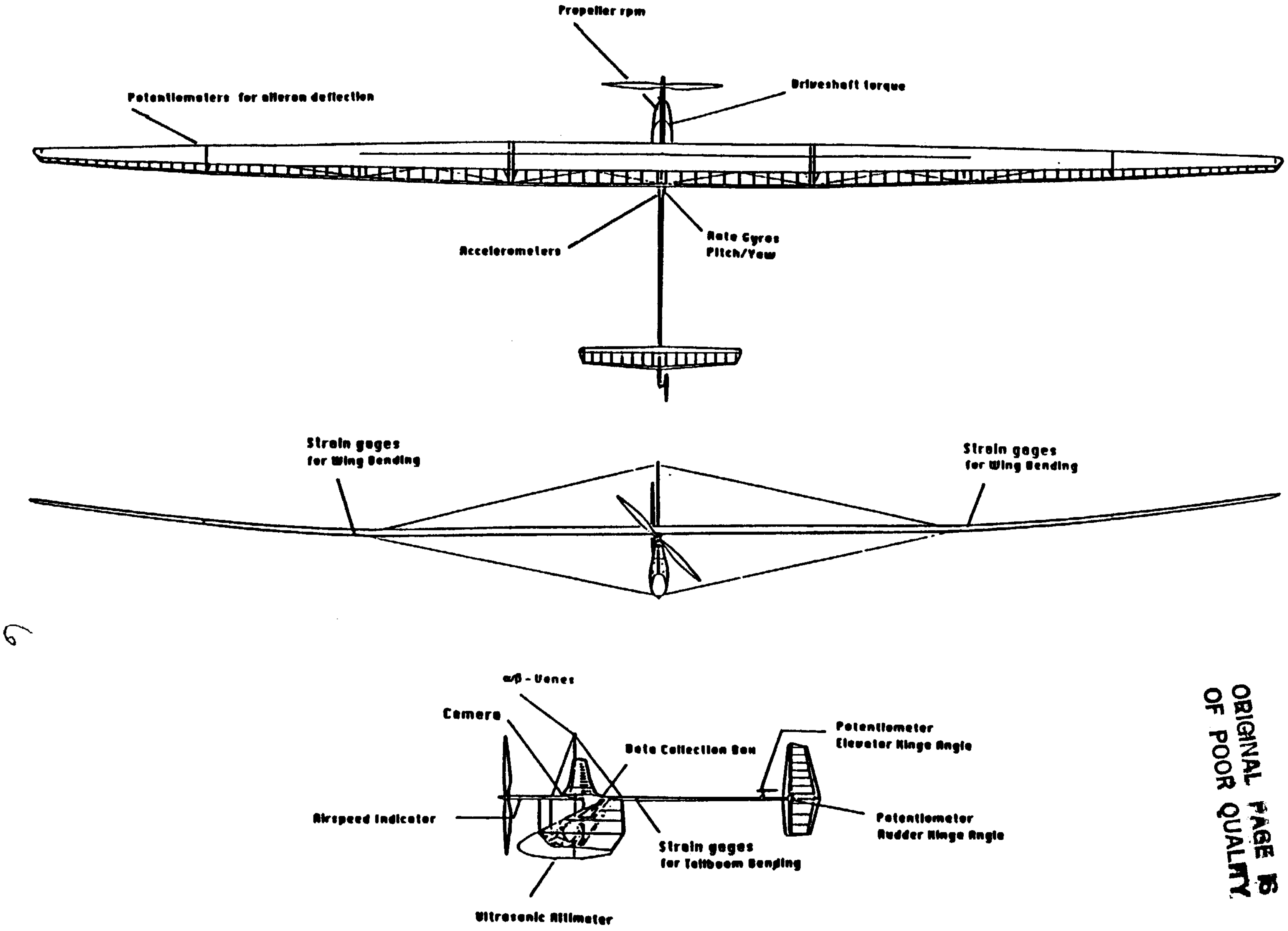

6

Figure 2-1 The Light Eagle

aerodynamic drag and structural weight. The power required to maintain level flight is approximately 200 W (0.27 Hp) when the aircraft's total weight is 110 kg (242 lbs). The characteristics of the Light Eagle are compared to those of the Gossamer Albatross and the Stork B in Table 2-1.

	Light Eagle	Gossamer Albatross II	Stork B
Wing Area (m^2)	31	44	21.7
Drag Area (m^2)	0.8	2.5	0.7
Wing Span (m)	34.7	29	21
Aspect Ratio	39.4	18.9	20.3
Empty Weight (kg)	42	32	35.9
Design Power (W)	225	246	275
Design Airspeed (m/s)	7.8	5.0	8.6

Table 2-1 Characteristics of the Light Eagle Aircraft

2.1.2 Pedalling Disturbances

The pilot is the aircraft's powerplant as well as the control unit. In his role as a powerplant, the pilot must pedal, moving his legs (perhaps 21 kg, or 20% of the gross aircraft weight) through a distance of approximately 40 cm.. The pedalling frequency is about 1.5 to 2 Hz, coinciding with a natural structural frequency (chordwise bending/torsion of the wing coupled with tailboom bending in the up-down direction). The pilot thus introduces a large periodic signal into all instrumentation channels, precisely in the frequency range of interest. For this reason, much of the flight testing was done during unpowered gliding flight, with the aircraft being towed to a certain altitude and then released.

2.1.3 Apparent Mass Effects

The Light Eagle flies with a wing loading of 37 N/m^2 (Table 2-2). The weight of the volume of air enclosed in a cylinder with its diameter equal to the wing chord and its length equal to the wingspan, is approximately twice the wing's structural weight. Apparent mass effects are thus large and must be consistently included in dynamic models. These effects have a large influence on the aircraft control, particularly in the lateral axis (Table 2-3).

High performance sailplanes	372 - 395 N/m^2
Trainer sailplanes	214 N/m^2
Hang Gliders	38 - 67 N/m^2
Light Eagle	37 N/m^2

Table 2-2 Wing Loadings of Different Aircraft

2.1.4 Aircraft Flexibility

Unloaded, the aircraft's wing spar is straight; however, equilibrium tip deflections during level flight exceed 1.4 m (4.6 ft), due almost entirely to wing bending near the liftwire attach point. This curved equilibrium shape must be taken as the reference configuration for linearized dynamic analyses. Coupling between chordwise bending and torsion is created by this curvature, leading to the potential of an unusual flutter mode involving chordwise motion [1,2].

The flexibility of the tailboom is very important for the coupling of lateral rigid-body modes and flexibility modes, and introduces a considerable time delay between control surface inputs and the corresponding response of the aircraft. Above a certain frequency, empennage control inputs have no effect on the overall motion of the aircraft and solely excite structural modes of the tailboom.

Fuselage with tailboom:	14.3 kg	(31.5 lbs)
Wing:	22.3 kg	(49.1 lbs)
Tail Surfaces:	1.7 kg	(3.8 lbs)
Reinforcements:	1.6 kg	(3.7 lbs)

Air mass / Length enclosed in the wing:	0.16 kg/m	(0.1 lbs/ft)
Wing mass / Length:	0.64 kg/m	(0.43 lbs/ft)

	Without Apparent Mass	With Apparent Mass
I_x	815.7 slugs ft^2	1596.9 slugs ft^2
I_y	82.9 slugs ft^2	138.6 slugs ft^2
I_z	849.8 slugs ft^2	1185.8 slugs ft^2
I_x	11057 kg m^2	21648 kg m^2
I_y	1124 kg m^2	1879 kg m^2
I_z	11520 kg m^2	16070 kg m^2

Table 2-3 Light Eagle Mass and Inertias

The natural frequencies of the aircraft's structural modes are comparable with the rigid-body estimates of the short-period and the dutch roll modes. One must thus expect that flexibility plays a large part in the aircraft's dynamic response and contributes to aeroelastic behavior [3]. These effects are described in more detail in the following chapter.

2.1.5 Unsteady Aerodynamics

The chord-based reduced frequency is $k = \omega c/u = 0.63$, corresponding to a frequency of 1 Hz, a flight speed of 8 m/s, and a chord of 0.8 m. This implies that unsteady aerodynamic effects will also play a major role in the dynamic response of the aircraft for all motions above approximately 0.1 Hz. This frequency is well within the pilot's bandwidth, and within the spectrum of the control inputs used during flight testing.

2.2 Instrumentation

The goals of the flight test program were to investigate the rigid body and structural dynamics of the Light Eagle, to evaluate sensors and actuators for the autopilot, and to determine the power required to fly the Daedalus aircraft. To accomplish these goals, it was necessary to assemble a Data Acquisition System (DAS) to fly onboard the aircraft. The system requirements for the DAS and the sensors were unique due to the small weight allowable and low power available; the entire system weighs approximately one kilogram. Figure 2-2 illustrates the size and complexity of the system.

2.2.1 Flight Critical Sensors

To allow the pilot to safely and efficiently fly the aircraft, an airspeed indicator and an altimeter were placed onboard the aircraft. The airspeed was sensed by measuring the rotation rate of a 7 cm diameter windmilling propeller located just aft of the aircraft's main propeller. Since the airspeed prop was located near the hub of the main prop, the effect of the main propeller's wash on the rotation rate of the airspeed prop was minimized. A small Samarium-Cobalt magnet was embedded in each blade of the airspeed prop. As the magnet moved past a Hall-effect sensor, a pulse was generated and sent through a coaxial cable to the processing electronics in the cockpit. These electronics converted the frequency of the pulses into a voltage representative of the airspeed of the aircraft (0.1V = 1.0 knot). This voltage was then

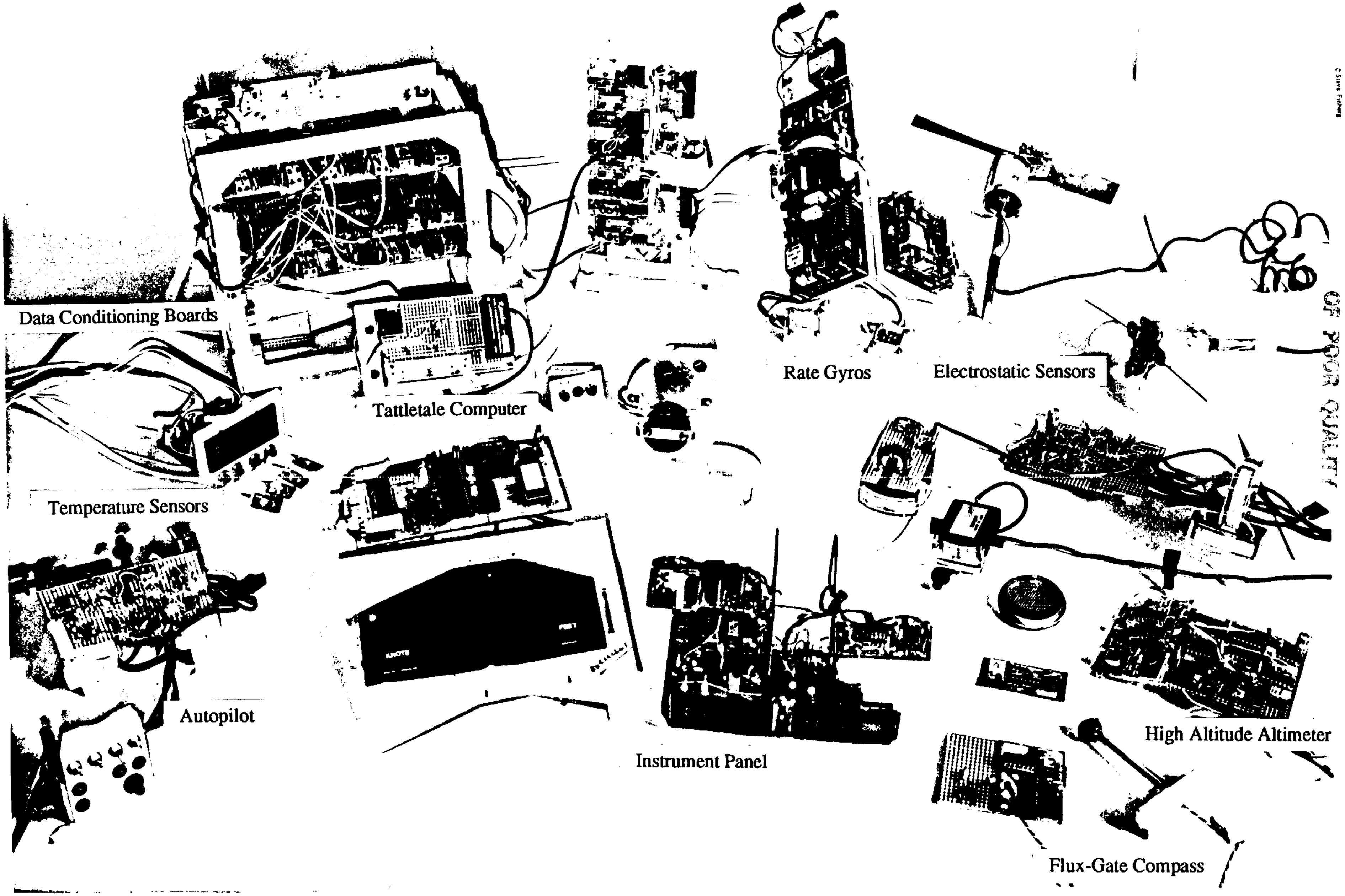

© Steve Finberg

Figure 2-2 Data Acquisition System and Sensors displayed digitally on an Acculex DP-650 LCD panel meter display located in the forward section of the cockpit.

The altitude was measured by a modified Polaroid ultrasonic rangefinder. The sensor generates a burst of ultrasonic sound that propagates through the air, bounces off the surface of the Earth, and returns to the aircraft. The length of time that this process takes is measured and is used as an estimate of the range to the ground. With the present configuration, altitudes of up to 12 meters can be reliably measured with a resolution of 7.5 cm. The output of this sensor was also displayed digitally on an LCD panel meter in the cockpit (0.1V = 1.0 ft).

A second, "high altitude", version of the altimeter was also constructed. Two of the Polaroid sound generating and receiving antennae discs were driven in parallel to produce a more powerful sound pulse. This sensor was ground tested to a range of 24 meters and had a resolution of 15.0 cm. Unfortunately time did not allow this sensor package to be installed and tested on the aircraft.

2.2.2 Inertial Instruments

To support the various dynamics experiments in the flight test program, two rate gyros and two accelerometers were installed in the aft instrument bay of the fuselage.

For experiments investigating the aircraft's lateral dynamics, the sensitive axes of the rate gyros were oriented to measure roll rate and yaw rate. For experiments investigating the longitudinal dynamics, one of the gyros was oriented to measure the aircraft's pitch rate. The gyros were supplied by General Precision Industries and were their Model QRS-10 solid state quartz rate gyros. They are characterized by a 180 deg/hr bias uncertainty, a temperature sensitivity of 6 deg/hr/deg F, and a hysteresis of 14 deg/hr. The outputs of the gyros were fed into high precision integrators that provided estimates of the pitch, roll, and yaw angles.

Though the steady state gyro bias was removed from the output of the gyros, the thermal sensitivity and hysteresis effects in the sensors unfortunately prevented the desired accuracy from being realized in the angle estimates.

Two accelerometers were installed in the aft instrument bay of the cockpit. The vertical accelerometer had a range of ±2 g's and the sideforce accelerometer had a range of ±0.5 g's. Since the accelerometers were not located at the aircraft's center of gravity, the data from the accelerometers were post-processed to remove the effect of the moment arm between the aircraft's center of gravity and the input axes of the accelerometers.

2.2.3 Flow Direction and Surface Position Sensors

To support the measurement of the dynamics of the aircraft, the angle-of-attack (AOA), the sideslip, and the deflections of the control surfaces had to be measured in flight. The AOA and the sideslip were measured by vanes mounted on the top of the wing support mast. This mast is at the quarter-chord of the wing and extends approximately 1.8 meters above the wing's surface. This location was selected since it minimizes the effects of the prop wash on the AOA and sideslip vanes; however, this location does not remove the vanes from the upwash of the wing. As a result, the AOA measurements are slightly exaggerated.

The vanes were constructed of balsa and basswood, sealed to prevent warpage. A steel shaft connected the vane to a 5K potentiometer that was used to indicate the position of the vane with respect to the aircraft. During flight tests it was found that the AOA signal was noisy and the sensor was replaced by a small AOA vane supplied by NASA.

The deflection of the elevator and rudder were measured with 10K potentiometers mechanically connected to the control surfaces through three-bar linkages. The position of one of the ailerons was measured using a spring-loaded potentiometer. A cable was wrapped around a drum on the shaft of the potentiometer. As the aileron was deflected, the cable was pulled off the drum, thus causing the shaft of the potentiometer to rotate. As the aileron returned to the undeflected position, the spring-loaded shaft rotated back to its original position and pulled the cable back onto the drum.

2.2.4 Structural Sensors

The goal of the structural tests was to characterize the flexibility modes of the aircraft's tailboom and wing. To sense the modes of the tailboom, two full bridges of 350 Ohm strain gages were used to measure the tailboom's pitch and yaw bending moments. These gages were located just aft of the fuselage-tailboom attach point. To reduce the noise in the strain gage signals, small preamplifiers were constructed and located near each bridge. The entire assembly was then encased in a balsawood and plywood compartment to minimize thermal effects on the strain gages and to prevent damage during ground handling of the aircraft.

A set of two full bridges of 350 Ohm strain gages was mounted on the wing spar just outboard of the lift-wire attach point. These sensors provided measurements of the wing bending moment at these points. Preamplifiers were also located near these strain gages to minimize the effects of the noise induced in the long wires back to the data acquisition system.

During several tests, an 8mm video camera was mounted on the upper fuselage tube just forward of the wing's leading edge. A wedge shaped mirror was then positioned aft of the camera such that the reflection of each wingtip could be seen by the camera. The motion of the tailboom and the deflections of the rudder and elevator could be observed by the camera under the bottom of the mirror. Small squares of reflective tape, approximately 2 cm square, were placed at various stations on the rudder, elevator, and wing, to allow their motions to be observed more precisely in the videotape.

2.2.5 Autopilot System

A number of sensors were evaluated to determine the feasibility of using them in an autopilot for human powered and high-altitude aircraft. These sensors included solid state rate gyros, electrostatic sensors, and a magnetic compass. The gyros and electrostatic sensors were used to estimate the attitude of the aircraft, specifically pitch and roll angles. In an autopilot, they would be used in the inner stabilization loop of an airspeed and wing leveling control loop. The magnetic compass that was tested would allow the autopilot to sense and control deviations from the desired heading.

The electrostatic sensors were an outgrowth of work done by Maynard Hill [4]. Hill's sensors consisted of a metal strip surrounded by a region of ionized air. The air was ionized by placing a radioactive source on the wing upwind of the metal strip. These sensors were attached to each wingtip of a model aircraft and their outputs connected to a high impedance differential op-amp. If the aircraft rolled, one sensor would be at a higher altitude and therefore at a lower voltage potential in the Earth's electric field than the other sensor. The op-amp would detect and amplify the voltage potential between the two sensors and would thus provide an analog indication of the roll angle.

One problem with this scheme is that the gradient of the Earth's electric field can change drastically from day to day. Unless this gain change is accounted for, the autopilot can saturate or possibly can be driven unstable. To circumvent this problem, a modified system was tested on the Light Eagle. Instead of attaching the sensors to the wing, they were attached to each tip of a small windmilling propeller that extended forward of the wing on a small boom. Rather than measuring the voltage potential between the two sensors, the electronics were configured to detect when the two sensors were nulled. This condition occurred only when the windmilling prop was level. A Hall effect sensor was used to detect the passage of a small magnet attached to the prop. The phase angle between where this magnet was detected and where the sensor's null occurred was equal to the roll angle of the aircraft. A similar sensor was configured to measure pitch angle, except the propeller used here had its axis of rotation perpendicular to the airflow (similar to an anemometer).

A magnetic compass, with no moving parts, was also constructed and tested on the aircraft. The compass compares the magnitude of the magnetic flux through two orthogonal coils and uses this information to estimate the direction of North. The autopilot was designed such that it would attempt to maneuver the aircraft to keep the sensor pointing North at all times. The pilot could rotate the coils in flight, thus allowing him to define his desired heading relative to North.

A set of autopilot actuators was tested on the Light Eagle. These actuators were simply small servos for radio controlled aircraft. On the Light Eagle, they drove trim tabs on the trailing edges of the rudder and elevator that in turn caused the rudder or elevator to move. The linkage between the servo and the trim tab was such that the position of the servo arm directly corresponded to a given deflection of the rudder or elevator. Thus the servo actually commanded the surface's position, not the surface's rotational velocity. This linkage is illustrated in Figure 2-3.

This actuator system was first demonstrated in ground tests. The elevator was attached to a beam and held above a pickup truck as the truck travelled at flight speed. Commands were then sent to the actuator thus causing the trim tab and hence the elevator to move. The dynamics of the surface in response to a change in the trim tab position resembled that of a first order system with a natural frequency of 11.4 rad/sec, a damping ratio of 0.7, and a time lag of 0.1 seconds.

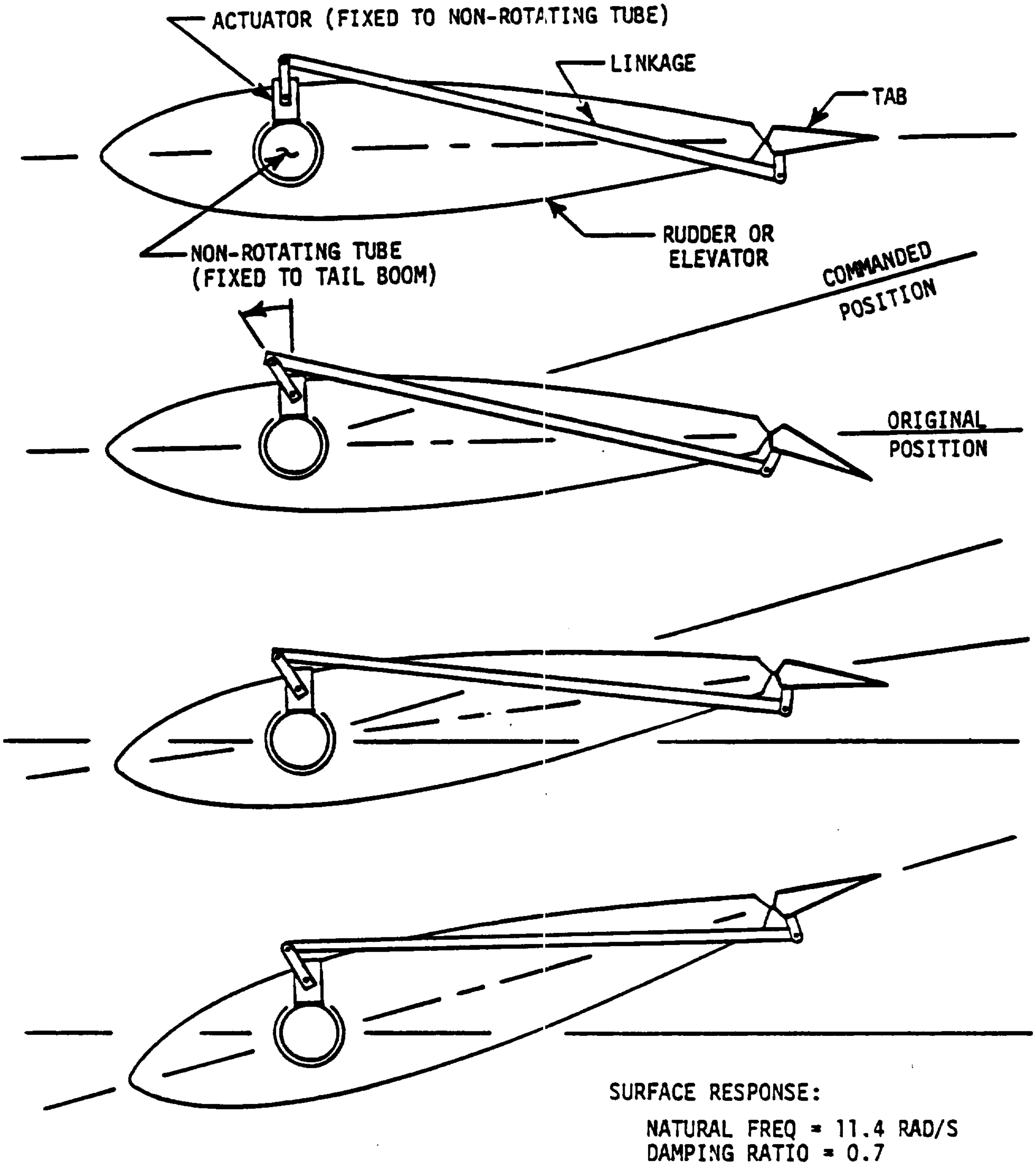

Figure 2-3 Actuator Linkage

The commands from the cockpit to the actuators were transmitted over a fiber optic cable to protect against electromagnetic interference. The system worked well in flight and in fact was used during some high altitude tow tests to set and hold the trim condition of the aircraft.

2.2.6 Sensors for Power Measurement

One of the prime objectives of the flight test program was to measure the power required to fly the Light Eagle and the Daedalus aircraft. These data were necessary to proceed with plans to attempt to fly the Daedalus aircraft 119 km. To measure the power that the pilot must supply, the torque on and the RPM of the driveshaft were measured and stored in the DAS. The torque was measured through a half bridge of 120 Ohm strain gages mounted on the driveshaft 45 degrees off the tube's axis of rotation. A small preamplifier was mounted on the rotating tube and was used to boost the strain gage signals before they were sent through slip rings and on to the DAS. The rotation rate of the driveshaft was estimated by recording the voltage across a generator that was rotated by the driveshaft. When the rotation rate and the torque measurement were combined during post-flight processing, the power being put into the drive system could be estimated.

A second means of determining the power required to fly the aircraft was to measure the pilot's heart rate with a small sensor made by AMF. The unit stored the pilot's heart rate as a function of time and allowed the time history to be downloaded into a computer for post-flight analysis.

2.2.7 Temperature Sensors

One of the concerns for making long duration flights in the Daedalus aircraft was that the pilot might overheat in the enclosed cockpit. To test the heating that could be expected, four thermistors were placed at various locations in the cockpit. The signals from each thermistor were amplified and displayed as temperatures on an Acculex LCD digital panel meter. Because of the low bandwidth required in this data, the data were not stored in the DAS but rather the pilot simply read the temperatures off the LCD display and radioed them to the support crew on the ground.

2.2.8 Data Acquisition System

To record the signals from the sensors distributed throughout the airframe, a Data Acquisition System (DAS) was assembled. The outputs of each of the sensors were filtered and then stored in a Tattletale data acquisition computer.

One of the important aspects of the flight instrumentation system was the short period of time between data acquisition and data processing. After each flight, the data were downloaded from the on-board computer onto floppy disks in an IBM compatible personal computer in the support van. After flight tests were concluded for that day, typically around 10:00 AM due to wind and thermal activity, the data were read off the floppy disks by a Compaq DeskPro 386. The data were then transferred through Ethernet onto NASA's mainframe computer. During that afternoon, the data were processed with a NASA parameter estimation program called pEst and by evening, preliminary estimates of the parameters were available, along with plots of the maneuvers flown that morning. This information allowed precise planning for the objectives of the following day's flight tests. It also allowed quick optimization of the maneuvers that would best highlight the data being sought. The pilots could then be briefed on the new or modified maneuvers that they would perform in the morning and could practice the maneuvers on the flight simulator.

This system allowed over 150 test flights to be made in three months with all of the preliminary data analysis being completed in this time.

Due to the stringent cost, weight, and power restrictions on the data collection system, no off-the-shelf DAS systems were found that could meet the requirements. However, a small computer, called a Tattletale, was acquired and proved to serve quite well as the onboard computer. A set of custom data conditioning boards were then constructed to act as an interface between the sensors and the Tattletale.

2.2.8.1 Data Conditioning Boards

During planning stages for the flight test program, it was estimated that potentially up to 40 sensors could be placed onboard the aircraft. The output from these 40 sensors had to be buffered and multiplexed before they could be stored in the Tattletale computer. To accomplish this task, a set of four conditioning boards was designed and constructed. Each board was identical, thus simplifying construction while also allowing repairs to be made in the field simply by swapping out defective boards.

Each card could receive and process the signals from up to 10 sensors with each sensor connected into the board by way of a 5 pin connector. One of these pins connected the sensor to ground and another pin connected it to the reference voltage. A third pin carried the output of the sensor while two of the pins were unused. The sensor's output entered the board through the connector and then passed through a ferrite bead that attenuated the noise induced in the long cable runs to the sensors. The output was then passed through a 5 Hz first order low pass filter. For eight of the channels on each board, the gain of this filter could be changed simply by turning trimming potentiometers. For the two other channels, both the gain and offset of the sensor's output could be changed by the trimming potentiometers. Thus each sensor's output could be scaled to maximize the sensitivity of the data and to minimize the quantization effects.

On each conditioning card, the outputs of these low pass filters were then fed into 2 multiplexers whose addresses were selected by the DAS computer. The multiplexers on each card were driven in parallel, thus the Tattletale had 8 analog signals coming into it, two from each of the four data conditioning boards. The Tattletale then used its internal multiplexer to select which of these 8 channels to connect to its A/D. By using this architecture, each sensor could be calibrated prior to the flight and its gain and offset values recorded for post-processing of the data.

The set of four conditioning boards plugged into a motherboard that was mounted in a balsawood cardcage located in the aft instrument bay of the cockpit. The Tattletale computer was connected to the motherboard through a ribbon cable.

2.2.8.2 Tattletale Data Collection Computer

The Tattletale computer, made by Onset Computers, is an extremely compact, yet relatively powerful computer. The unit measures only 12. x 6.7 x 3.6 cm and consists of a microprocessor, 512K of RAM, a 10 bit A/D, and a UART for communication with peripherals. A number of output lines on the computer are available for controlling external devices. The Daedalus DAS used four of these lines to drive the multiplexers on the data conditioning boards.

The Tattletale microprocessor runs BASIC and assembly language programs that are uploaded from a personal computer. To maximize speed, most of the data acquisition software was written in assembly code. This allowed the computer to receive and store 17 channels of 8 bit data at 20 Hz. The 20 Hz rate was used throughout the flight test program, since it minimized aliasing of the data. (Recall that the filters on the data conditioning boards had a 5

Hz break frequency). During measurements of the pilot's power output, the driveshaft torque and RPM signals were filtered at 15 Hz and recorded at 50 Hz (8 bit data).

Once the aircraft landed, the data were downloaded through the Tattletale's 9600 baud modem into a portable PC. The amount of download time was approximately equal to the flight time, typically around 10 minutes. Operationally this was not a significant problem; the data were downloaded as the pilot was being briefed on the next set of maneuvers and as the aircraft was readied for its next flight.

A DAS control panel was positioned in the forward cockpit which allowed the pilot to start the data acquisition process when the flight began. A flashing LED informed the pilot that the DAS was indeed taking data. When the tests were complete, the pilot would push the button again, the LED would stop flashing, and no more data would be taken. If the computer's memory was full, a second LED would inform the pilot to abort the test to allow the memory to be downloaded.

2.2.9 Additional Use for the Data Acquisition System

One unexpected use of the DAS was to investigate the crash of the Daedalus 87 aircraft on February 7, 1988. After the crash, flights in the Light Eagle and the Daedalus 88 highlighted factors that restricted the controllability of the Daedalus 87 during its crash. Changes were then incorporated on the Daedalus 88 ship, thus improving its controllability and providing additional margin against a mishap occurring during the flight in Greece.

2.3 Flight Test Maneuvers

The Light Eagle typically flies at 3-4 m (10-16 ft.) altitude and is designed to operate over a narrow speed range of 6.6-9.1 m/s (13-18 mph). Within this envelope, a set of flight test maneuvers was defined with which the aircraft's stability derivatives and structural dynamics could be observed. Because the aircraft is marginally powered and has a fairly small structural safety margin, the flight test maneuvers were severely constrained by safety and operational considerations. This led to the emphasis on small-perturbation maneuvers. Fortunately the limitations on the maneuvers did not significantly limit the usefulness of the data since most of the dynamics models are based on locally linearized models of the aircraft's aerodynamics. Large maneuvers exceed the range of these linearized models and thus necessitate the use of non-linear aerodynamic and structural models which are much more difficult to work with.

Table 2-4 is a presentation of the flight test matrix with the highest priority flights listed in the first column (unpowered towed flights).

	Unpowered Towed Flights	Powered Flights 15 mph	Powered Flights 18 mph	Long Liftwire	Short Liftwire
elevator doublet	2 Hz	2 Hz	2 Hz		*
rudder doublet	2 Hz	2 Hz	2 Hz	*	
aileron doublet	0.5 Hz	0.5 Hz	0.5 Hz		*
elevator freq sweep	0 - 3 Hz	0 - 3 Hz	0 - 3 Hz		*
rudder freq sweep	0 - 3 Hz	0 - 3 Hz	0 - 3 Hz	*	*
aileron freq sweep	0 - 1 Hz	0 - 1 Hz	0 - 1 Hz		*
dutch roll (rudder / aileron doublet)	1 Hz	1 Hz	1 Hz		*

Table 2-4 Flight Test Matrix

All test flights were conducted in the early morning in an attempt to avoid turbulence and thermal activity. Thus, time available for flight testing was limited to about three hours every morning. The effects of solar heating on the lakebed became significant after about 10:00 AM, contaminating mostly the angle-of-attack data. The data sets used for parameter identification generally were taken on extremely calm and overcast days.

2.3.1 Longitudinal and Lateral Dynamics

The aircraft's longitudinal dynamics include the short-period and phugoid modes, as well as tailboom bending and symmetrical wing bending modes. These modes can be easily observed with an elevator doublet. In general the exact shape of the doublet is unimportant, but for best excitation and a reasonable signal-to-noise ratio, the pulse duration should approximately equal the natural periods of the short-period mode and the tailboom flexibility mode. Large longitudinal pulses can result in significant flight condition changes and are thus unacceptable for use with the small-perturbation theory.

The Daedalus and the Light Eagle aircraft also exhibit the usual lateral-directional modes: Dutch roll, roll-convergence, and spiral-divergence. The optimum technique for exciting all of these modes is to use both aileron and rudder inputs. It is certainly possible to excite all the modes with aileron input only or with rudder input only; however, these approaches require careful design and execution of the desired input. In the experiments on the Daedalus and Light Eagle aircraft, the lateral-directional inputs consisted of simple rudder doublets combined with aileron doublets.

2.3.2 Steady Turns

The main purpose of flying steady-state turns was to observe the sideslip angle during the turns. Preliminary test flights indicated that the steady-state sideslip angle during turns was much higher than predicted. This contributed to the Daedalus 87 accident since the higher sideslip angles reduced the rudder's control authority.

The steady-state turns were flown with two different dihedrals (4 degrees and 9 degrees) and with two different control schemes. First, only the rudder was used to make the turn and later, both rudder and aileron were used. By comparing the resulting maneuvers, it was determined that with sufficient dihedral, ailerons were not necessarily more effective than the rudder for the execution of steady-state turns. Figure 2-4 demonstrates the controllability of the aircraft during a steady-state turn with rudder only. (The notation used in the plots of the flight data is listed in Table 2-5). Starting at 4 seconds, the aircraft establishes an almost constant yaw rate of 3 deg/sec. The roll angle and the sideslip angle build up steadily until at 16 seconds, a steady turn is established with a constant rudder setting of approximately 3 degrees. The sideslip angle builds up gradually and remains constant during the turn, at approximately 12 degrees.

2.3.3 Control Surface Pulses and Doublets

Control surface pulses and doublets were introduced into the elevator, rudder, and aileron to excite the dynamics of the aircraft. Tests with the Light Eagle's rudder and aileron were of particular interest because the Daedalus aircraft did not have ailerons and therefore needed to be controllable in the lateral axis with rudder only. Figure 2-5 shows the time history of an aileron doublet followed by a rudder doublet. The aileron doublet starts at 5 seconds and ends at 13 seconds. It is followed by a rudder doublet that lasts 5 seconds. The other two time histories show the fuselage's yaw rate and roll rate in response to these control inputs. The plots demonstrate the significant adverse yaw rate (4.0 deg/sec) and the relatively slow roll rate (-1.0 deg/sec) due to an aileron deflection. Note that an aileron deflection causes

ALT : altitude; [ft]

ALPHA : angle-of-attack; [deg]

AN : normal acceleration; [g]

AX : lonngitudinal accelleration; [g]

AY : lateral acceleration; [g]

BETA : angle-of-sideslip; [deg]

DA : aileron deflection; [deg]

DE : elevator deflection; [deg]

DR : rudder deflection; [deg]

LWING : strain gage signal, left wing up/down bending; [ft lbs.]

P : roll rate; [deg/sec]

Q : pitch rate: [deg/sec]

QBAR : dynamic pressure; [lbs./ft sec^{2}]

R : yaw rate; [deg/sec]

RWING : strain gage signal, right wing up/down bending; [ft lbs.]

TAILUP : strain gage signal, tailboom up/down bending; [ft lbs.]

TAILSIDE : strain gage signal, tailboom left/right bending; [ft lbs.]

V : airspeed; [ft/sec]

Table 2-5 Nomenclature for Flight Data

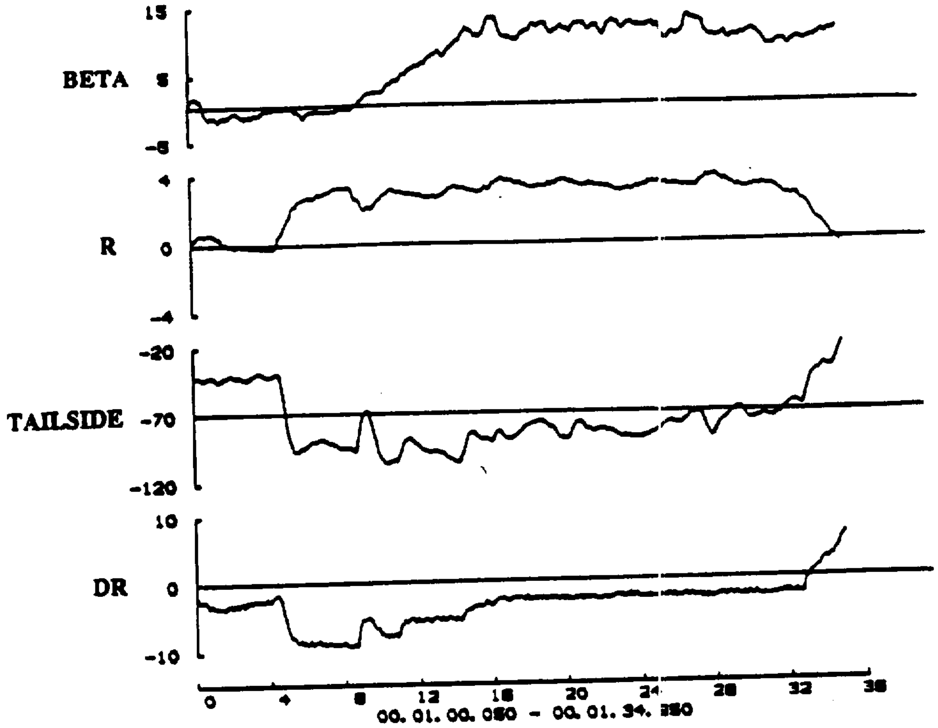

Figure 2-4 Steady-State Turn (Rudder Only)

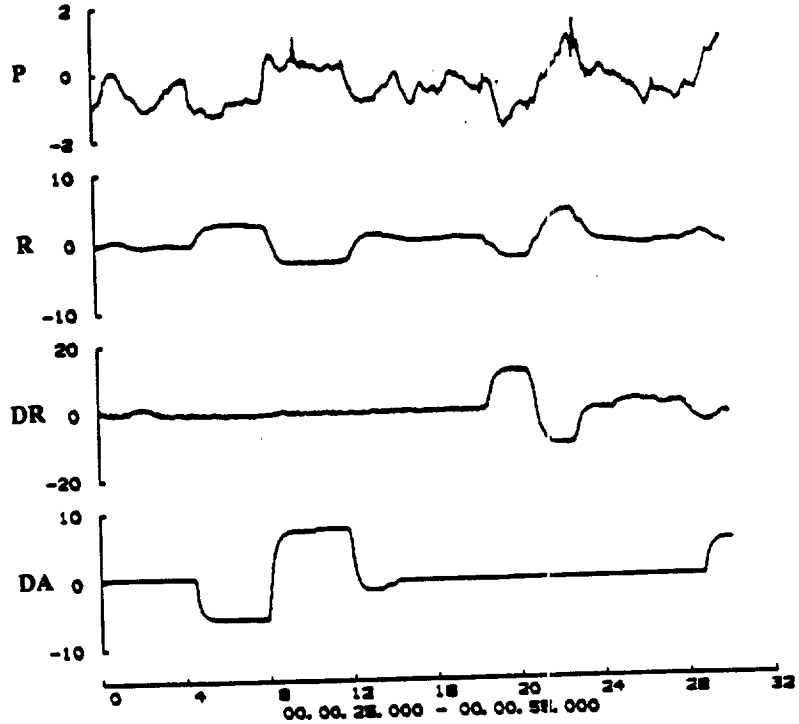

Figure 2-5 Aileron Doublet Followed by Rudder Doublet

the aircraft to initially yaw in the direction opposite of the desired turn while a rudder deflection causes the aircraft to enter an approximately coordinated turn.

Using the data from these maneuvers, stability derivatives were estimated by initially assuming a rigid-body aircraft model with quasi-steady aerodynamics. During the test flights it became obvious that the high flexibility of the aircraft's main structure, namely the tailboom and wing spar, invalidated the rigid-body assumption. Therefore, the equations of motion were then augmented to include flexibility effects by the introduction of a first-order filter between the control surface deflection and the application of the control torque. The data from the doublet maneuvers were used to estimate the parameters of the filter since these maneuvers highlight the time lag due to the tailboom flexibility effects.

2.3.4 Frequency Sweeps

Frequency sweeps with the elevator, rudder, and ailerons were also used to evaluate the interaction between the aircraft's rigid-body modes and flexibility modes. Test flights have shown that both the pitch (longitudinal) and the roll-yaw (lateral-directional) responses are significantly affected by the structural flexibility of the tailboom and wing.

Figure 2-6 shows an elevator frequency sweep starting at 12 seconds with a frequency of approximately 0.3 Hz, gradually increasing up to 1 Hz. The response from the accelerometers mounted in the fuselage follows the elevator excitation with little phase lag. However, from the wing bending moments at the liftwire attach point (RWING/LWING), it is clear that the outer wing motion due to high frequency elevator inputs is attenuated. This indicates that for low input frequencies, the rigid-body model may give acceptable results for control parameter estimation, whereas for high frequencies, a model that includes tailboom flexibility modes must be used.

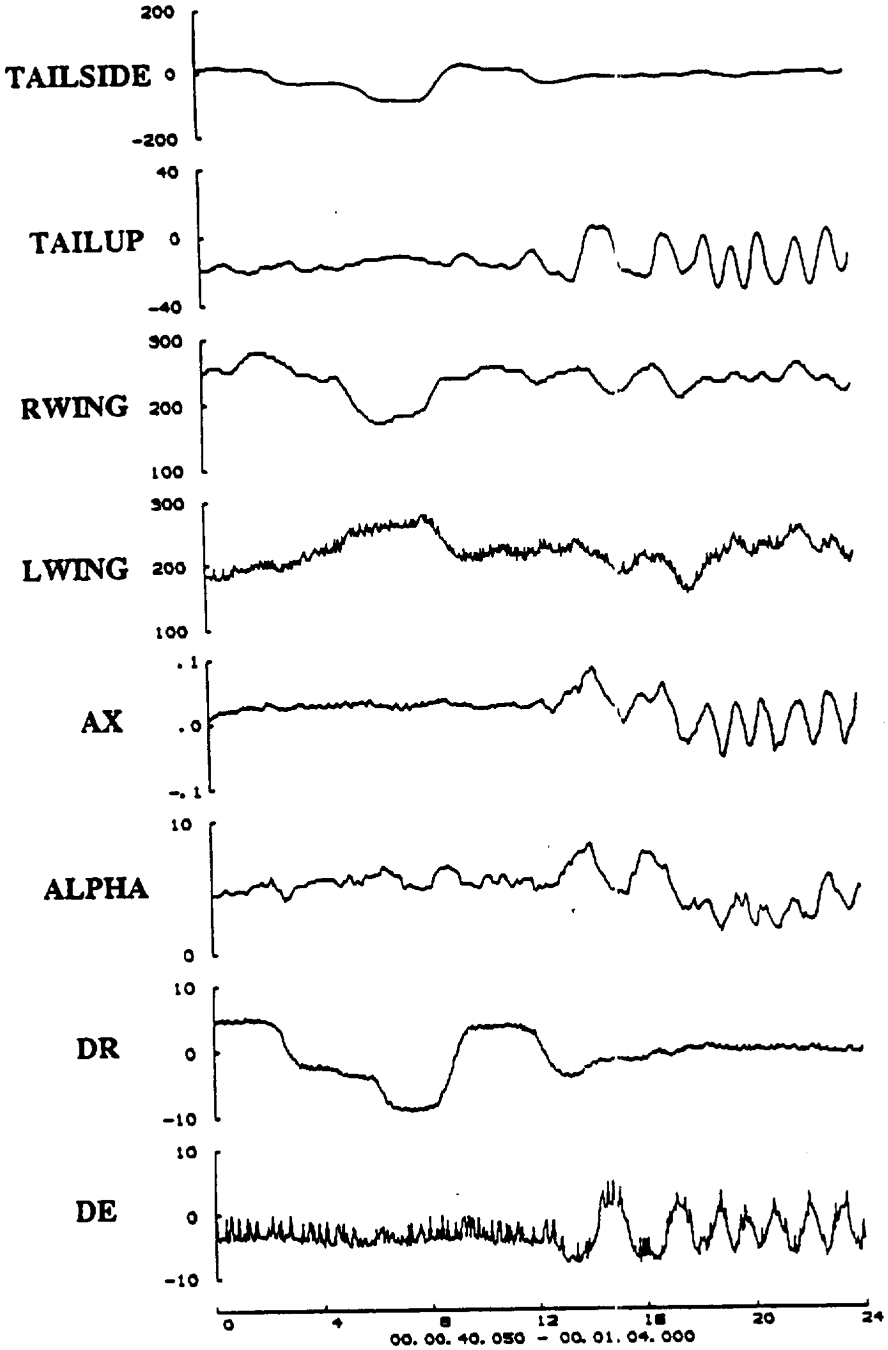

Figure 2-6 Elevator Frequency Sweep

3.0 Parameter Estimation and Aircraft Dynamics

Considerable flight time was devoted to investigating the dynamics and the aeroelastic behavior of the Light Eagle aircraft. The results from these tests should extend the knowledge of aeroelastic effects of low Reynolds number aircraft and should prove valuable to designers of both the structure and the autopilot of high altitude, solar powered research aircraft.

To characterize the aeroelastic behavior of the Light Eagle, sets of strain gages were placed on its wing and tailboom. Signals from these sensors and the other instrumentation onboard the aircraft were recorded by the DAS and later processed with a parameter estimation program. This program tried to optimally fit flight data with a mathematical model of the aircraft augmented with various flexibility effects.

Although the basic theoretical considerations and the data from the test flights suggest that the flexibility effects of the structure and the unsteady aerodynamics effects are both significant, the first attempt to estimate stability and control derivatives was based on a rigid-body model with quasi-steady aerodynamics. This parameter estimation was performed using NASA Dryden software known as pEst [5,6]. From the elevator, rudder, and aileron inputs and the measured aircraft response, the program iteratively adjusts a specified set of stability and control derivatives in order to minimize the time integral of the mean squared error between the measured and the simulated responses. The initial estimates of the stability derivatives were generated by QUADPAN, a computational method that treats the aircraft as a rigid body and is able to model steady, three dimensional flow around it. QUADPAN is described in more detail in reference [7].

3.1 Parameter Estimation

Though the constants that define the aircraft's mass, inertias, wing area, span, chord, and center-of-gravity location are well known, many of the longitudinal and lateral-directional stability and control derivatives are not well known and are difficult to predict analytically. Amongst them are $C_{l\beta}$, C_{lp}, C_{lr}, $C_{n\beta}$, C_{np}, and C_{nr}. Generally, the effects of C_{lr}, C_{nr}, C_{lp}, and C_{np} are not significant for the overall behavior of typical aircraft, but in the case of extremely light wing loadings, low Reynolds number airfoils, high aspect ratio planforms, low flight speeds, and highly flexible structures, this may not be true. During the Light Eagle flight test program it was found that as the aircraft turns, much higher angles-of sideslip are produced than are predicted by QUADPAN. Therefore parameters like $C_{l\beta}$ and $C_{n\beta}$ become very important. Also, since the Light Eagle has such a large wing span and such a low flight speed, much of the rolling moment into a turn is generated by C_{lr} , which typically is not significant in more conventional aircraft.

When estimating stability and control parameters from small perturbation maneuvers, unusual results may be obtained if too many parameters are estimated at one time. Therefore when using pEst, a number of parameters were fixed leaving only five to six parameters free that the program would estimate. This lead to an iterative procedure during which one flight test maneuver would be analyzed with different sets of free parameters. Using this technique, an understanding was obtained of the importance and the effects of each parameter on the performance and convergence of the mathematical model of the aircraft.

After analyzing a number of parameters with either the same maneuver or an ensemble of similar maneuvers (e.g. rudder doublets), it became obvious that a time delay existed between when the rudder was actuated and when the yawing moment acted upon the fuselage. This lead to contradictory estimation results; consequently, the validity of the rigid-body model came into question. Figure 3-1 shows time history plots for a rudder doublet with the estimator trying mainly to minimize the error between the measured and the simulated yaw rate response, lateral acceleration, and sideslip angle. Less emphasis was placed upon roll rate and tailside bending moment in order to improve the curve fit on the first three variables. Although the maneuver was one of the best that was performed throughout the entire flight test program, it is obvious that the tailside bending moment is generated more slowly than predicted by the model.

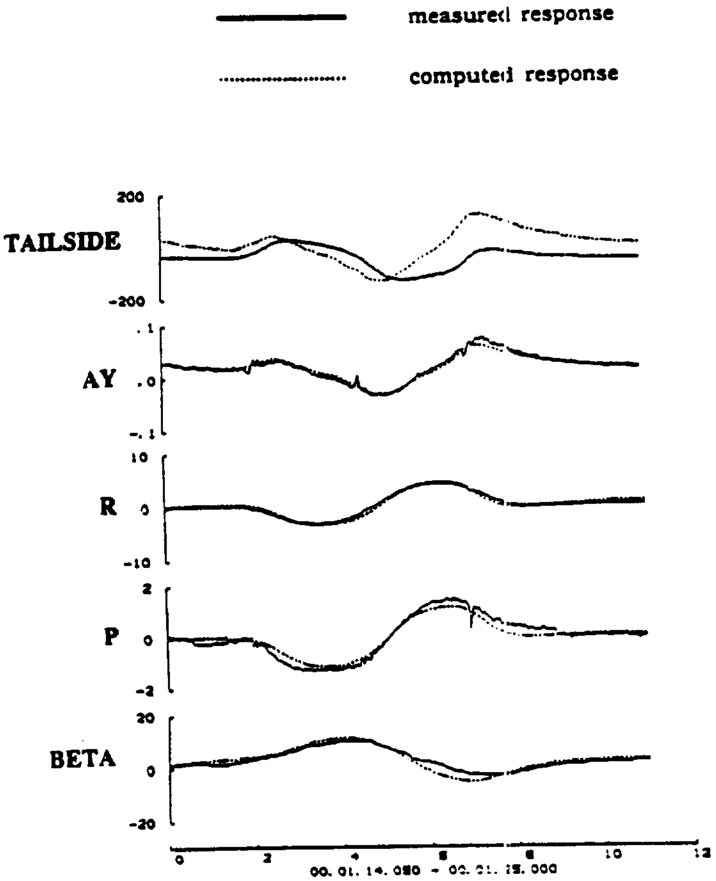

Figure 3-1 Rudder Doublet (Measured vs Computed Response)

3.2 Simple Model of Flexibility and Aerodynamic Lag

Inspection of Figure 3-1 suggests that the computed tailside bending moment response differs from the measured response by a simple lag. Indeed, such a lag can be explained by the flexibility of the tailboom itself and by the unsteady aerodynamic effects on the tail surfaces. Simple estimates, using quasi-steady aerodynamics, suggest that the tailboom lateral bending motion exhibits an aerodynamic damping of 20 percent of critical. This highly damped mode, with a resonant frequency of 1.4 Hz, resembles a first order lag with a time constant of 0.3 seconds. In addition to this lag, there is also a lag due to unsteady aerodynamics. Fung [8] gives a clear discussion of the the lift produced by an airfoil with a sudden change in angle of attack. He shows that the unsteady lift is given by a time convolution of Wagner's function with the downwash at the 3/4 chord point. Wagner's function is well approximated by

$$\Phi(T) = 1 - 0.165\, e^{-0.0455\,T} - e^{-0.03\,T}$$

$$T = \frac{2 U_\infty t}{c}$$

This indicates a first-order aerodynamic lag with a time constant (based on rudder chord of c=0.7 m; U_∞=8 m/s) of:

$$\tau = \frac{3.3\,c}{2\,U_\infty} = 0.14 \text{ secs}$$

These lags have been implemented in the lateral-directional equations of motion by including a first-order filter between the rudder deflection and the torque applied to the fuselage.

$$\dot{x}_{lag} = \frac{1}{\tau} x_{lag} + \frac{1}{\tau} \delta_r$$

$$C_l = C_{l_o} + C_{l_\beta} \beta + \frac{b}{2 V R} (C_{l_r} r + C_{l_p} p) + C_{l_{\delta r}} x_{lag}$$

$$C_n = C_{n_o} + C_{n_\beta} \beta + \frac{b}{2 V R} (C_{n_r} r + C_{n_p} p) + C_{n_{\delta r}} x_{lag}$$

$$C_y = C_{y_o} + C_{y_\beta} \beta + \frac{b}{2 V R} (C_{y_r} r + C_{y_p} p) + C_{y_{\delta r}} x_{lag}$$

$$\text{tailside} = q\, S_R\, l\, (C_{y_{\delta r}} x_{lag} + C_{y_\beta} \beta) + \text{tailside}_{bias}$$

Figure 3-2 shows the improvement in the curve fit (compared to Figure 3-1) on the tailside bending moment after extending the lateral equations of motion with the tailboom flexibility mode. For this curve fit, the same weights have been placed on the yaw rate, lateral acceleration, sideslip angle, roll rate, and bending moment as were used for the analysis in Figure 3-1. Table 3-1 presents a comparison between the stability and control parameters as estimated by pEst from this maneuver, with those computed analytically by QUADPAN. The differences between the results suggest that the effects of the aircraft flexibility and unsteady aerodynamics are quite significant.

Note that a considerable discrepancy exists between QUADPAN's and pEst's estimates of C_{l_β}. This difference may be explained by flexibility effects in the wing. To initiate a turn, the rudder is deflected, thus causing the sideslip angle to increase. Due to this sideslip angle and the associated yaw rate, the wingtip on the outside of the turn has more lift on it than the inner wingtip; consequently, the outer wingtip's dihedral increases and thus the C_{l_β} increases. A significant period of time elapses between when the sideslip develops, the wing structure

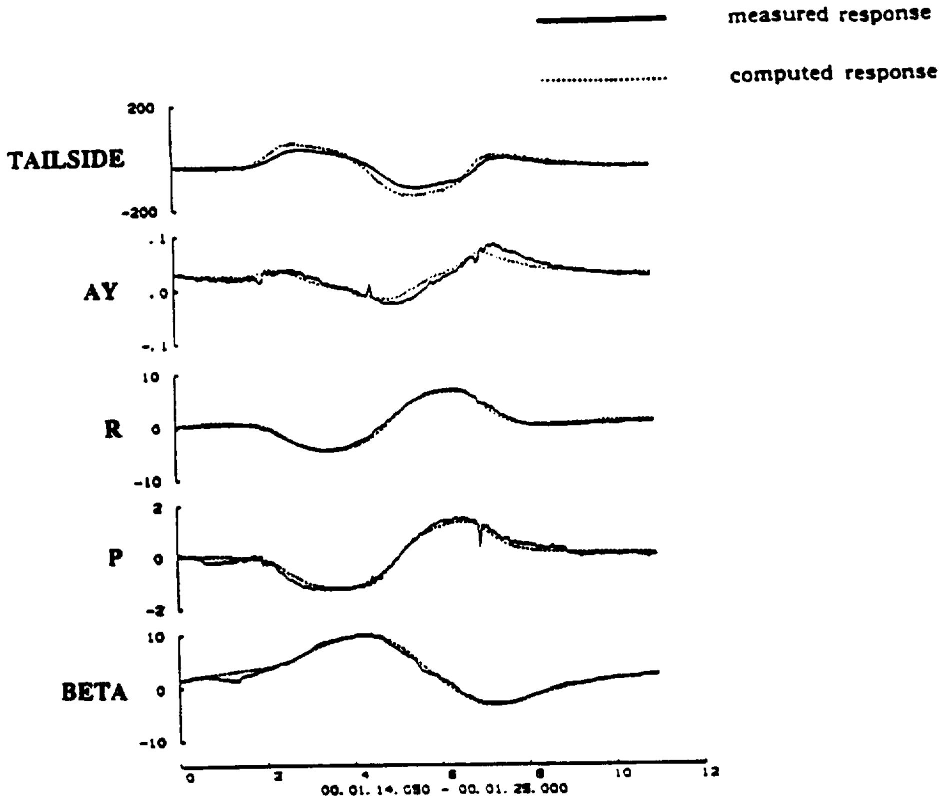

Figure 3-2 Rudder Doublet with Modeled Flexibility Lag

QUADPAN		pEst		pEst (with lag terms)
0.0000	C_{yo}	0.0425	C_{yo}	0.0332
- 0.0070	$C_{y\beta}$	- 0.0063	$C_{y\beta}$	- 0.0040
0.0053	$C_{y\delta r}$	0.0046	$C_{y\delta r}$	0.0032
0.0000	C_{lo}	- 0.0014	C_{lo}	- 0.0013
- 0.1000	$C_{l\beta}$	- 0.0007	$C_{l\beta}$	- 0.0015
- 0.7900	C_{lp}	- 0.2445	C_{lp}	- 0.7900
0.2110	C_{lr}	0.0567	C_{lr}	0.1456
0.0000	C_{no}	0.00006	C_{no}	0.00002
0.00065	$C_{n\beta}$	0.00002	$C_{n\beta}$	0.0002
- 0.00095	$C_{n\delta r}$	- 0.0087	$C_{n\delta r}$	- 0.0012
0.0000	a_{ybias}	- 0.0048	a_{ybias}	- 0.0033
0.0000	τ	0.0000	τ	0.0170

Table 3-1 Parameter Estimation Results

deflects, and the roll rate begins. Due to this considerable time lag, the roll rate is not well correlated with the sideslip angle; consequently, a poor estimate for $C_{l\beta}$ is obtained.

Because of the spectral limitation of the aerodynamic actuation and the apparent high damping in all the responses, a rigid-body model of the aircraft, when augmented by low-pass filters to simulate the flexibility effects, has some applicability for modeling the motion of the aircraft. The model is valid to high frequencies, well into the range where unsteady aerodynamics and flexibility become important; however, this validity is restricted to excitations from the aerodynamic control surfaces and to maneuvers similar to those performed in the flight tests. Such a model has utility for pilot handling evaluation and for autopilot design. It is, however, somewhat phenomenological and cannot predict other important aspects of aircraft motion such as flutter and gust response.

3.3 Aeroelastic Model

In order to obtain a better understanding of the Light Eagle's dynamics, a fully flexible aeroelastic model has been developed from the frequency estimates of Table 3-2. Details of the model are given in Appendix A. The approach taken in developing the model was to use assumed modes that were generated by an eigen-analysis of the free-free aircraft with apparent mass loading but with no flight speed. The analysis is marked by the approximate equality of many structural natural frequencies. Illustrations of the structural modes are provided in Appendix B. No clear spectral separation between the low-frequency and high-frequency modes has been identified; consequently, it is difficult to justify the inclusion or exclusion of any particular mode.

To further investigate the aircraft's dynamics, the aeroelastic model of the aircraft has been extended to include the effects of forward flight speed. Three analyses have been

1. Structural Natural Frequencies (with apparent mass):

Symmetric:

- first up/down wing bending mode: 0.6 Hz
- first elevator up/down bending: 1 Hz
- first fore/aft wing bending mode with a strong tailboom participation: 1.6 Hz
- second up/down wing bending mode: 2.5 Hz
- second fore/aft wing bending mode with a strong tailboom participation: 3.0 Hz
- third up/down wing bending mode: 4.5 Hz

Anti-symmteric:

- tailboom torsion mode: 0.6 Hz
- first up/down wing bending mode: 0.9 Hz
- first fore/aft wing bending mode: 1.4 Hz
- second up/down wing bending mode: 2.8 Hz
- second fore/aft wing bending mode: 3.9 Hz

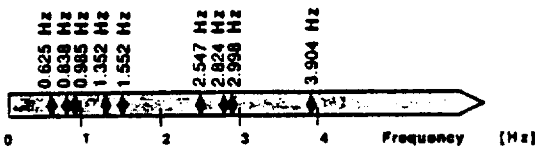

2. Rigid-body Estimates (quasi-steady aerodynamics):

phugoid: 0.1 Hz (lightly damped)
short-period: 1 Hz (critically damped)
spiral: 11 secs (unstable)
dutch roll: 10 Hz, 5 Hz (over critically damped)

3. Aerodynamic Lag:

first order fit to Wagner's function: pole at 0.14 Hz
reduced frequendy at 1 Hz: 0.63

4. Pilot pedaling: 1.8 to 2.0 Hz

5. Summary of modeling approaches

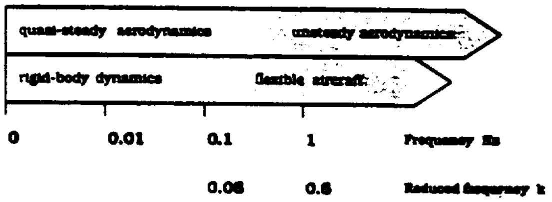

Table 3-2 Aircraft Structural Natural Frequencies

performed: (1) the aircraft flying at sea level with the nominal pitch inertia, (2) the aircraft flying at sea-level with an increased pitch inertia, and (3) the aircraft flying at approximately 6000 meters (half the sea-level density) with the nominal pitch inertia. These cases illustrate how the dynamics of the aircraft change with airspeed, with different payload weights, and with altitude. The most significant implication of these results is on the design of an autopilot for a high-altitude RPV similar in construction to the Light Eagle. It is clear that a very sophisticated and robust autopilot will be necessary to handle the changes in the aircraft's dynamics due to each of these effects.

The first analysis case examines the aircraft's aeroelastic behavior at sea-level with the nominal pitch inertia (186 kg-m^2). The root-locus plot in Figure 3-3 summarizes the results for this case by illustrating the trajectory of the short period and phugoid modes with increasing airspeed. The respective frequency and damping ratios of each of these modes is shown in Figures 3-4 and 3-5. It is clear, that the phugoid mode is initially fairly poorly damped; however, as the velocity approaches 4.0 meters/sec, the damping increases significantly. Simultaneously, the natural frequency of this mode decreases from approximately 1.0 Hz to 0.3 Hz. As the velocity increases further, the damping begins to decrease, and by 7.0 ft/sec, the damping ratio is less than that at the lowest airspeed. As this is happening, the natural frequency of this mode is continuing to drop. Thus at the higher speeds, the phugoid mode becomes very lightly damped and has a period of approximately 5 seconds. The short period mode damping is fairly constant throughout the velocity range; however, the natural frequency of this mode starts around 0.5 Hz and increases almost linearly with airspeed. At 10.0 ft/sec, this mode has a natural frequency of around 1.9 Hz.

A similar analysis has been then performed assuming that the pitch inertia is 30% higher (242 kg-m^2) than the inertia in the previous case. Figures 3-6 through 3-8 illustrate the trajectories of the short period and phugoid modes for the aircraft with the increased pitch inertia. Results similar to those of the previous case are found; however, now the aircraft's short period mode is initially located where the phugoid mode was initially located in the previous case. Furthermore, in the prior case, the short period mode was not oscillatory at the lower airspeeds, now however it is. As the airspeed increases, the frequency of the short period mode increases, but the rate of increase is less for this case than for the previous case.

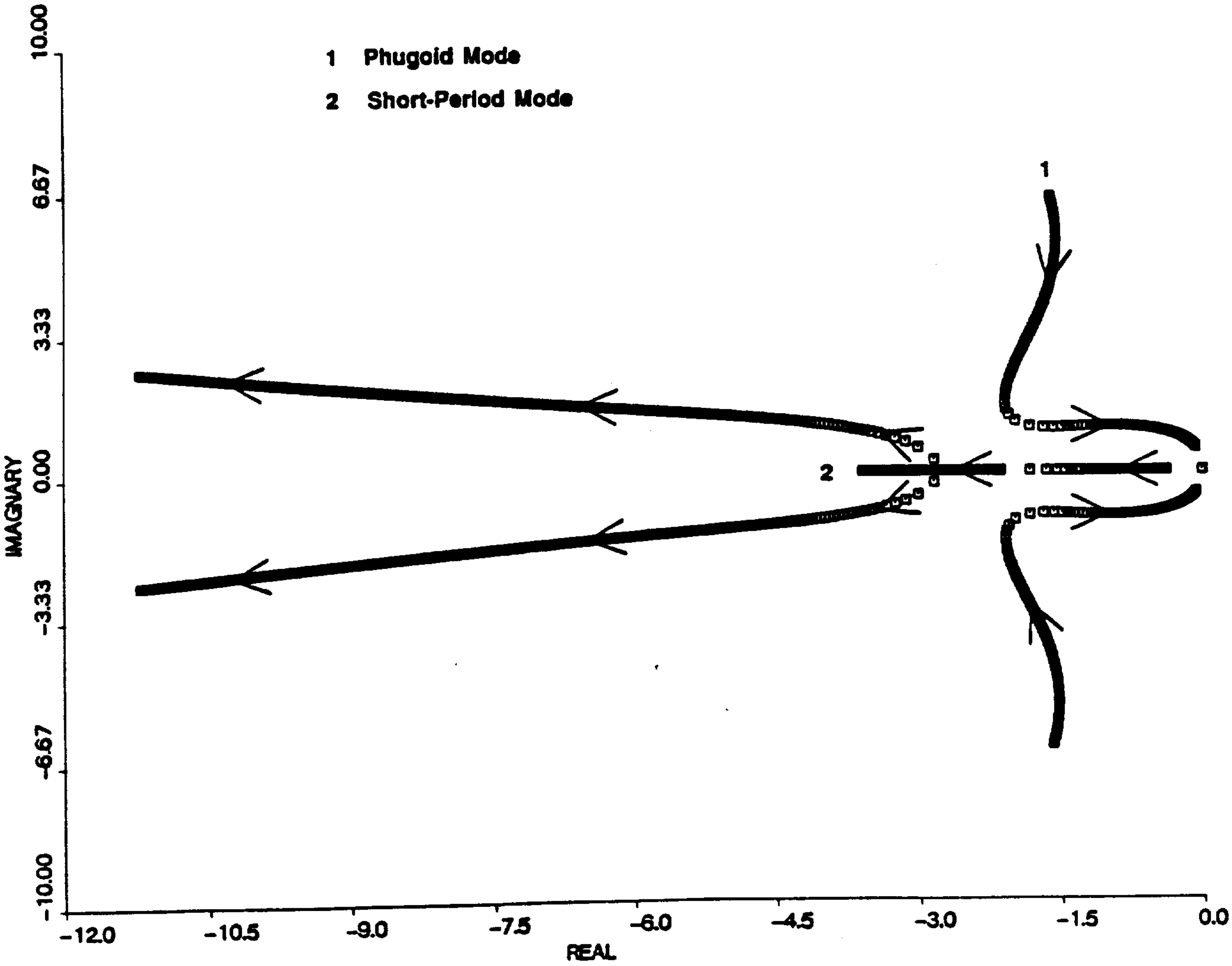

Figure 3-3 Root Locus of Longitudinal Modes with Increasing Airspeed
(Sea-Level, Nominal Pitch Inertia = 186 kg m^2)

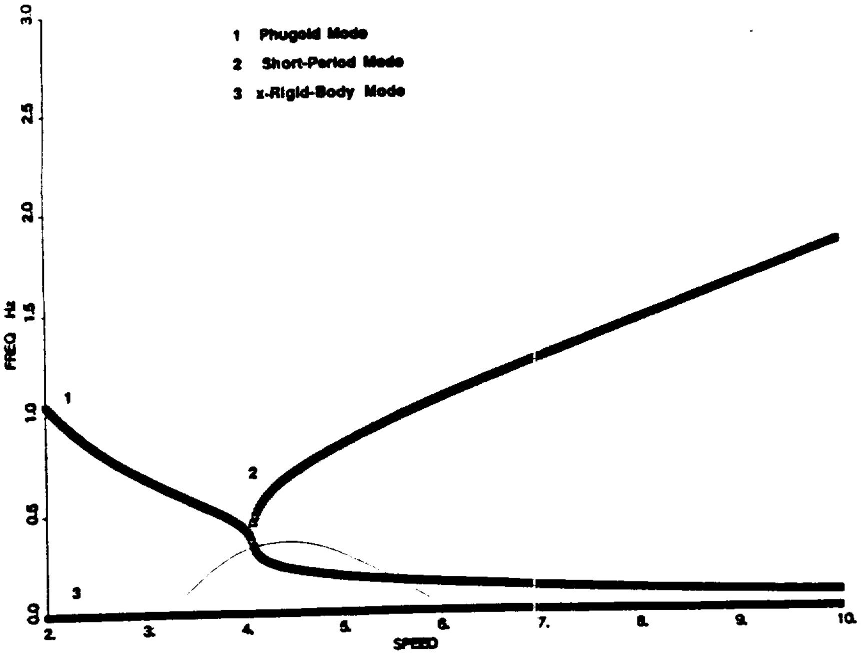

Figure 3-4 Longitudinal Modal Frequencies with Increasing Airspeed (Sea-Level, Nominal Pitch Inertia = 186 kg m^2)

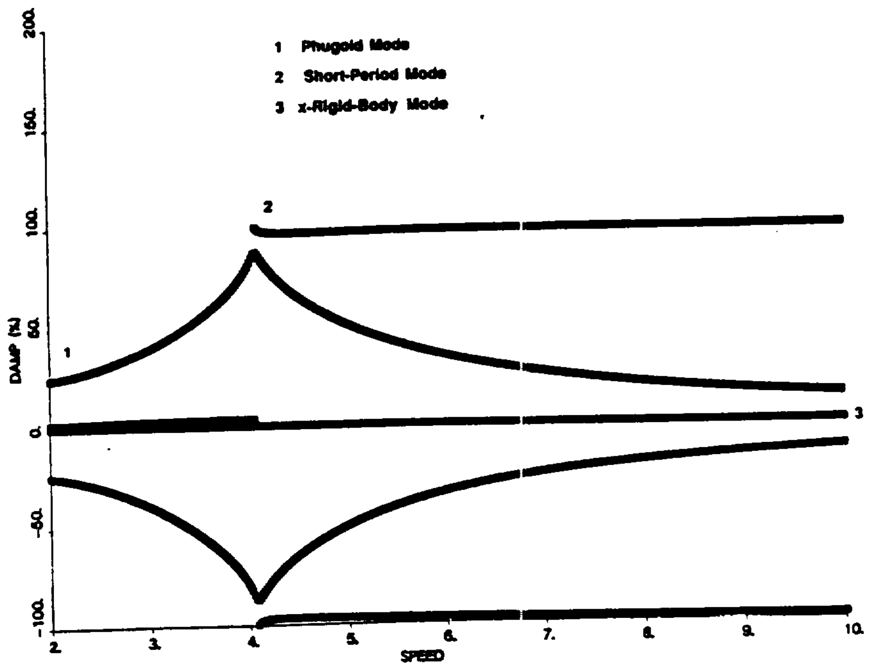

Figure 3-5 Longitudinal Modal Damping with Increasing Airspeed (Sea-Level, Nominal Pitch Inertia = 186 kg m^2)

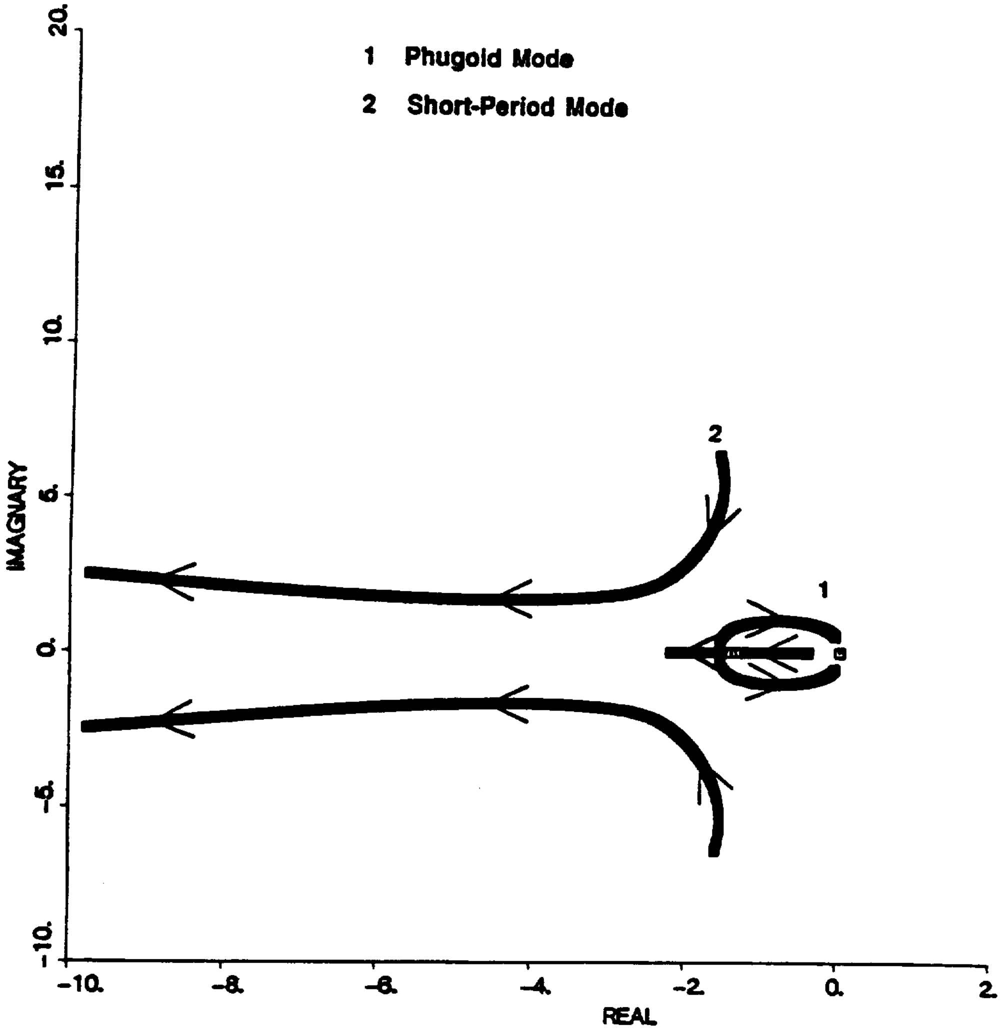

Figure 3-6 Root Locus of Longitudinal Modes with Increasing Airspeed (Sea-Level, Increased Pitch Inertia = 242 kg m^2)

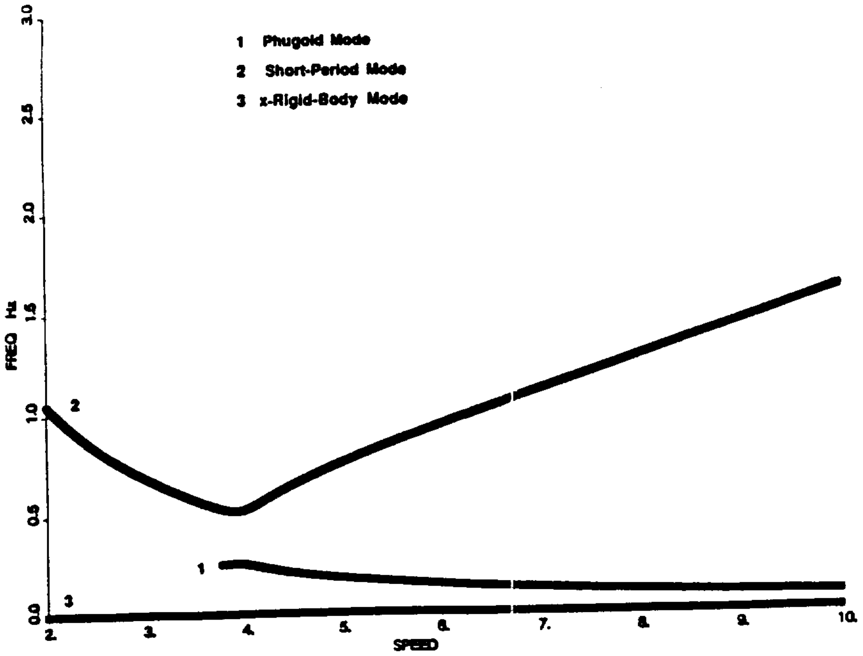

Figure 3-7 Longitudinal Modal Frequencies with Increasing Airspeed (Sea-Level, Increased Pitch Inertia = 242 kg m^2)

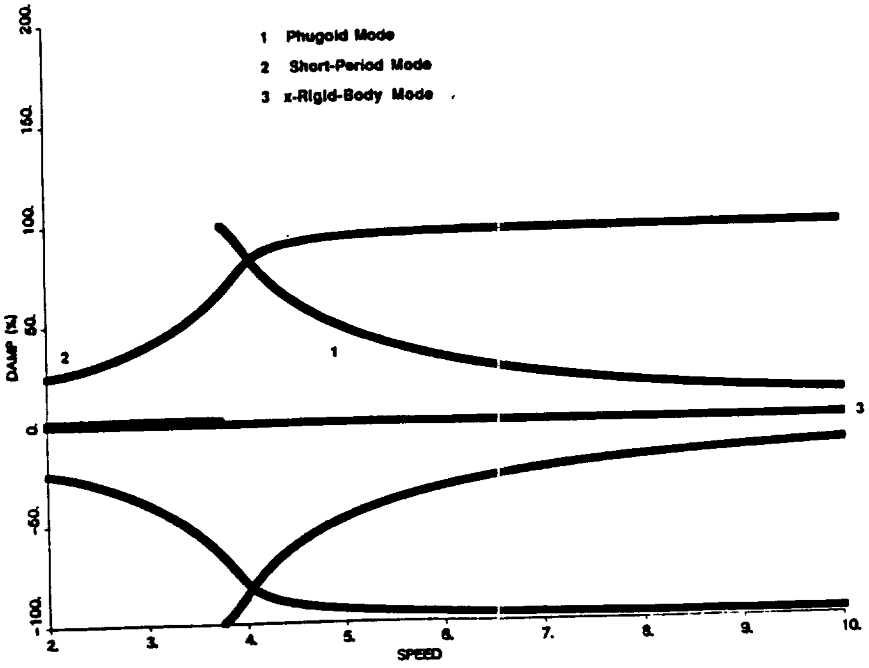

Figure 3-8 Longitudinal Modal Damping with Increasing Airspeed (Sea-Level, Increased Pitch Inertia = 242 kg m^2)

For this higher inertia case, the phugoid mode is initially well damped, much more than before; however, as the airspeed increases, the damping decreases to the level observed previously.

An analysis has also been performed assuming that the air density is half that of the original case. This corresponds to an altitude of 6000 meters. The pitch inertia is assumed to be identical to that used in the first analysis. From Figures 3-9 through 3-11, it is clear that the short period mode is now oscillatory throughout the entire speed range. Furthermore, as the airspeed increases, the rate at which the short period's natural frequency increases is less than the rate observed in the sea-level case. The natural frequency of the phugoid mode is fairly constant across the speed range for the high altitude case; whereas, there is considerable variation in the sea-level case. Also for the high altitude case, the phugoid damping is much better at airspeeds below 4.0 meters/sec; however, above this speed, the damping ratios for both cases are almost identical.

The results of these analyses indicate that a sophisticated autopilot will be required to stabilize the Light Eagle if it is used as a high-altitude RPV. Changes in airspeed and altitude have a significant effect on the dynamics of the aircraft and these effects cannot be ignored in designing the autopilot. Furthermore, changes in the mass and distribution of the payload will change the pitch inertia and will thereby affect the natural frequencies of the aircraft's pitch modes. The autopilot will have to be flexible enough and robust enough to handle all these conditions. Further constraints are placed on the autopilot robustness due to uncertainties in the aeroelastic model of the aircraft. The aeroelastic model is of high order and represents a significant computational extrapolation from experimentally verified results. In order to improve the confidence in the model, experimental validation will be necessary. A ground vibration test can be used to validate the model at zero flight speed and with different boundary conditions. Additional flight tests using excitation schemes other than aerodynamic control

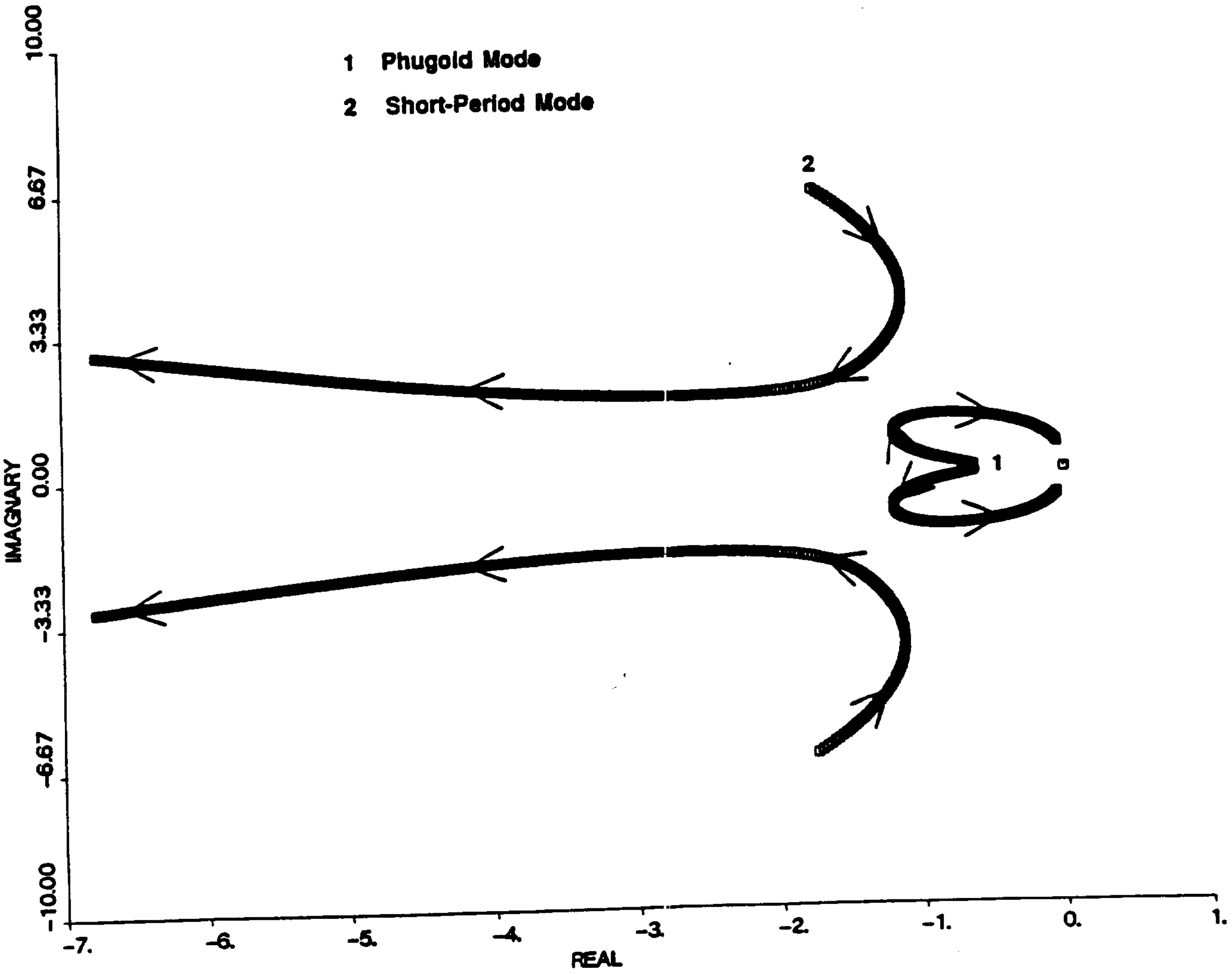

Figure 3-9 Root Locus of Longitudinal Modes with Increasing Airspeed
(6000 Meters Altitude, Nominal Pitch Inertia = 186 kg m^2)

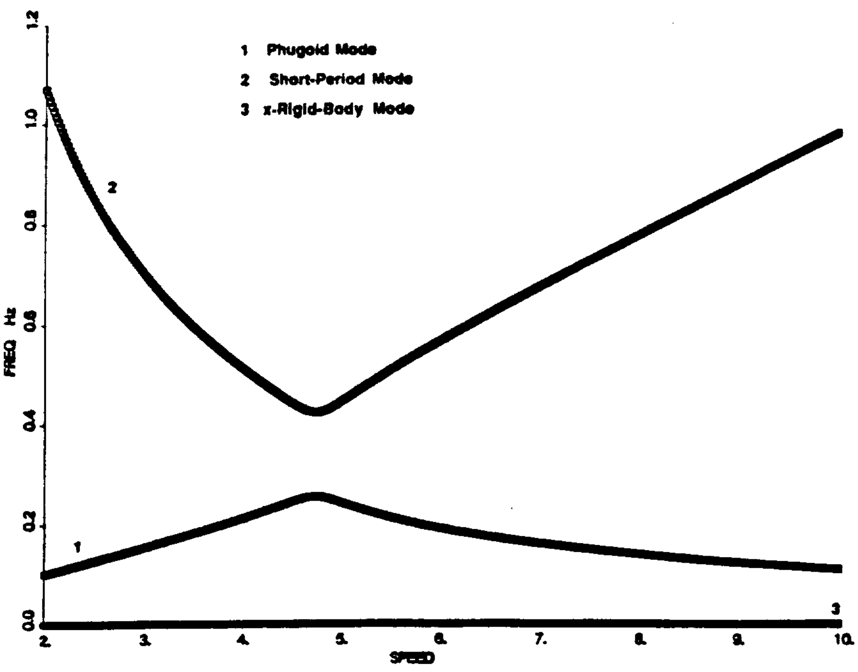

Figure 3-10 Longitudinal Modal Frequencies with Increasing Airspeed (6000 Meters Altitude, Nominal Pitch Inertia = 186 kg m^2)

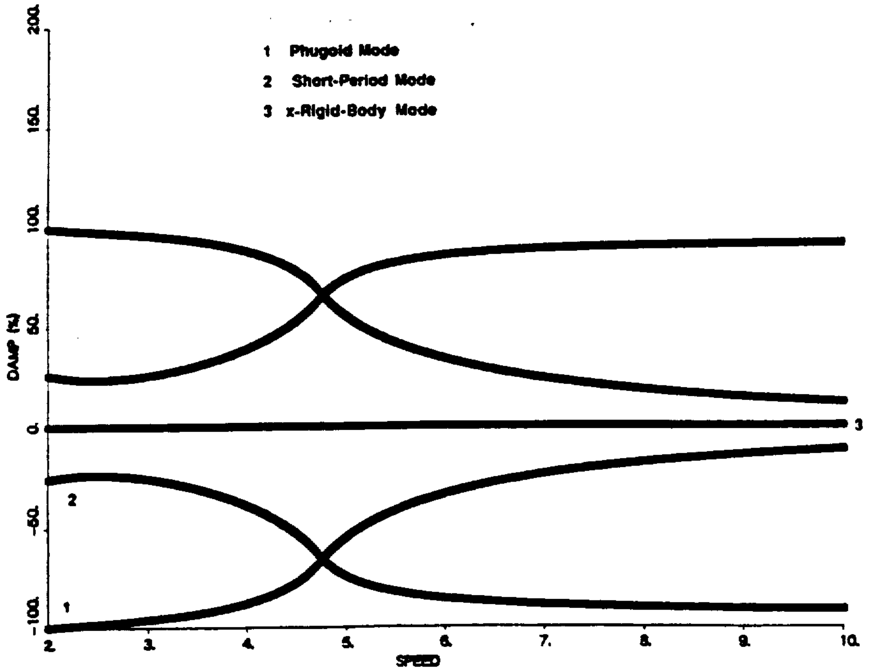

Figure 3-11 Longitudinal Modal Damping with Increasing Airspeed (6000 Meters Altitude, Nominal Pitch Inertia = 186 kg m^2)

surfaces may prove necessary to provide sufficient high frequency content to identify parameters associated with the faster degrees of freedom. Novel excitation schemes might include dropping weights, firing small rocket motors, and having bicyclists pull on ropes. Even with these tests, it is unlikely that such a large model would ever be fully validated experimentally.

3.4 Daedalus Autopilot Performance

Because the final flight of the Daedalus aircraft was expected to take four to five hours to complete, an autopilot was designed to help simplify the pilot's task of controlling the aircraft. The autopilot was never actually flight tested due to difficulties in developing the required sensors. Nevertheless, it is interesting to analyze the performance that the system would have had in light of the aircraft dynamics observed during flight tests. The design of the control system was based on rigid-body dynamics with the stability derivatives predicted by the QUADPAN computer algorithm. However, the flight tests have demonstrated that the aircraft exhibits additional dynamics due to the flexibility of the structure. Furthermore, the data from the flight tests have produced estimates for the stability derivatives, some of which are quite different from those predicted by QUADPAN. In the following sections, the design of the autopilot is described and the performance of the system is evaluated with the updated aircraft dynamics.

3.4.1 Autopilot Design

The autopilot was designed to maintain a constant airspeed (independent of the power supplied by the pilot), to hold a wings level attitude, and to track a desired heading. To minimize the complexity of the system, the autopilot was designed such that all control inputs were to have been made through the rudder and elevator; the ailerons would not have been used.

3.4.2 Airspeed Hold System

The airspeed hold system maximizes the performance of the aircraft by keeping the airspeed close to the velocity at which the maximum lift to drag ratio is achieved. If the aircraft is flying faster than this speed, the control system corrects by gaining altitude, thus converting the excessive kinetic energy into potential energy. If the aircraft is flying slower than the optimal speed, the aircraft dives to regain the necessary velocity.

To implement this system, both an attitude sensor and an airspeed sensor are required. The first step in stabilizing the longitudinal dynamics is achieved by feeding back the signal from the attitude sensor (Figure 3-12). Next, the airspeed is regulated by feeding back the difference between the aircraft's desired velocity and its actual velocity. Finally, the steady state error is forced to zero by feeding back the airspeed error through an integrator. The three feedback signals are summed to create the position signal for the elevator servo. This signal is then passed through a limiter so that excessive elevator deflections are not commanded.

3.4.3 Wing Leveler and Heading Hold System

To maintain a wings level attitude and to maintain the correct heading, a lateral control system has also been designed for the aircraft. The block diagram of this system is shown in Figure 3-13. Note that stabilization is achieved simply by feeding back the roll angle and heading error signals.

3.4.4.0 Autopilot Performance with Rigid-Body Versus Flexible-Body Dynamics

The autopilot was designed using QUADPAN estimates of the stability derivatives and assuming rigid body dynamics; consequently, it is interesting to investigate the system's

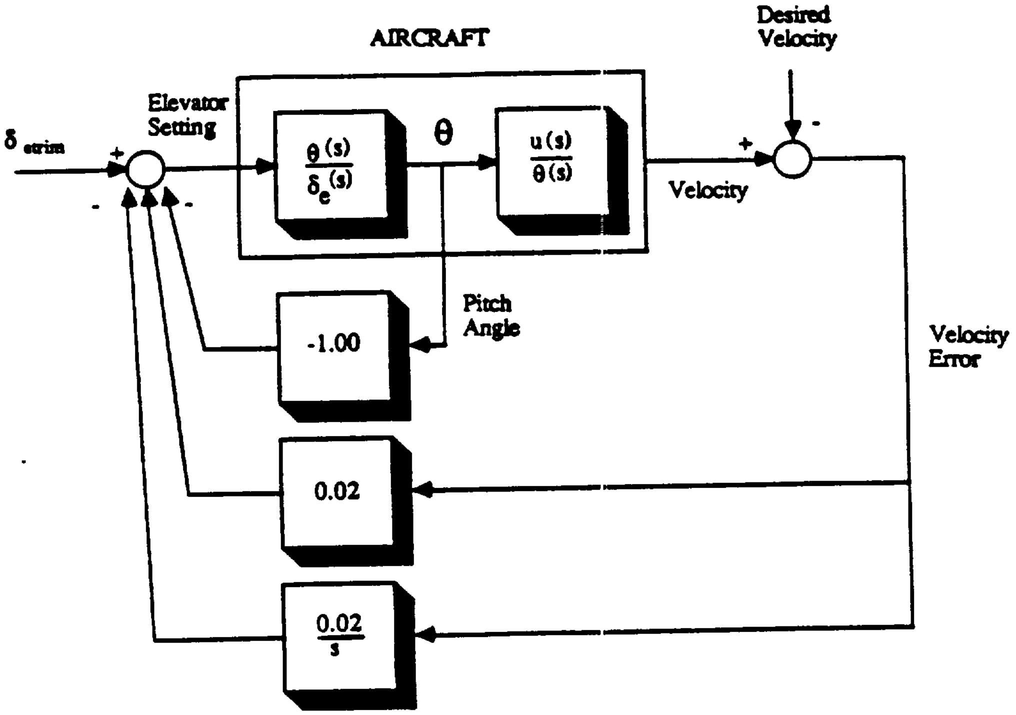

Figure 3-12 Block Diagram of Airspeed Hold System

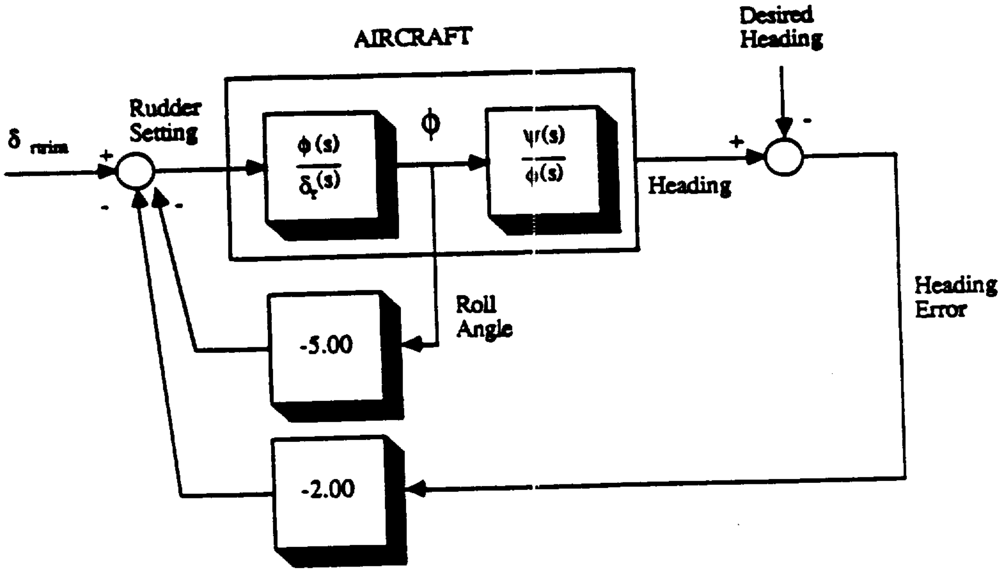

Figure 3-13 Block Diagram of Lateral Control System

performance with the aircraft's dynamics augmented with the tailboom flexibility effects described in Section 3.2. To evaluate the effects of the modified dynamics, first the open-loop longitudinal dynamics are compared with and without the flexibility effects. The airspeed hold autopilot's closed-loop performance is then investigated using each of the dynamics models. Next the lateral dynamics are explored. Simulations of the open loop lateral dynamics are compared with and without flexibility effects present. The stability derivatives are then modified to represent those derived by pEst from the flight test data. Finally, the heading hold autopilot is evaluated with these new dynamics present.

3.4.4.1 Open-Loop Longitudinal Dynamics

The rigid-body, open-loop response of the aircraft's longitudinal axis is shown in Figure 3-14 for a -2.0 degree step in the elevator setting. As expected, the change in the elevator setting causes the aircraft to pitch up. This in turn causes the aircraft to gain altitude and to lose airspeed, thus causing the phugoid mode to be excited.

Superimposed on the rigid body dynamics in Figure 3-14 are the dynamics including flexibility effects. The plot of the elevator setting reveals how the flexibility of the tailboom causes a lag in the effective elevator setting. This lag results in a corresponding lag in the change in pitch angle, altitude, and velocity of the aircraft. Furthermore, the magnitude of these changes are slightly reduced due to the filtering effects of this flexibility. If higher frequency control inputs are made, the magnitude of the effective elevator settings will also be attenuated due to the filtering effects of the tailboom flexibility.

3.4.4.2 Closed Loop Longitudinal Dynamics of the Airspeed Hold System

The rigid-body, closed-loop dynamics of the airspeed autopilot are illustrated in Figure 3-15. At 5 seconds into the simulation, a 1.0 meter/sec airspeed change is commanded. The

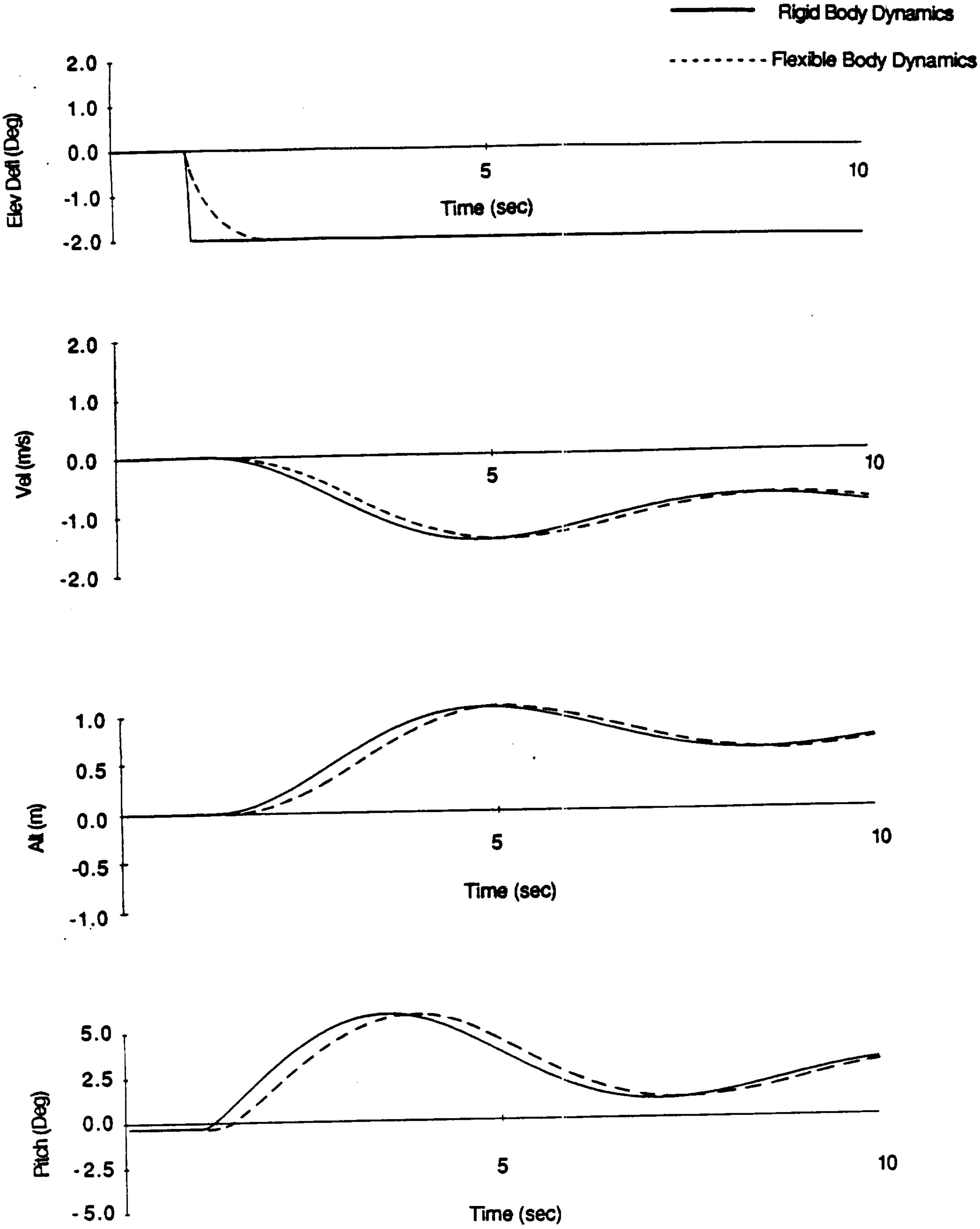

Figure 3-14 Open-Loop Longitudinal Dynamics
(Rigid-Body vs Flexible Dynamics)

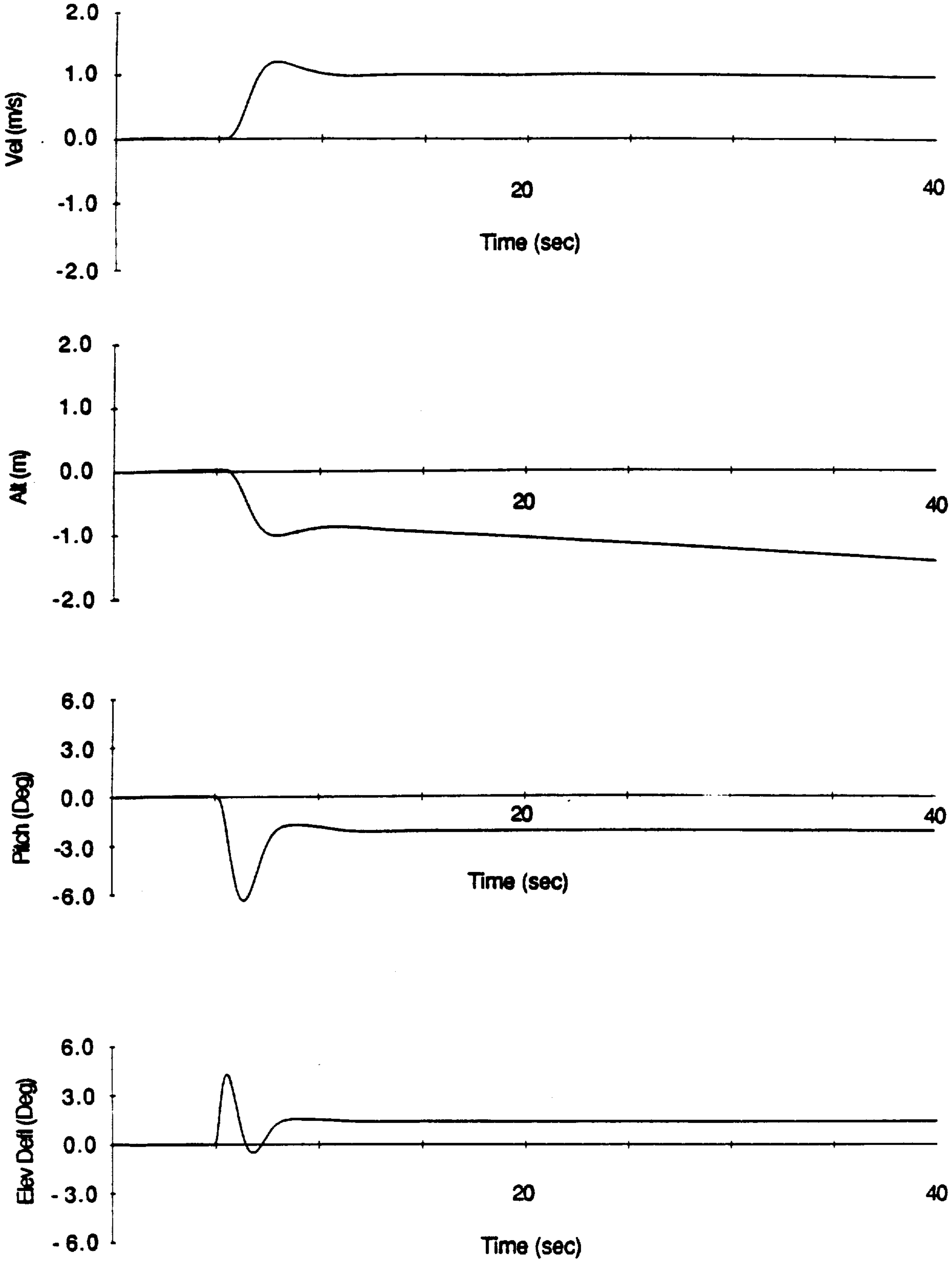

Figure 3-15 Airspeed Hold Performance (Rigid Body Model)

autopilot commands the aircraft to pitch down in order to increase its velocity. This increase in kinetic energy results in a corresponding decrease in potential energy (altitude). By the end of approximately 5.0 seconds, the autopilot has settled to the desired airspeed.

When the airspeed hold system was designed, the magnitude of the flexibility effects in the tailboom were not foreseen; consequently, its design was based solely on rigid body dynamics. From flight data it has become obvious that this assumption was not valid. Figure 3-16 shows the marked difference in the autopilot's performance when the tailboom flexibility effects are included. Note that the aircraft's response, though stable, is now oscillatory even after 30 seconds of time. This autopilot performance is obviously unacceptable and, due to the velocity oscillations, the efficiency of the aircraft is now compromised.

A quick study was made to determine if the autopilot's performance could be improved. One technique that proved to be relatively successful was to augment the pitch angle stabilization loop with pitch rate feedback. Figure 3-17 shows the improved performance. Note that now, the oscillations are much more damped and after 10 seconds, the system has settled to the desired airspeed. It is likely that even better performance can be achieved if a more complete and systematic design process is used.

It was hoped that the autopilot's performance could have been evaluated with the longitudinal stability derivatives measured during flight tests. However on February 7, 1988, the Daedalus 87 aircraft crashed due to insufficient roll control. As a result, the priorities of the flight test program were shifted and work was directed toward solving this lateral control problem. Therefore, most of the data collected was in the lateral axes; insufficient data was obtained to reliably estimate the longitudinal stability derivatives.

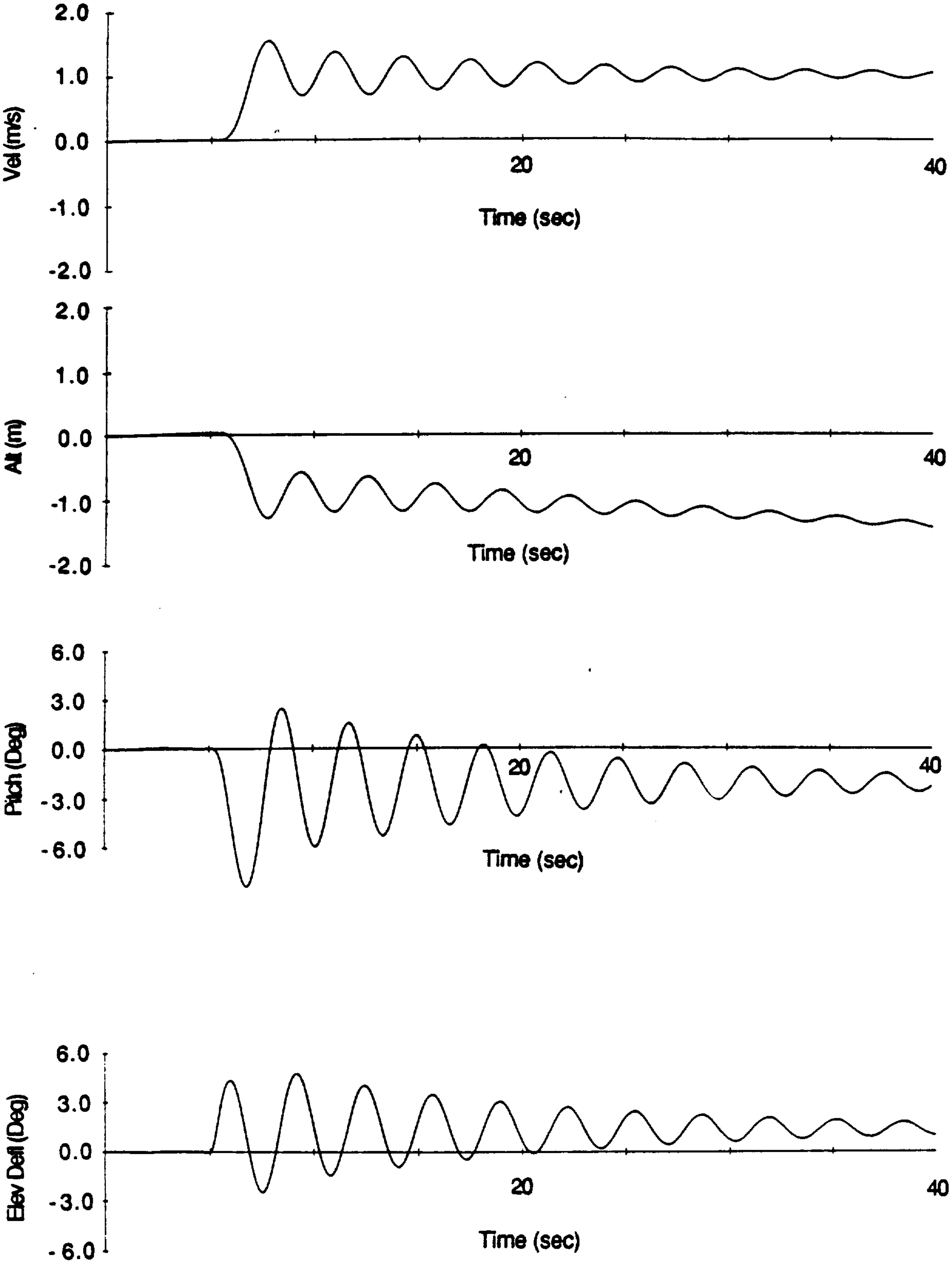

Figure 3-16 Airspeed Hold Performance (Flexibility Effects Included)

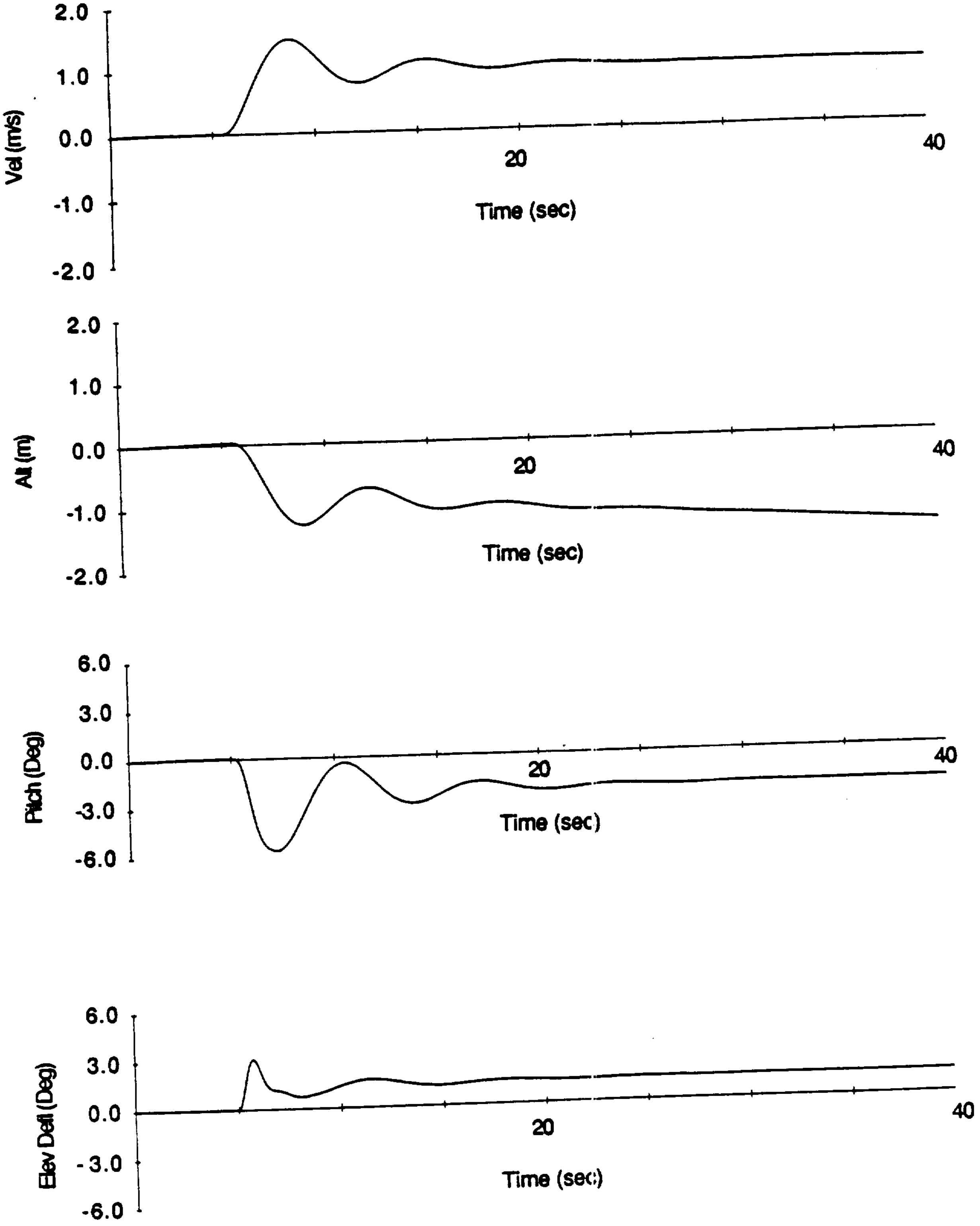

Figure 3-17 Airspeed Hold Performance (Flexibility Effects Included)
(With Improved Feedback Compensation)

3.4.4.3 Open-Loop Lateral Dynamics

The rigid-body, open-loop response of the aircraft's lateral axis is shown in Figure 3-18 for a 5.0 degree rudder pulse. (The model used in this simulation assumes the QUADPAN stability derivatives). The resulting yaw rate and sideslip angle cause the aircraft to start rolling to the left; consequently, the heading changes to the left. Note that once a roll angle is established, even with no rudder input, the aircraft's roll angle continues to increase. This is the spiral divergence mode that resulted in the crash of the Daedalus 87 aircraft.

Also shown in Figure 3-18 is the aircraft's open-loop lateral response with the tailboom flexibility effects included. The primary effect of the flexibility is the time lag between when the rudder change is commanded and when the yawing moment is effectively applied to the aircraft. The filtering characteristics of the flexibility also reduce the high frequency components of the yawing moment; consequently, the yaw rate and roll rate magnitudes are slightly reduced.

Figure 3-19 demonstrates the open-loop dynamics of the aircraft assuming the stability derivatives estimated by pEst. Note that for the same input that was used before, the response is now totally different. The maximum sideslip angle developed for this case is only about 0.3 degrees while with the QUADPAN derivatives, approximately 3 degrees of sideslip developed. This is explained by the fact that the $C_{n\delta_r}$ estimate is an order of magnitude smaller for the flight test results than for the QUADPAN estimates. Furthermore, since the $C_{l\beta}$ estimate from the flight tests is two orders of magnitude below that predicted by QUADPAN, the aircraft does not continue rolling even when a sideslip angle is present. These characteristics are not typical of the dynamics observed during flight tests and conflict with the control strategies used by the pilots to control the aircraft. The difficulties in estimating these derivatives can be partially traced to measurement noise and unmodeled flexibility effects. Specifically in the

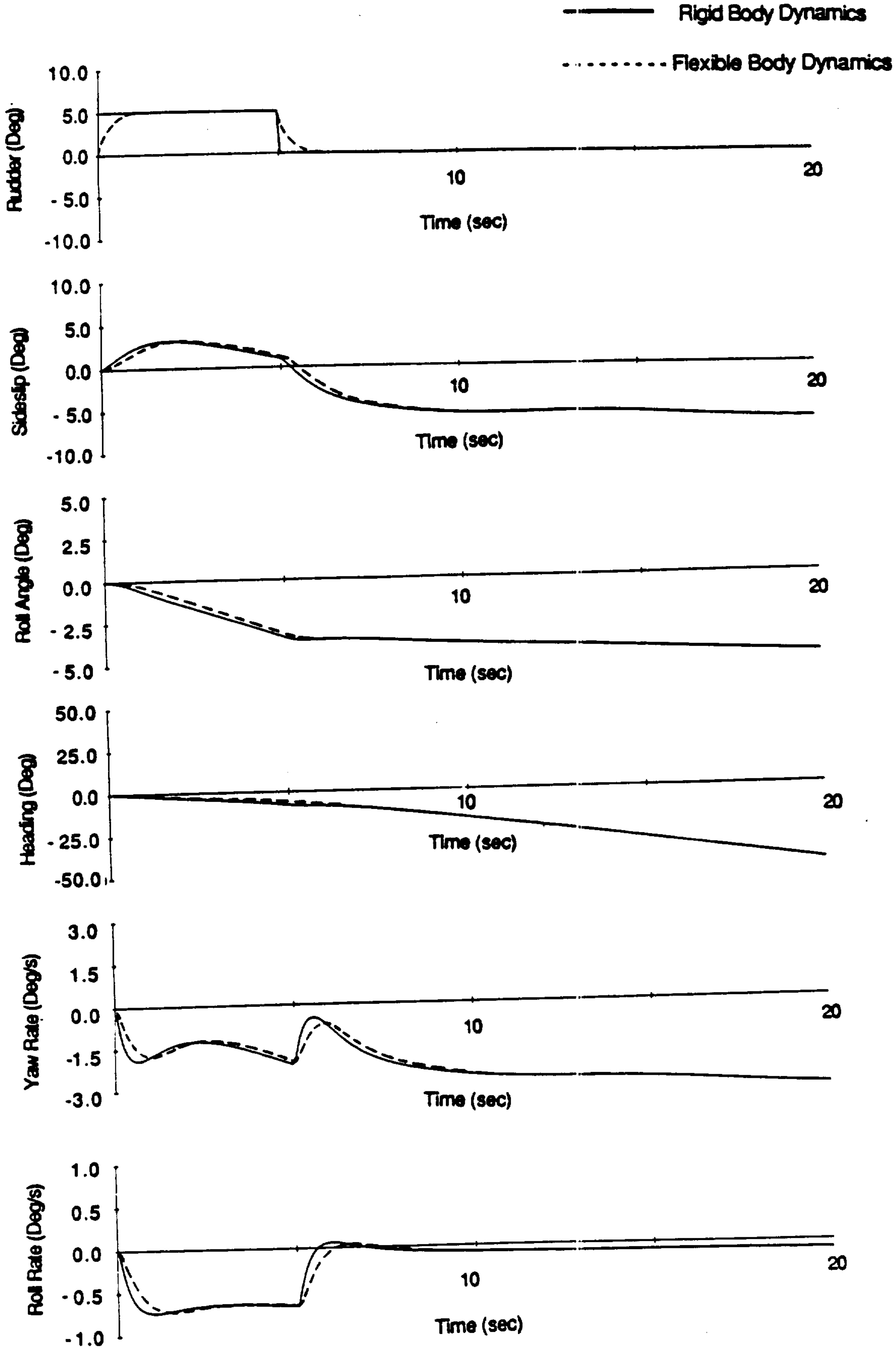

Figure 3-18 Open-Loop Lateral Dynamics
(Rigid-Body vs Flexible Dynamics)

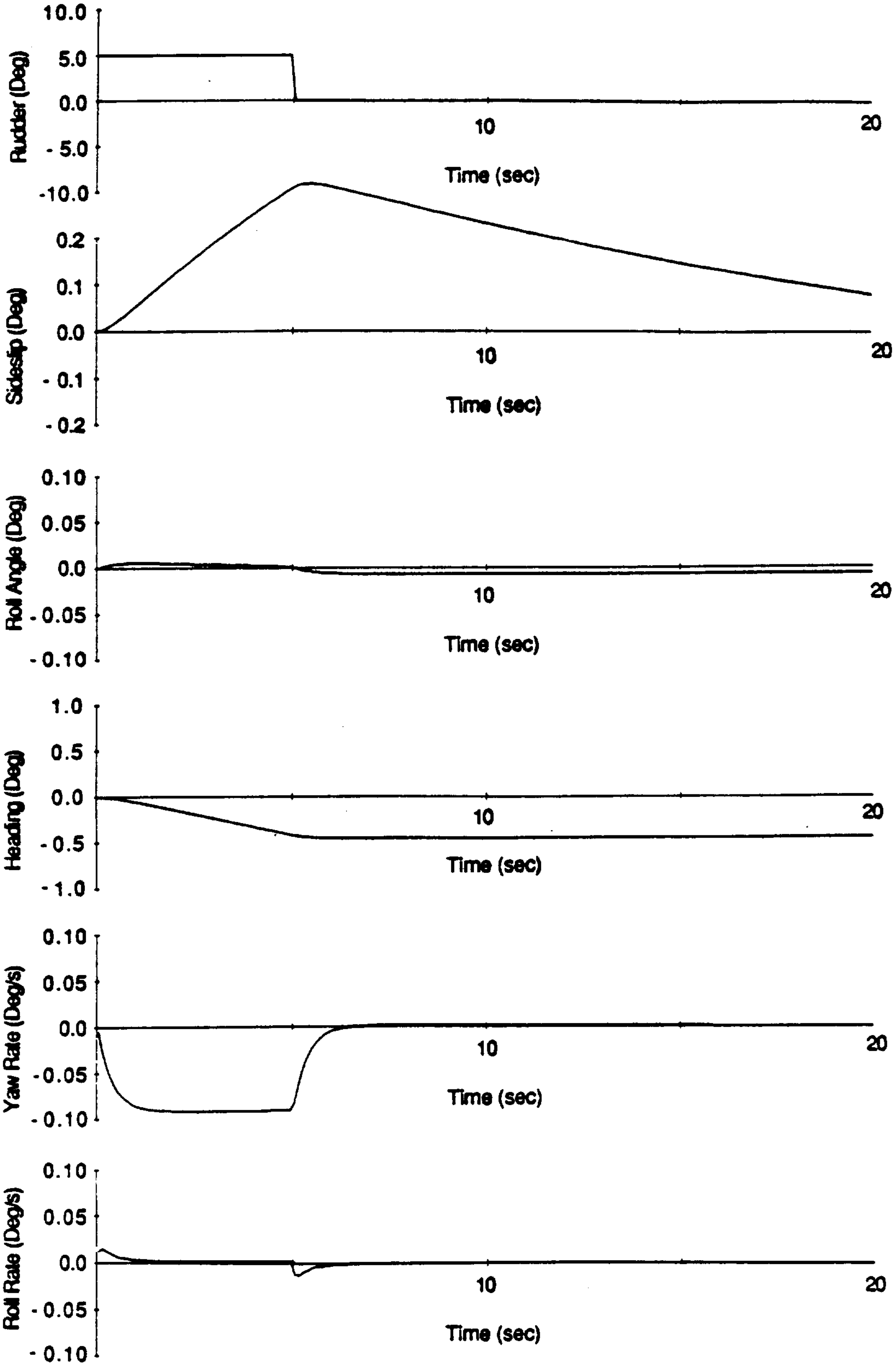

Figure 3-19 Open-Loop Lateral Dynamics
(With pEst Derived Stability Derivatives)

lateral axes, turbulence and localized thermals cause motions of the aircraft that the estimator tries to match with control inputs. The erroneous correlation of this noise to control inputs can cause unrealistic values to be estimated for the stability derivatives.

3.4.4.4 Closed-Loop Lateral Dynamics

A simulation of the lateral control system acting on rigid-body dynamics is illustrated in Figure 3-20. At 2.0 seconds into the simulation, a 5.0 degree heading change is commanded by the pilot. The autopilot commands a rudder deflection that causes the aircraft to yaw to the right. This causes the aircraft to roll right and therefore to steer towards the desired heading. As the aircraft approaches the commanded heading, the roll angle decreases and the aircraft settles on the desired heading.

Figure 3-21 illustrates the performance of the autopilot when the flexibility of the tailboom is included. Note that the flexibility effects cause the aircraft's response to be slightly more oscillatory than when rigid body dynamics are assumed. Furthermore, the autopilot commands slightly larger control inputs with the flexible tailboom. Considering the low bandwidth required for the lateral control system, these slight degradations in the aircraft's response are not considered significant enough to warrant a redesign of the lateral control system.

Because the stability derivatives derived from the flight test data do not produce a plausible aircraft response, the autopilot was not evaluated using these dynamics. Before further autopilot designs are investigated and before unmanned flights are attempted with the Light Eagle, it is advisable that the discrepancy between the stability derivatives estimated by QUADPAN and the stability derivatives estimated from flight data be resolved.

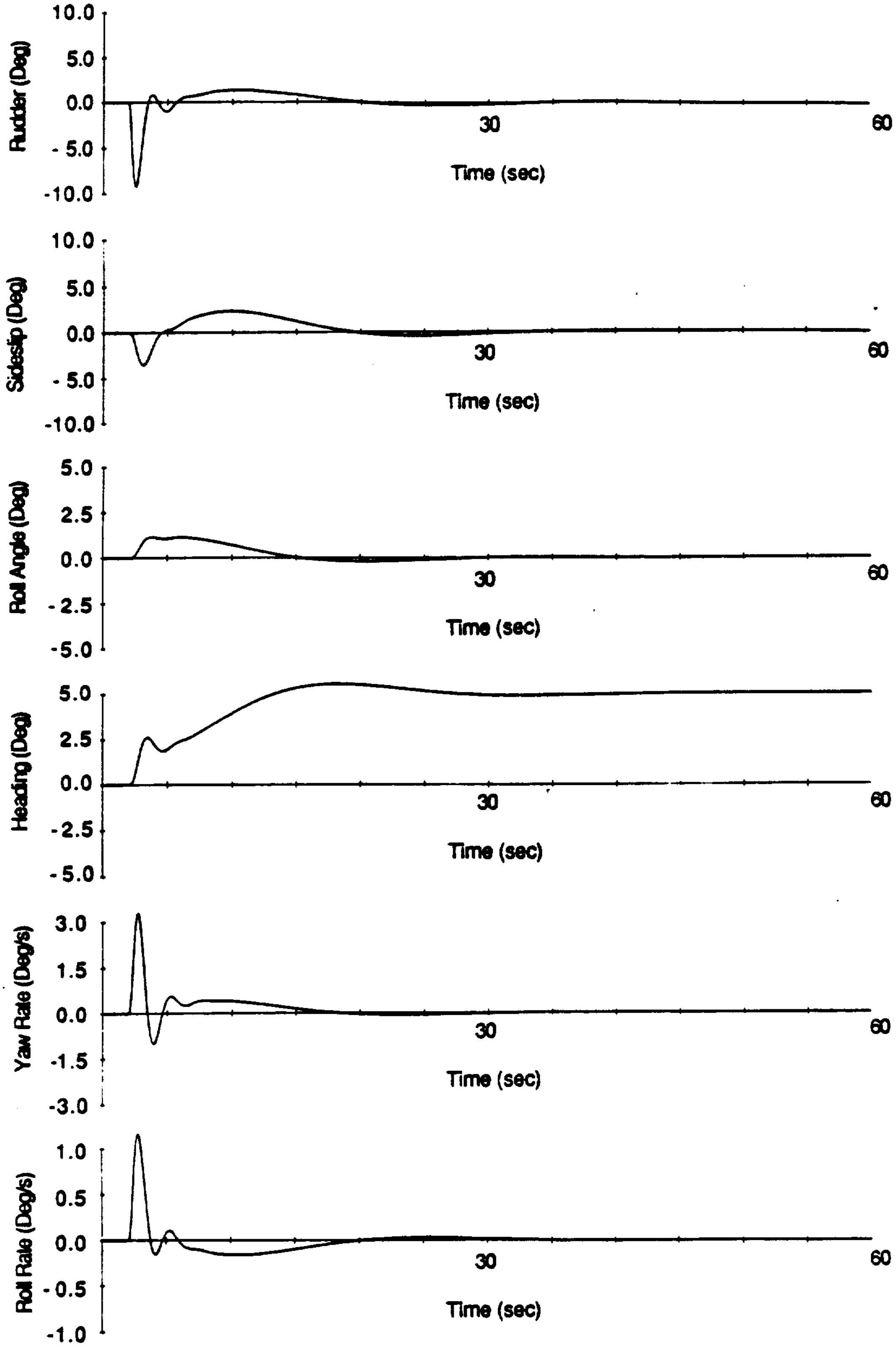

Figure 3-20 Lateral Control System Performance (Rigid Body Model)

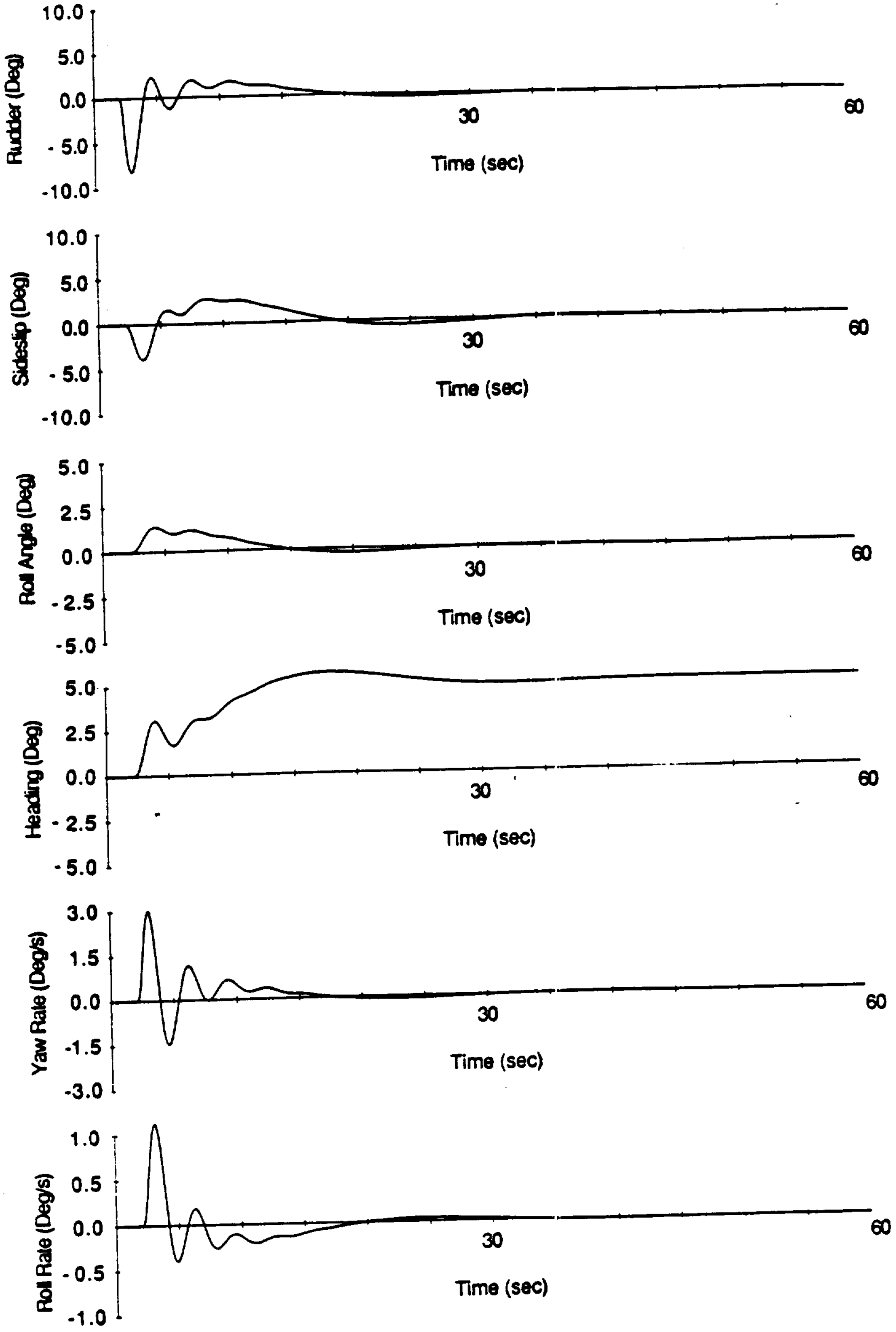

Figure 3-21 Lateral Control System Performance (Flexibility Effects Included)

3.5 Summary

It is clear from the parameter estimation results that unsteady aerodynamics and structural flexibility effects have a significant impact on the dynamics exhibited by both the Light Eagle and the Daedalus aircraft. Significant lags have been observed between when the rudder is deflected and when the resulting moment acts on the fuselage. This lag has been attributed to unsteady aerodynamics and structural flexibility. When the angle of attack of the rudder is quickly changed, a delay of approximately 0.14 seconds occurs before the lift on the rudder changes accordingly. After this force is generated, an additional lag of 0.3 seconds (due to tailboom flexibility) results before the moment is effectively applied to the fuselage. When these lags are accounted for in the parameter estimation program, better results are obtained for many of the stability derivatives.

The structural model of the aircraft should be extended to include the flexibility effects of the wing. Using the rigid body model for the wing, the parameter estimation program underestimates the value of $C_{l\beta}$ by two orders of magnitude. It is believed that when a sideslip is generated, the outer portion of the wing begins to roll into the turn and, due to the change in the direction of the lift vector, the heading begins to change. Only after a significant lag does the center section begin to roll. Since the rate gyros were mounted in the fuselage, they did not sense the roll rate until the center section began to roll. Due to the lag between when the sideslip was initiated and when the gyros sensed the roll rate, the estimator did not correlate the two signals; thus the estimate is quite poor.

The performance of the autopilot has been investigated in the light of the flexibility effects observed in the tailboom. Results indicate that the nominal autopilot design would not have exhibited acceptable performance due to these flexibility effects; however, with a simple augmentation of the compensation technique, adequate performance can be achieved. This result emphasizes that if a high altitude RPV is constructed that is similar in design to the Light Eagle, an accurate model of the aircraft's dynamics must first be developed and validated before the autopilot can be designed with any confidence.

An aeroelastic analysis has been performed on the aircraft's structure. When no forward airspeed is included in the analysis, the aircraft's structure is characterized by a significant number of closely spaced flexibility modes. (These modes are illustrated in Appendix B). Due to the close spacing of these modes and the relatively high frequencies involved in some of them, the observation of each mode is difficult in flight. Since the frequency content of aerodynamic surface deflections are not sufficient to excite many of these modes, other techniques must be devised. Possible means of excitation include placing small shakers onboard the aircraft, firing small rocket motors, and having ground personnel pull on ropes during the flight. Additional insight may be obtained by performing a ground-based vibration excitation test.

By extending the aeroelastic model to include the effects of forward flight speed, the variation in the dynamics of the aircraft with airspeed have been investigated. Three cases have been analyzed: (1) the aircraft flying at sea level with the nominal pitch inertia, (2) the aircraft flying at sea level with the pitch inertia increased 30%, (3) the aircraft flying at an altitude of 6000 meters with the nominal pitch inertia. Each case exhibits significantly different dynamics as the airspeed increases. From these findings, it is clear that if an aircraft similar to the Light Eagle is used as a high altitude RPV, a robust autopilot will be necessary to control the aircraft at each airspeed, at all altitudes, and with different payloads (different pitch inertias).

4.0 Power Measurements

One of the primary goals of the flight test program was to determine the power required to fly the Daedalus aircraft. This information allowed an estimate to be made of the endurance that each of the pilots would have in the aircraft. It was essential to verify that the pilots and the aircraft would have sufficient endurance and therefore sufficient range to complete the 119 km flight in Greece.

4.1 Data Collection and Processing

To estimate the power required to fly the Daedalus aircraft, the driveshaft's torque and RPM were recorded by the Tattletale Data Acquisition Computer at a 50 Hz rate. Airspeed, altitude, rudder deflection, and sideslip angle were also recorded but only at a 3.8 Hz rate (1/13 the rate of the power measurements) in order to save memory. A sample of the raw data is shown in Figure 4-1 where the torque and rotation rate signals have been multiplied to produce the power signal. The only filtering performed on this signal was the 15 Hz filter built into the Data Acquisition System; no post-processing filtering has been done. Considering this fact, the signal looks quite clean and relatively consistent. It is interesting to note in Figure 4-1 that the pilot appears to have one leg that is stronger than the other. This is evident by observing the power peak at the 68.75 second mark. At this point, the pilot's strong leg is going over the top of the pedaling stroke and therefore is producing a large torque and hence a large power value. His strong leg then continues to move forward until it reaches its maximum extension; at this point the torque and power are at a minimum. Next, his weak leg approaches the top of circle, its point of maximum torque. However, this power level is substantially below that produced by the other leg when it was in the same position in the pedalling cycle. This characteristic is fairly consistent throughout the data.

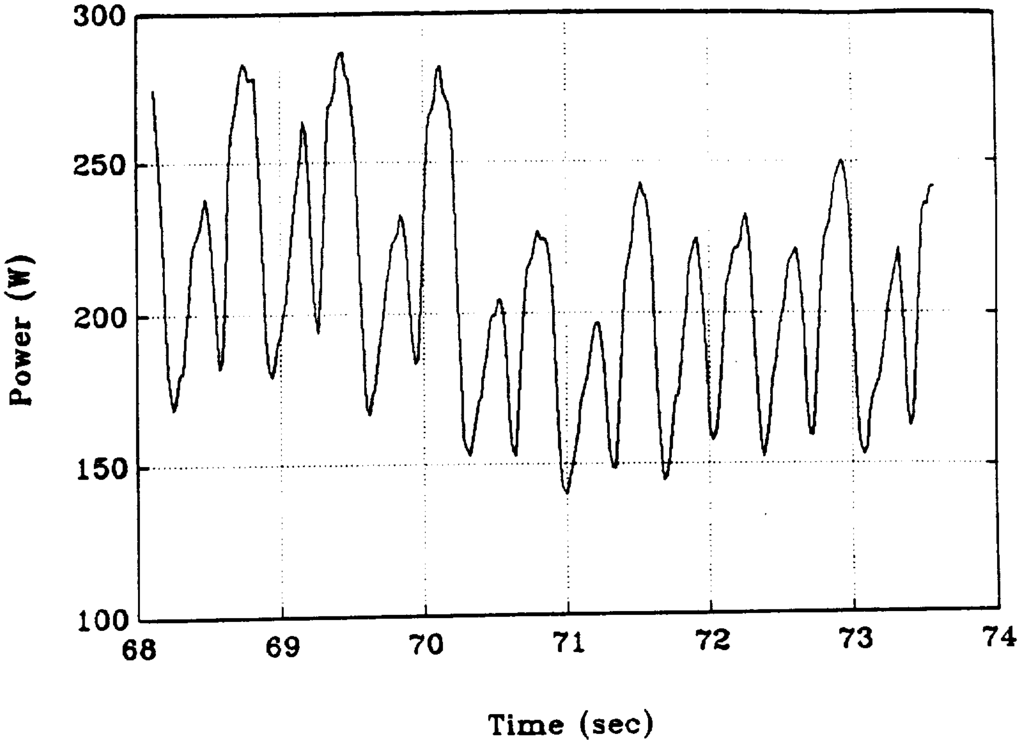

Figure 4-1 Raw Power Signal

The data collected during one of the flights (Flight 307B) is shown in Figures 4-2 through 4-5. In this flight, the pilot held the airspeed approximately constant while flying a nearly parabolic altitude trajectory. (The altitude is measured from the ground to the bottom of the fuselage). Note that the power increases as the pilot adds energy to gain altitude and airspeed. Conversely, the power decreases when the pilot descends or loses airspeed. Due to these effects, it is difficult to determine the actual power being produced by the pilot over a given time interval. Therefore, instead of analyzing the data as power output, the power signal has been integrated and processed as energy. By doing this, the energy put into increasing the altitude (potential energy) and increasing the airspeed (kinetic energy) can be compensated for. The integrated power signal, without the altitude and airspeed compensation, is shown in Figure 4-6. It is clear that at the beginning of the flight, as the pilot gains altitude, the power required is quite high, as evidenced by the steep slope during this time. Conversely, as he loses altitude at the end of the flight, the slope of the line, and hence the power required,

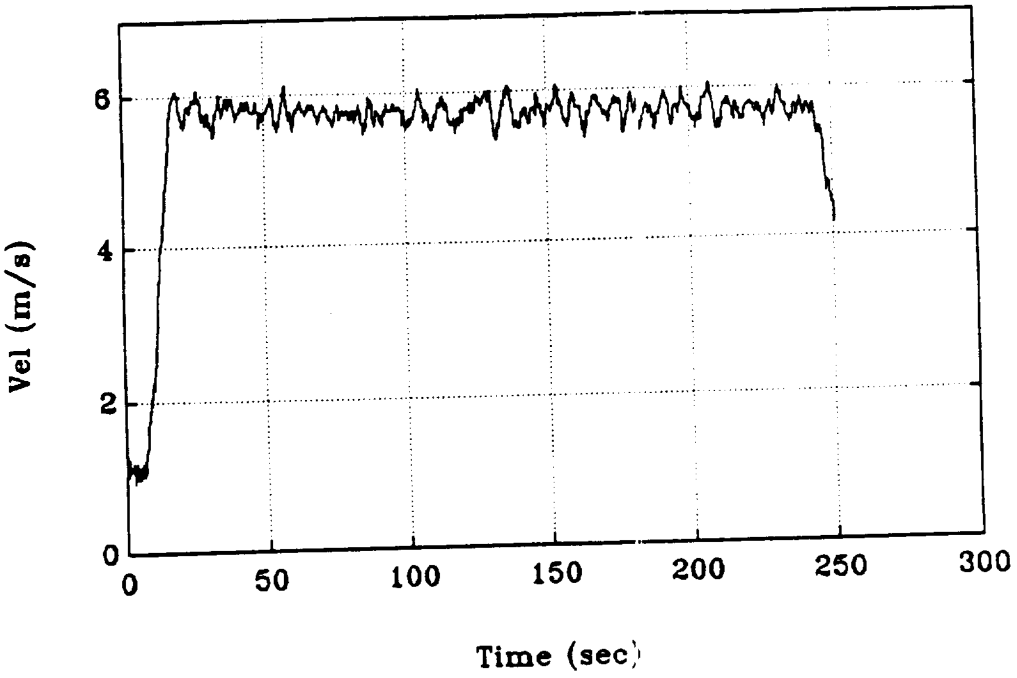

Figure 4-2 Flight 307B Velocity Time History

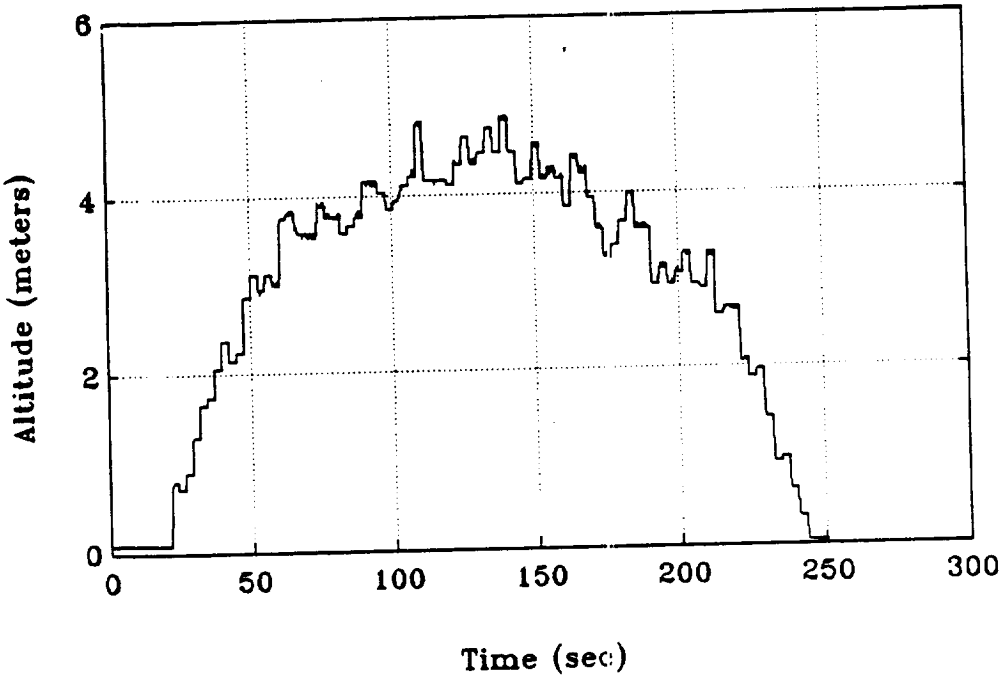

Figure 4-3 Flight 307B Altitude Time History

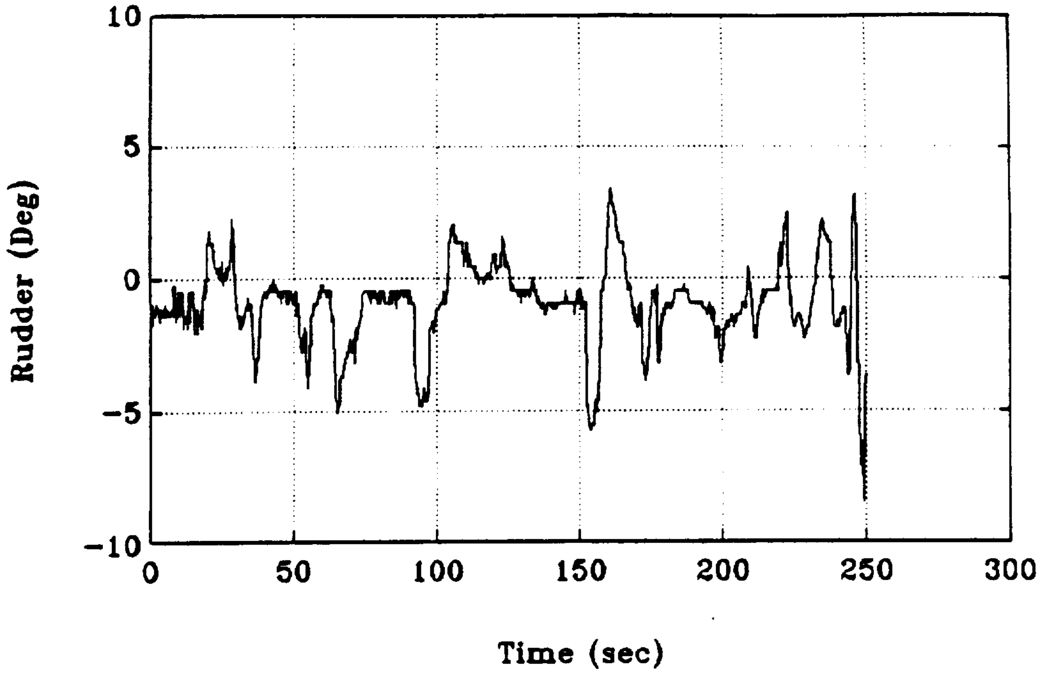

Figure 4-4   Flight 307B Rudder Time History

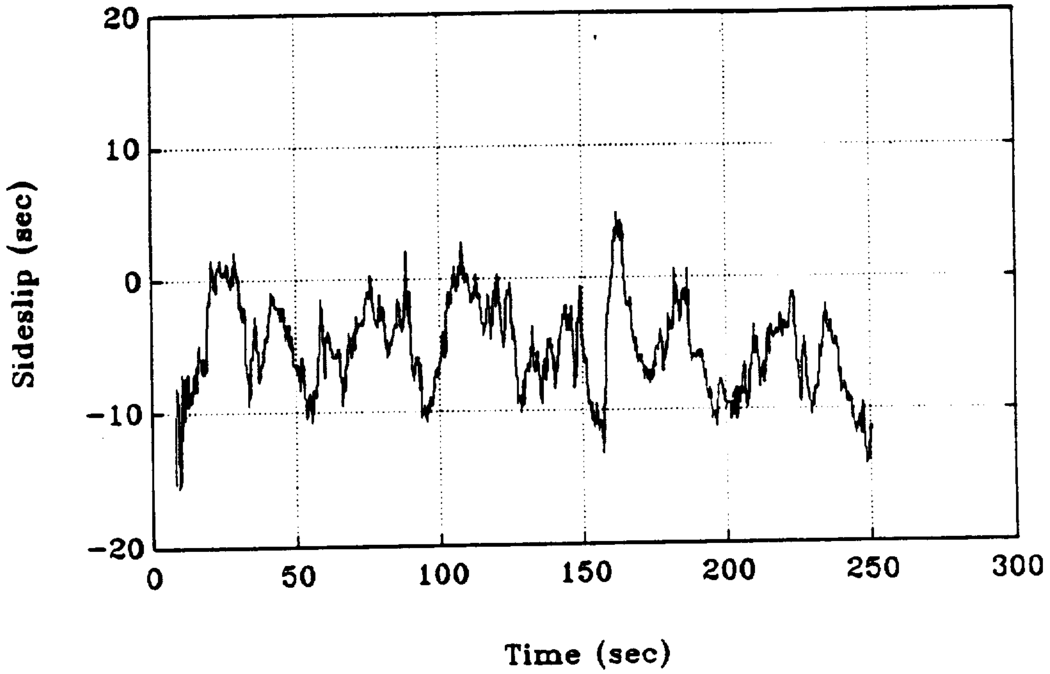

Figure 4-5   Flight 307B Sideslip Time History

decreases significantly. To correct this problem, the integrated power signal has been compensated for the altitude and airspeed energy effects (Figure 4-7). After these compensations are made, the slope of the energy line becomes much more constant, and thus its slope represents the power required to fly the aircraft at constant airspeed and altitude. This power level is equivalent to the power required to overcome the drag of the aircraft.

Though the energy time history has been compensated for variations in the kinetic energy due to changes in airspeed, no attempt has been made to correct for the decrease in the aircraft's efficiency if the flight speed is higher or lower than the optimum. Due to this variation in the efficiency, the resulting power estimate may be biased if the airspeed varies considerably over the period of time being analyzed. However, if the airspeed is fairly consistent over a relatively long period of time, the change in the power level can be correlated with the different airspeeds, and thus the most efficient airspeed can be observed. Fortunately, during each of the sections of the flights analyzed, the airspeed is sufficiently constant that the power estimates should not be biased and thus the efficiency of the aircraft can be observed at the different airspeeds.

The compensated energy plot for Flight 307B (Figure 4-7) has been numerically fitted with a straight-line to allow the slope of the plot and thus the power level to be estimated. Through this process, it has been discovered that the pilot was supplying 157 Watts (0.21 Hp) of power, somewhat less than the theoretical estimate of the power required. It is believed that errors in calibrating the power measurement sensors resulted in the low power estimates. Though the absolute magnitude of the power measurements are low, the estimates are still quite useful in observing relative changes in the power with airspeed and altitude.

To evaluate the quality of the straight-line numerical fit, the error between the

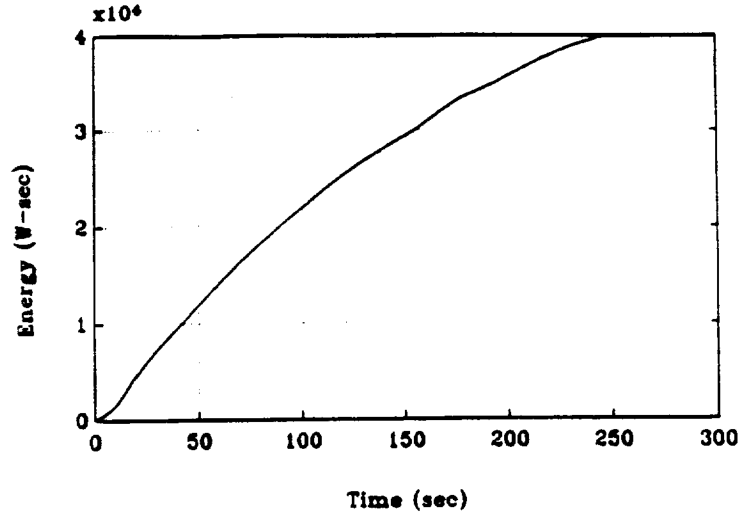

Figure 4-6 Flight 307B Uncompensated Energy Time History

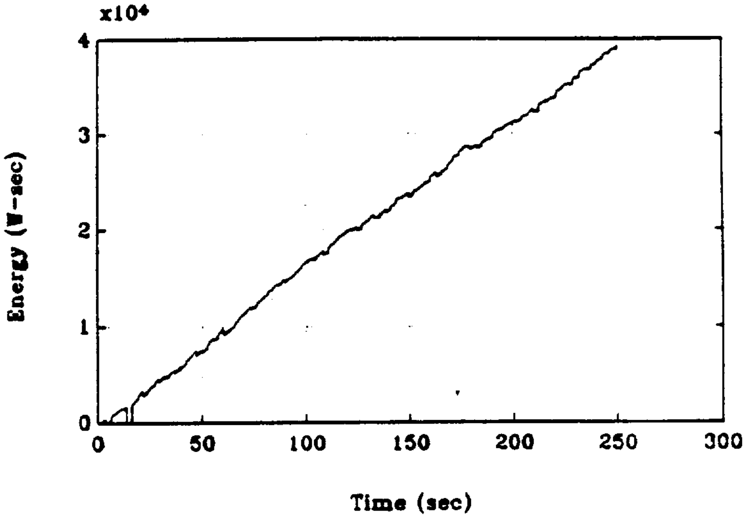

Figure 4-7 Flight 307B Compensated Energy Time History

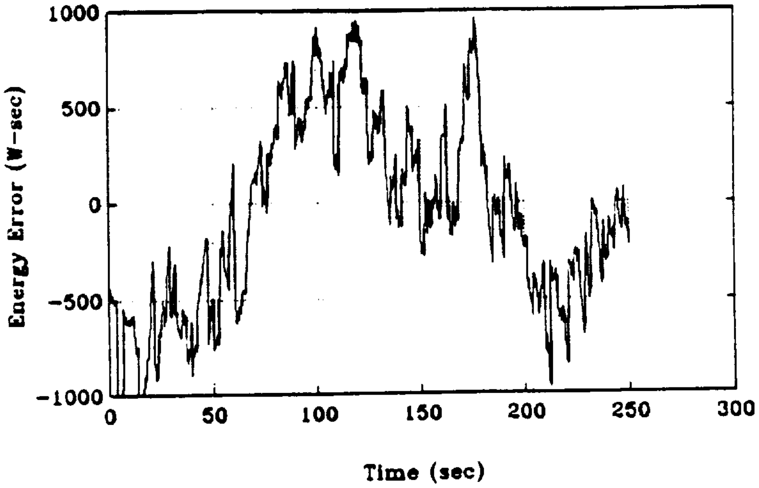

Figure 4-8 Flight 307B Energy Error After Numerical Fit

compensated energy line and the numerically-fitted line has been plotted in Figure 4-8 (see previous page). Quantitatively, the fit is quite good; however, the remnant is certainly not white noise. Indeed, the error appears to be correlated with altitude and implies that the power decreases with altitude. This effect is examined more closely in the following section.

4.2 Altitude Effects

The data from Flight 307A are shown in Figures 4-9 through 4-12. The purpose of this flight was to investigate ground effect; therefore, the pilot flew at four different altitudes but at approximately the same airspeed. (The altitude is measured from the ground to the bottom of the fuselage). Note that throughout the flight, the rudder deflection and the sideslip angle are relatively small. Though the sideslip indicates a fairly constant five degree offset, it is believed that the calibration was slightly biased. This finding is consistent with sideslip angle data from other test flights.

The raw data from Flight 307A has been processed in the manner described above. Figure 4-13 shows the integrated power signal with no compensation. It is clear from the figure that the resulting signal is not linear but contains several changes in slope which represent changes in the power level input. By compensating the energy plot for the energy put into increasing the aircraft's altitude and airspeed, it can be seen from Figure 4-14 that these compensations do in fact improve the linearity of the integrated power signal.

The data have been analyzed in four separated sections corresponding to the four different altitudes flown during this test flight. The resulting periods are from 35 to 90 seconds, 135 to 180 seconds, 220 to 280 seconds, and 360 to 500 seconds. Estimates of the slope during each of these periods are listed in Table 4-1 along with the mean and standard deviations of the airspeed, altitude, rudder deflection, and sideslip angle. Note that the

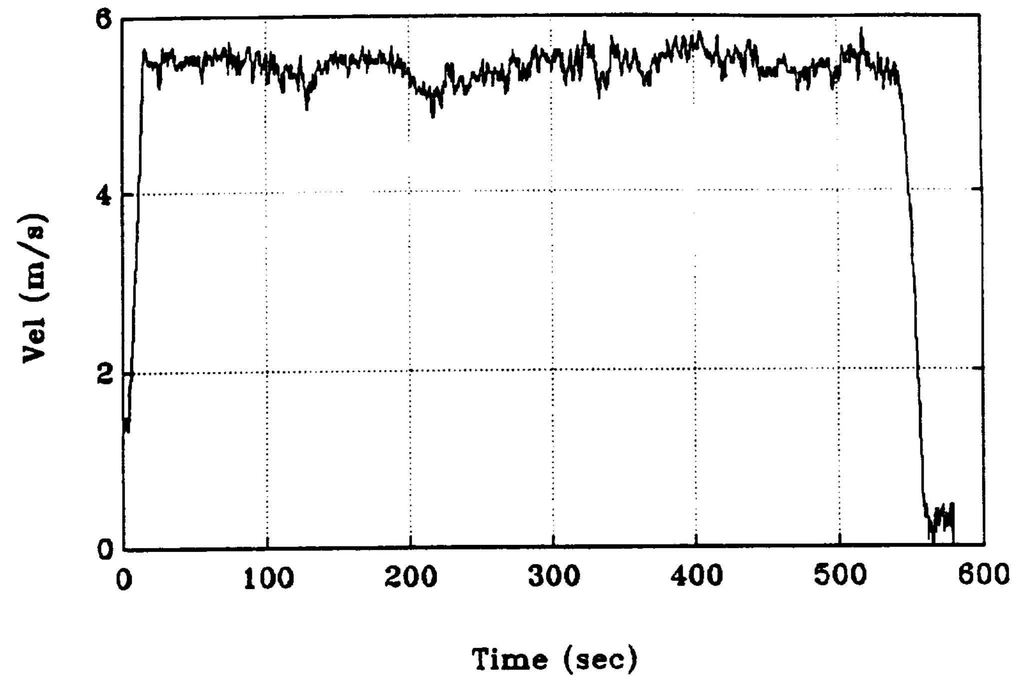

Figure 4-9 Flight 307A Velocity Time History

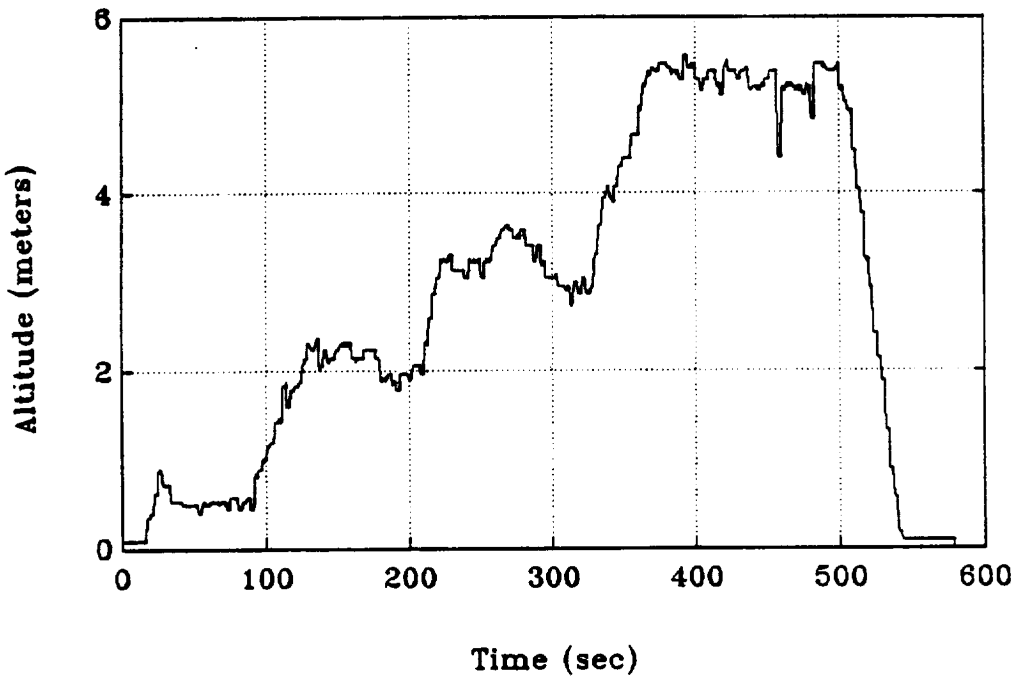

Figure 4-10 Flight 307A Altitude Time History

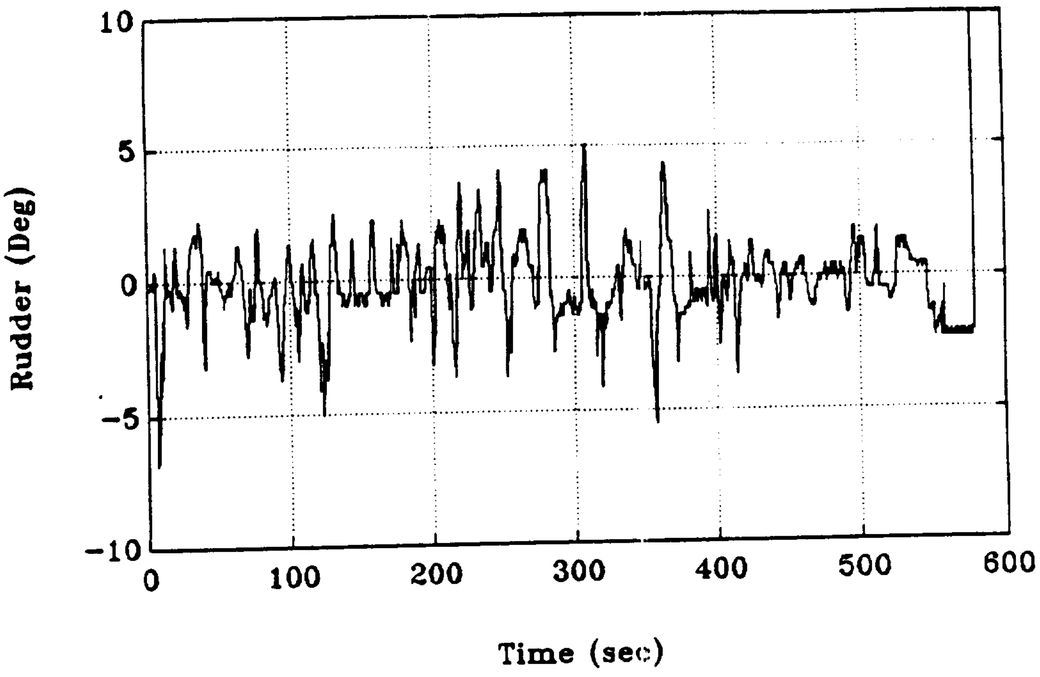

Figure 4-11 Flight 307A Rudder Time History

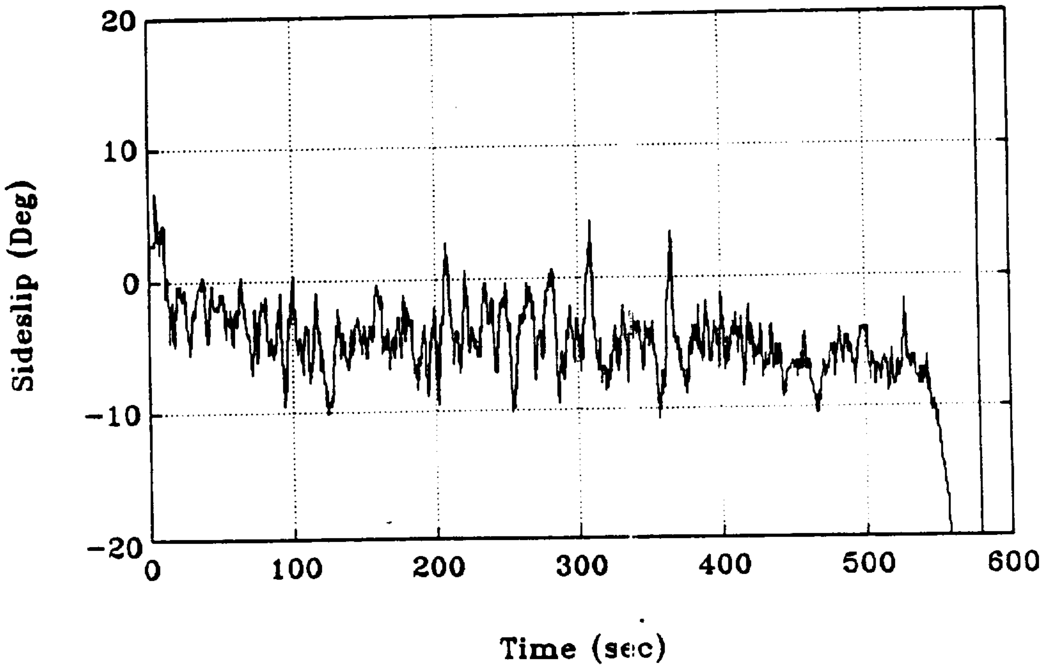

Figure 4-12 Flight 307A Sideslip Time History

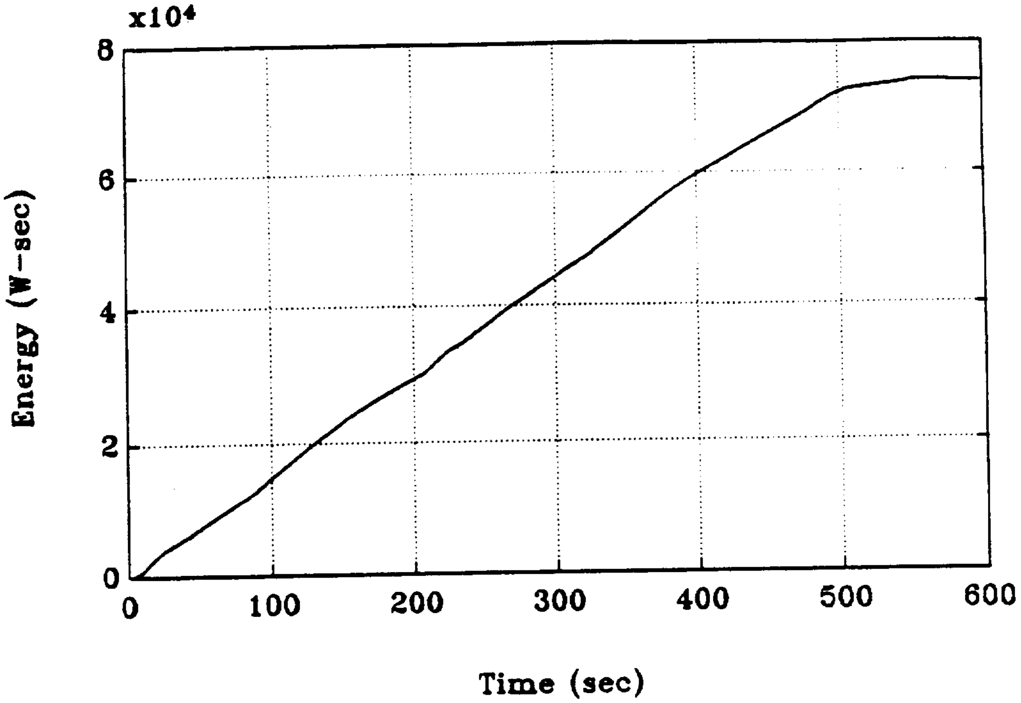

Figure 4-13 Flight 307A Uncompensated Energy Time History

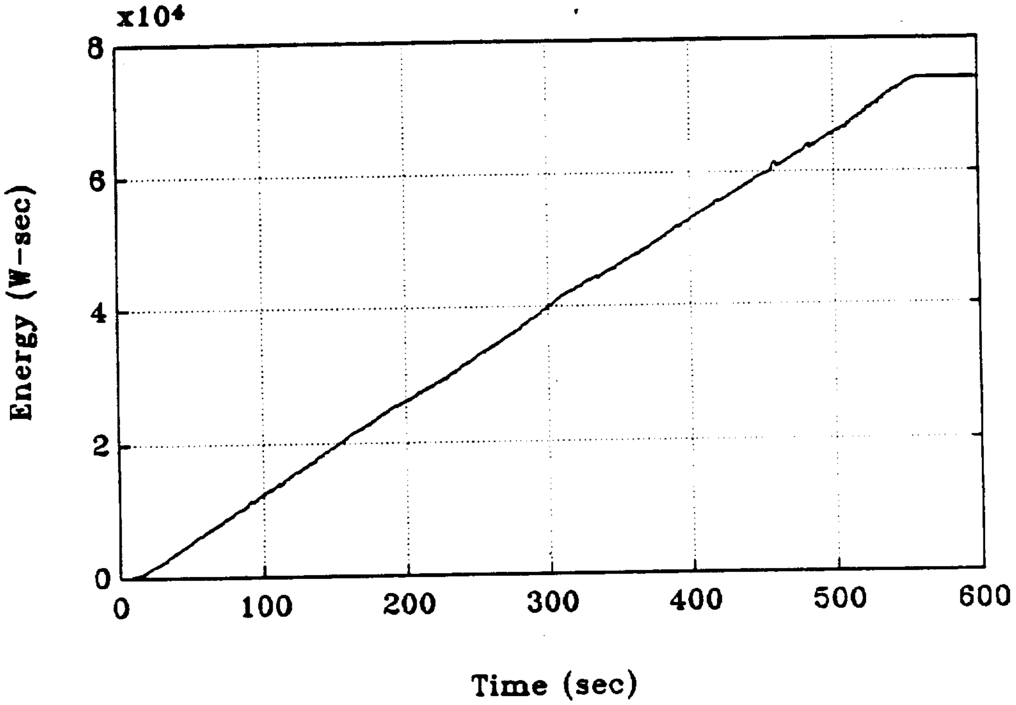

Figure 4-14 Flight 307A Compensated Time History

airspeed is fairly constant over the entire flight. Also listed in the table are the standard deviations of the errors between the compensated energy data and the straight line fit to that data.

	Lowest Alt (35 to 90 sec)	Low-Middle Alt (135 to 180 sec)	Middle Alt (220 to 280 sec)	High Alt (360 to 500 sec)
Altitude (meters)				
Mean	0.56	2.20	3.31	5.28
Std Dev	0.130	0.088	0.185	0.191
Airspeed (meters/sec)				
Mean	5.50	5.47	5.29	5.46
Std Dev	0.086	0.072	0.123	0.145
Rudder Defl (Deg)				
Mean	-0.34	- 0.15	0.90	- 0.70
Std Dev	1.23	0.93	1.64	1.12
Sideslip (Deg)				
Mean	-3.21	- 4.06	- 3.63	- 5.69
Std Dev	2.08	1.53	2.35	2.00
Energy Error (W-sec)				
Std Dev	79.1	97.7	75.3	132.0
Power (W)				
Mean	141.0	143.1	137.3	130.6

Table 4-1 Data Summary for Flight 307A

By examining the power estimates at each altitude, it is clear that the power generally decreases with altitude. The exception to this is at the very lowest altitude. This suggests that two effects are actually present: a "classical ground effect" and an "inverse ground effect". It is believed that the inverse ground effect is caused by turbulence in the Earth's boundary layer. The diameters of the largest boundary layer eddies (which represent most of the turbulent kinetic energy) are proportional to altitude; thus, closer to the ground, the energy in the boundary layer becomes concentrated in eddies of smaller and smaller diameter. Eventually the eddies become sufficiently small (approximately 0.5 cm) that they trip the laminar boundary layer on the wing. As a result, a greater percentage of the wing area is covered with turbulent flow. Consequently, the aircraft's drag and the power required both increase as the aircraft flies closer to the ground.

From the data it also appears that at extremely low altitudes, the classical ground effect overrides the inverse ground effect and results in a slight decrease in power due to the slight reduction in induced drag. Further data supporting these hypotheses are presented later in this chapter.

There is some subjective data that also supports this theory. When Kanellos Kanellopoulos flew the Daedalus aircraft from Crete to Santorini, Greece, he observed that when flying at 12 meters (39 ft), the required power was less than when flying closer to the surface of the water. Also, during the crossing of the English Channel by the Gossamer Albatross, Bryan Allen was almost forced to abort the flight due to the high power required when flying at an altitude of 1.5 meters (5 ft). However, when he increased his altitude to 4.5 meters (15 ft), he found that the required power decreased and he was thus able to complete the flight [9]. Although most of the upper surface of the Albatross wing was probably turbulent (judging from the particular airfoil on the Albatross), it is possible that the atmospheric turbulence during Allen's flight was of sufficient intensity to trip the laminar boundary layer on the bottom surface of the wing. This could explain the higher power at the lower altitude.

For each of the four sections analyzed in Flight 307A, the errors between the compensated energy data and the straight-line fits have been plotted in Figures 4-15 through 4-18. From these plots, it is clear that the residual errors are quite small. Note that a 74.6 W-sec (0.1 Hp-sec) error in energy is equivalent to a 7.6 cm (3 inch) error in altitude for a 30.9 kg (68 lbs) aircraft and a 65.1 kg (152 lbs) pilot. This altitude error is equivalent to the

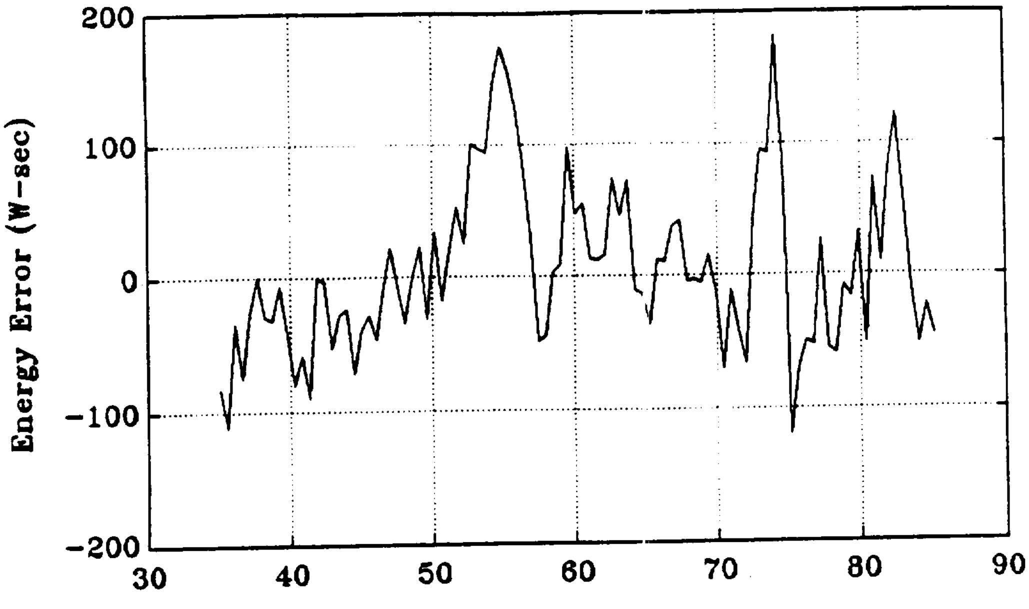

Figure 4-15 Flight 307A Energy Error After Numerical Fit (Lowest Altitude)

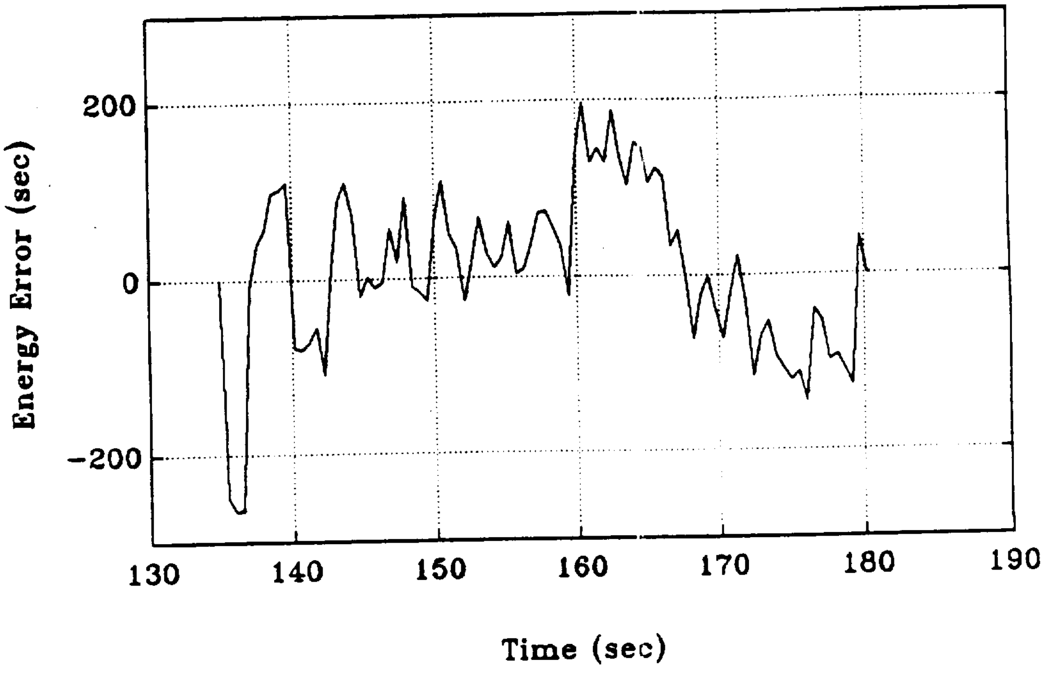

Figure 4-16 Flight 307A Energy Error After Numerical Fit (Low-Middle Altitude)

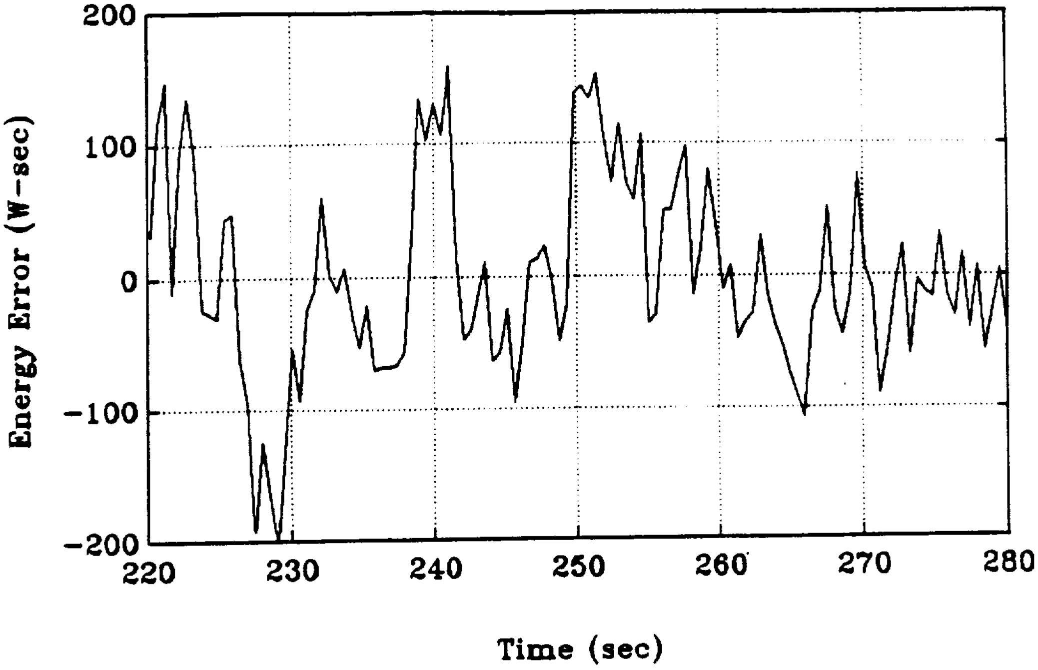

Figure 4-17 Flight 307A Energy Error After Numerical Fit (Middle Altitude)

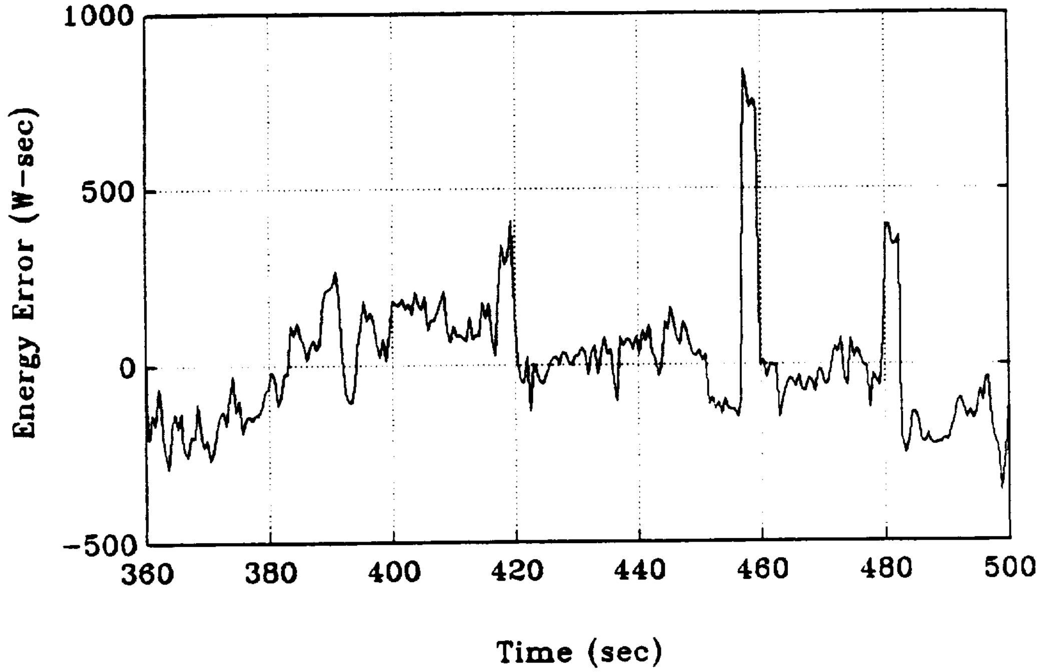

Figure 4-18 Flight 307A Energy Error After Numerical Fit (High Altitude)

quantization of the altimeter. Since these errors are remarkably small, the confidence in the power estimates is quite high.

4.3 Discussion of Possible Instrumentation Errors

Bias and scale factor errors in the altimeter measurements have been investigated to determine if they could produce results that might be misconstrued as the "inverse ground effect". Figures 4-19 and 4-20 illustrate that this is not possible. In these drawings, it is assumed that the pilot is initially flying at altitude h_1, and then adds extra power to increase his altitude to h_2. The darker line indicates the actual energy required to perform this maneuver. If a positive scale factor error exists in the altimeter, the change in altitude and thus the change in potential energy is overestimated; consequently, when the data is compensated for the potential energy effects, it is actually overcompensated (the lighter line in Figure 4-19). During the gradual increase in altitude, the scale factor error would thus cause the slope of the energy line to decrease and thus cause the power to be underestimated. However, when the aircraft is at constant altitude, the altimeter scale factor error does not cause a change in slope; it simply causes a constant offset to the compensated energy line. Consequently, the scale factor error will not cause an error in the power estimate while the aircraft is flying at constant altitude. By examining Flight 307A, it is clear that the aircraft is flying at a nearly constant altitude during the times over which the data has been processed. Therefore, an altimeter scale factor error would not explain the "inverse ground effect" seen in the data.

Similarly a bias in the altimeter measurement would not affect the power estimate. The bias would simply shift the level of the entire energy data but would not change the slope of the line. Since the slope is not affected, the power estimate is not affected and again, would not explain the "inverse ground effect" observed.

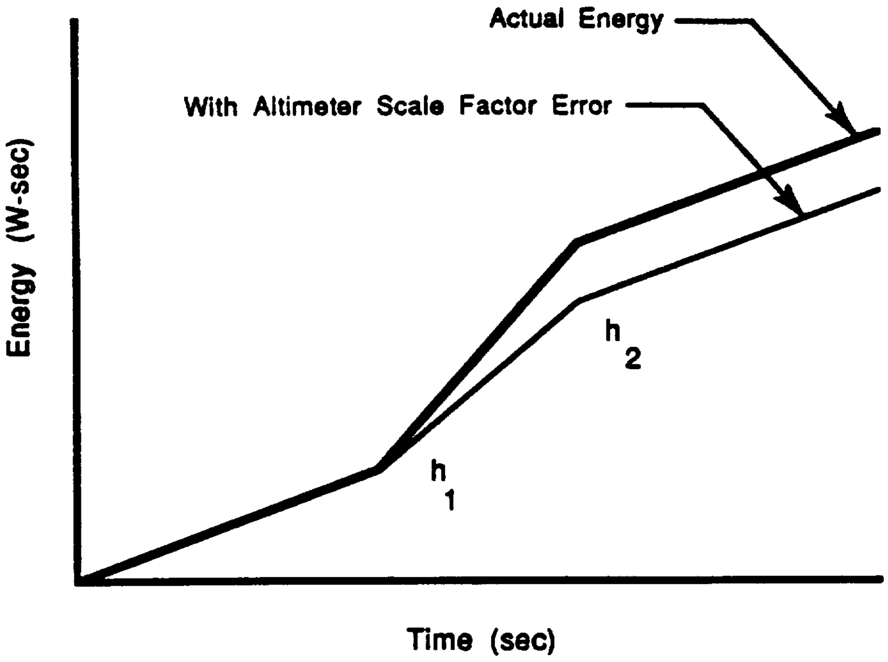

Figure 4-19 Altimeter Scale Factor Error Effects

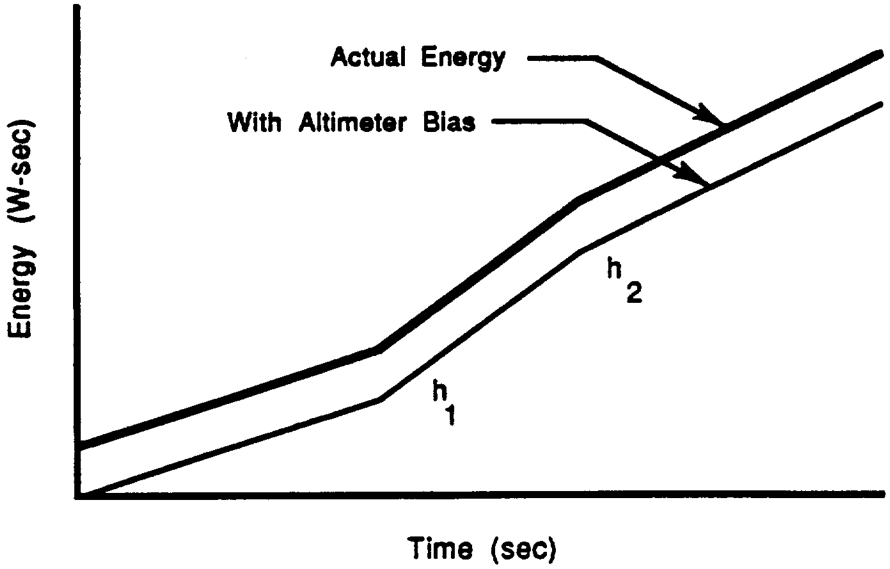

Figure 4-20 Altimeter Bias Error Effects

4.4 Airspeed Effects

The remainder of the flights were made at different airspeeds; therefore, it is difficult to observe the effect of altitude on these power estimates until the airspeed effects are first accounted for. The data from all of these flights have been analyzed in the same manner as described above; each flight has been analyzed in sections over which the altitude and airspeed are approximately constant (see Appendix C for raw data of Flights 307C, 307D, and 307E). These results are summarized in Table 4-2. To allow the airspeed effects to be separated from the altitude effects, each power estimate has been plotted in Figure 4-21 versus altitude and airspeed. In this figure, the values next to each data point are the corresponding power

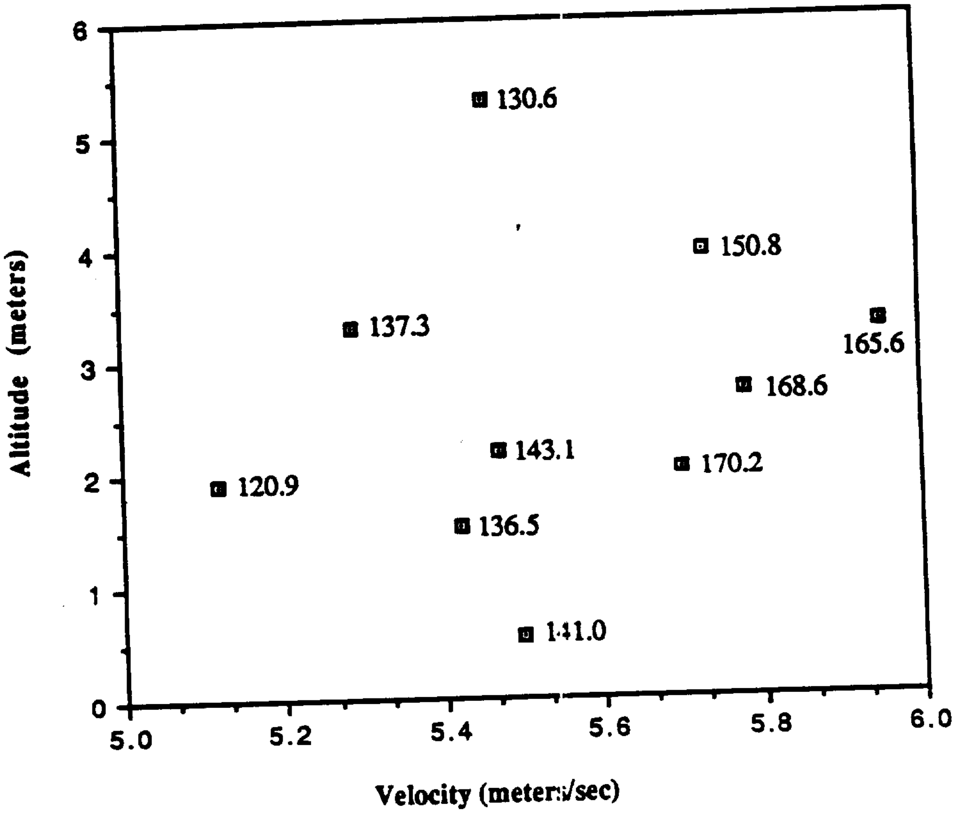

Figure 4-21 Power Estimates vs Airspeed and Altitude

Flight	Analysis Period (secs)	Velocity (meter/sec)		Altitude (meters)		Rudder (Deg)		Sideslip (Deg)		Energy Error	Power
		Mean	Std Dev	Mean	Std Dev	Mean	Std Dev	Mean	Std Dev	Std Dev (W-sec)	(W)
307A 1	35 - 90	5.50	0.086	0.56	0.130	-0.34	1.23	-3.21	2.08	79.1	141.0
2	135 - 180	5.47	0.072	2.20	0.088	-0.15	0.93	-4.06	1.53	97.7	143.1
3	220 - 280	5.29	0.123	3.31	0.185	0.90	1.64	-3.63	2.35	75.3	137.3
4	360 - 500	5.46	0.145	5.28	0.191	-0.70	1.12	-5.69	2.00	132.0	130.6
307B 1	30 - 70	5.78	0.122	2.72	0.762	-1.58	1.25	-5.34	2.35	208.9	168.6
2	70 - 200	5.73	0.140	3.94	0.488	-0.91	1.51	-4.85	3.44	299.1	150.8
3	200 - 240	5.70	0.116	2.03	0.796	-0.37	1.33	2.10	0.25	185.0	170.2
307C 1	0 - 350	5.12	0.182	1.92	0.637	-0.62	2.88	-1.16	4.50	470.0	120.9
2	400 - 500	5.95	0.235	3.29	0.347	-1.02	3.77	-4.39	4.69	253.6	165.6
3	550 - 700	5.42	0.152	1.52	0.570	-0.93	4.17	-5.42	4.50	440.1	136.5
307D 1	100 - 150	5.51	0.210	3.00	0.661	-2.35	4.50	-6.85	6.34	551.3	161.8
2	170 - 230	5.63	0.169	2.40	0.430	-0.17	2.61	-3.01	4.08	379.0	147.8
307E 1	31 - 70	5.43	0.164	1.12	0.201	-0.77	2.74	-5.76	3.97	164.1	161.2
2	90 - 130	5.36	0.122	1.75	0.396	1.06	3.13	-1.17	5.79	350.6	184.1
3	150 - 190	5.51	0.235	3.18	0.384	-3.80	3.65	-8.77	7.80	2461.8	107.7
4	230 - 290	5.50	0.158	2.33	0.433	-1.05	2.09	-4.58	4.10	387.2	155.5
5	290 - 360	5.52	0.146	1.48	0.485	-0.25	1.92	-2.88	3.39	429.7	172.5
6	360 - 410	5.49	0.210	2.68	0.472	1.42	3.51	0.77	6.96	391.7	124.4
7	500 - 560	5.45	0.180	1.50	0.360	-0.41	2.25	0.58	4.04	402.1	181.2
8	560 - 600	5.66	0.152	2.45	0.689	-0.60	2.62	-2.54	4.82	596.8	127.8
9	600 - 690	5.69	0.174	1.67	0.396	-0.14	2.12	-3.41	3.02	446.1	165.7

Table 4-2 Summary of Flight Data

estimates for that section of the flight. The data substantiates the hypothesis that the power decreases with altitude. The two exceptions to this statement are Flight 307C, subsection 3 and Flight 307A, subsection 1. Though these portions of the flights were performed at low altitudes, the power is actually less than for other flights made at higher altitudes but at approximately the same airspeeds. This suggests that the classical ground effect may be present and may cause a slight reduction in the power required when the aircraft is extremely close to the ground.

The data from sections of Flights 307D and 307E (see Table 4-2) have not been plotted in Figure 4-21 due to the widely varying power estimates. The decision to ignore these results was made only after carefully examining the time histories of the energy input, the altitude, the airspeed, the rudder deflections, and the sideslip angles. Flights 307D and 307E were the last flights performed on the day the power measurements were made; as a result, they may have been performed during a time of increased thermal activity and therefore greater turbulence. This increase in turbulence has been observed to start quite abruptly on Edwards Dry Lakebed and to vary considerably from location to location on the lakebed. This second effect has been attributed to the damp condition of the lakebed, a result of the frequent rains. The damper portions tended to be darker and therefore tended to exhibit greater thermal effects; furthermore, the water vapor rising off the damper portions also tended to create vertical air movements. The effect of these air movements can be seen in the data from these two flights (see Appendix C for the raw data from Flights 307D and 307E). In Figure 4-22, the energy time history for Flight 307D shows that the power input is very inconsistent; data from previous flights exhibited a much more linear behavior. It is clear that between 80 and 100 seconds, the power required to fly the aircraft is nearly zero, as indicated by the nearly horizontal slope. This event is also accompanied by a rapid increase in altitude. Consequently, it appears that the aircraft was flying through a upward moving thermal. However, after the aircraft leaves this thermal, the associated sink is encountered, thereby increasing the power required to fly the aircraft. This explains the high power estimate for the first section of Flight 307D. Because of these disturbances, this data point was deleted from Figure 4-21. The power estimate for the second section of this flight is not unreasonable; however, the thermal effects clearly cause abrupt changes in the slope of the energy time history. These effects raise doubt as to the accuracy of the power estimate made during this time; as a result, this estimate has also been deleted from Figure 4-21.

Similarly, data from Flight 307E appears to be significantly distorted by thermal effects as demonstrated by the short term changes in the slope of the energy plot and by the poor fit in the energy error plot (Figure 4-23). To demonstrate these effects, the data from this flight have been evaluated over nine separate intervals (Table 4-2). This analysis shows that the power drops significantly as the aircraft gains altitude and increases greatly when altitude is lost; however, the decrease in power with altitude is too large to be explained by the inverse ground effect theory. This implies that strong air currents are being generated that cause the aircraft to gain and lose altitude. The lower power estimates occur during periods of updrafts; the higher power estimates occur during periods of downdrafts.

Thus having eliminated the anomalous data from Flights 307D and 307E, it is now clear from Figure 4-21 that the power indeed decreases with altitude and increases with airspeed. Due to the lack of data at consistent altitudes, it is difficult to totally separate the effects of altitude from those of airspeed; however, it does appear that the lowest power estimate occurs at the lowest airspeed. This is not totally expected. Classical aircraft theories predict that below the optimum airspeed, the power should start to increase due to the high angle of attack required. From the limited quantity of Daedalus power data, this effect cannot be observed. If a greater range of airspeeds are tested in the future, this effect, however, will become evident.

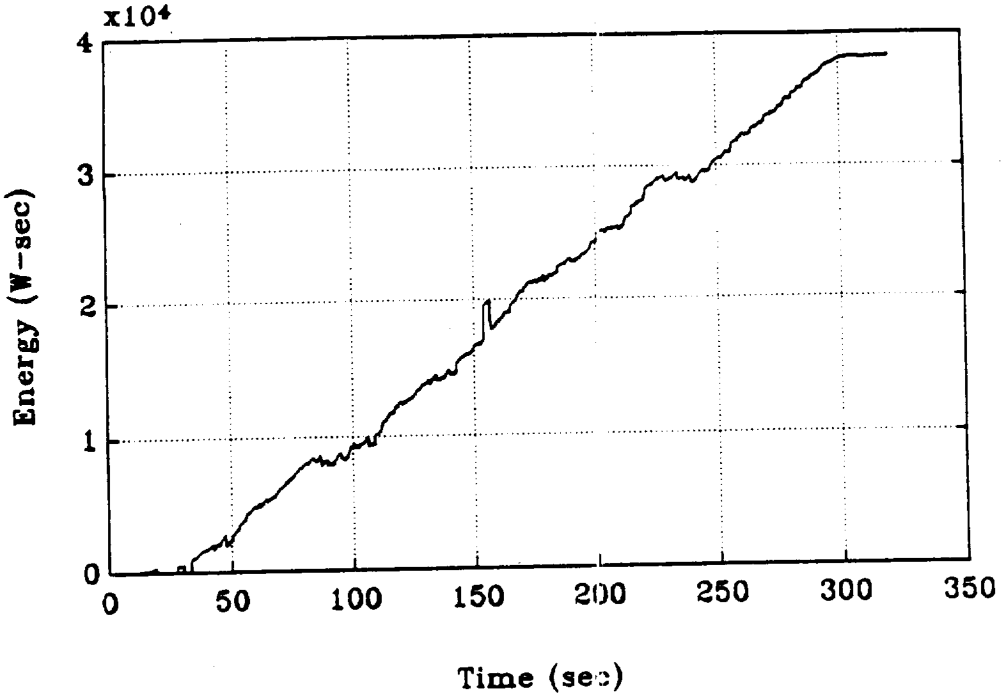

Figure 4-22 Flight 307D Compensated Energy Time History

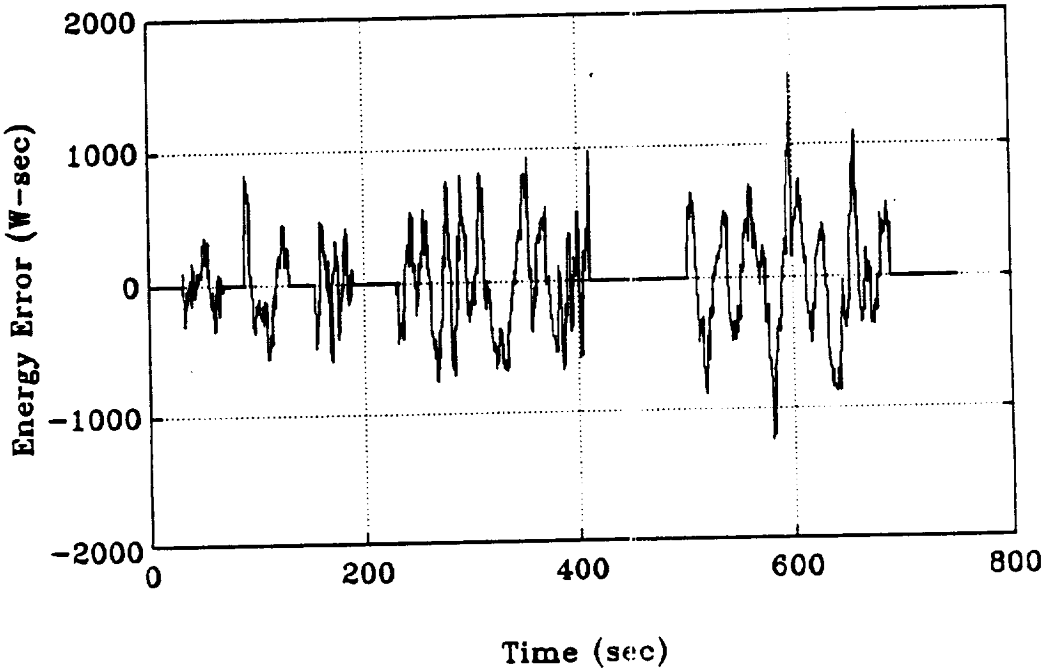

Figure 4-23 Flight 307E Energy Error After Numerical Fit

To compare the powers estimated from the flight data with those predicted by the theoretical drag computations on the aircraft, the theoretically derived powers for a range of airspeeds have been listed in Table 4-3. Note that no altitude effects are assumed in the calculations. It is obvious that these powers are higher than those estimated from the flight data; it is believed that the flight data is underestimated due to calibration errors in the torque and RPM sensors. From Table 4-3, it is also clear that the optimum theoretical airspeed is higher than that observed in the flight data. Realizing this, the lift coefficient for the flight with the lowest airspeed (in Table 4-2) has been calculated and found to be 2.43. This C_L is higher than the airfoil is predicted to be capable of generating; consequently, it is believed that a scale factor error was present in the airspeed sensor.

Velocity (meters/sec)	Power Required (W)
5.00	175.3
5.25	167.9
5.50	161.9
5.75	156.7
6.00	153.7
6.25	151.4
6.50	149.9
6.75	149.9
7.00	151.4
7.25	153.7
7.50	157.4
7.75	161.9
8.00	167.9
8.25	174.6
8.50	182.0
8.75	191.0
9.00	201.4

Table 4-3 Theoretically Derived Power Estimates

C-2

The scale factor error in the airspeed sensor should not affect the technique used to analyze the power data since each flight was divided and analyzed during periods of constant airspeed. As a result, during each flight section, the energy compensations due to changes in airspeed are relatively small; therefore, errors in these compensations should be extremely small.

The ability to find the optimum airspeed is not compromised by the error in the airspeed sensor. The voltage into the panel meter that displayed airspeed was the same voltage measured by the Data Acquisition System; thus by comparing the two signals, the corresponding meter reading for the optimum airspeed can be determined. Consequently, the pilot can fly the aircraft at this reading even though it is a relative and not an absolute value of airspeed.

4.5 Summary

An effective set of sensors and data collection equipment has been assembled that can precisely measure the power required to fly a human powered aircraft. A useful and accurate technique has been developed for processing the resulting data. This technique involves integrating the power supplied by the pilot and then compensating this total energy for the power required to change altitude (potential energy) and the power required to change airspeed (kinetic energy). Due to problems in calibrating the sensors, the power estimates for the data are not accurate in an absolute sense; however, the estimates are quite precise and can be used to observe small changes in the power required to fly the aircraft. This is quite useful for flight testing human powered aircraft since it is allows the measurement of the power reduction obtained by flying at the optimal airspeed and altitude, by reducing the weight of the aircraft, and by making various minor changes to the airframe.

Though the classical ground effect may be present when the Daedalus aircraft is flying at extremely low altitudes, there is insufficient data to fully substantiate this finding. However, the results from the flight tests do indicate that the power required to fly the aircraft actually tends to decrease with altitude. This is contrary to classical ground effect theories; however, it correlates with the subjective observations of Kanellos Kanellopoulos during his 119 km flight between Crete and Santorini, Greece and of Bryan Allen during his flight across the English Channel in the Gossamer Albatross.

It is hypothesized that this inverse ground effect is caused by turbulence in the Earth's boundary layer. The diameters of the largest boundary layer eddies (which represent most of the turbulent kinetic energy) are proportional to altitude; thus, closer to the ground, the energy in the boundary layer becomes concentrated in eddies of smaller and smaller diameter. Eventually the eddies become sufficiently small (approximately 0.5 cm) that they trip the laminar boundary layer on the wing. As a result, a greater percentage of the wing area is covered in turbulent flow. Consequently, the aircraft's drag and the power required both increase as the aircraft flies closer to the ground.

From the power data it is obvious that the airspeed at which the aircraft is flown has a significant effect on the power required; however, due to the distortion of the data from inverse ground effect, it is difficult to obtain a consistent relationship between airspeed and power. The power for the Daedalus aircraft does increase as the airspeed increases; however, there is not sufficient data to observe the increase in power when the aircraft is flying slower than the optimum airspeed.

5.0 Summary and Conclusions

1. A sophisticated data acquisition system has been assembled that can be used on aircraft where size and weight are extremely critical. The system and the associated sensors weigh less than one kilogram.

2. By comparing turns performed using only the rudder with turns performed using both rudder and ailerons, it has been substantiated that ailerons are not particularly effective in controlling turns for human powered aircraft. The long wingspan of the Light Eagle combines with the drag due to the aileron deflections to generate significant adverse yaw moments. The resulting yaw rate is in the direction that, through C_{l_r}, will cause the aircraft to initially roll in the direction opposite to the desired turn. The net effect is large adverse yaw rates and very small roll rates in the commanded direction.

3. Unsteady aerodynamics and the structural flexibility of the Light Eagle and Daedalus aircraft cannot be ignored when performing parameter estimations on flight data.

a. Significant lags have been observed between when the rudder is deflected and when the resulting moment acts on the fuselage. This lag has been attributed to unsteady aerodynamics and structural flexibility. When the angle of attack of the rudder is quickly changed, a delay of approximately 0.14 seconds occurs before the lift on the rudder changes accordingly. After this force is generated, it causes the tailboom to deflect significantly before the moment is effectively applied to the fuselage. Thus an additional lag of approximately 0.3 seconds results. When these lags are accounted for in the parameter estimation program, better estimates are obtained for many of the stability derivatives.

b. The structural model of the aircraft should be extended to include the flexibility effects of the wing. Using the rigid body model for the wing, the parameter estimation program underestimates the value of $C_{l\beta}$ by two orders of magnitude. However, significant wing flexibility has been observed during flight tests. When a sideslip is generated, the outer portion of the wing begins to roll into the turn and, due to the change in the direction of the lift vector, the heading begins to change. Only after a significant lag does the center section begin to roll. Since the rate gyros were mounted in the fuselage, they did not sense the roll rate until the center section began to roll. Due to the lag between when the sideslip was initiated and when the gyros sensed the roll rate, the estimator did not correlate the two signals; thus the $C_{l\beta}$ estimate was quite poor.

4. The performance of the autopilot has been investigated in the light of the flexibility effects observed in the tailboom. Results indicate that the nominal autopilot design would not have exhibited acceptable performance due to these flexibility effects; however, with a simple augmentation of the compensation technique, adequate performance could have been achieved. This result emphasizes that if a high altitude RPV is constructed that is similar in design to the Light Eagle, an accurate model of the aircraft's dynamics must first be developed and validated before the autopilot can be designed with any confidence.

5. An aeroelastic analysis has been performed on the aircraft's structure. When no forward airspeed is included in the analysis, the aircraft's structure is characterized by a significant number of closely spaced flexibility modes. (These modes are illustrated in Appendix B). Due to the close spacing of these modes and the relatively high frequencies involved in some of them, the observation of each mode is difficult in flight. Since the frequency content of aerodynamic surface deflections are not sufficient to excite many of these modes, other techniques must be devised. Possible means of excitation include placing small shakers

onboard the aircraft, firing small rocket motors, and having ground personnel pull on ropes during the flight. Additional insight may be obtained by performing a ground-based vibration excitation test.

By extending the aeroelastic model to include the effects of forward flight speed, the variation in the dynamics of the aircraft with airspeed have been investigated. Three cases have been analyzed: (1) the aircraft flying at sea level with the nominal pitch inertia, (2) the aircraft flying at sea level with the pitch inertia increased 30%, and (3) the aircraft flying at an altitude of 6000 meters with the nominal pitch inertia. Each case exhibits different dynamics as the airspeed increases. From these findings, it is clear that if an aircraft similar to the Light Eagle is used as a high altitude RPV, a robust autopilot will be necessary to control the aircraft at each airspeed, at all altitudes, and with different payloads (different pitch inertias).

6. a. A useful and precise technique has been developed for measuring and processing the power data for human powered aircraft. Due to problems in calibrating the torque and RPM sensors, the power estimates for the data are not accurate in an absolute sense; however, the estimates are quite precise and can be used to observe small changes in the power required to fly the aircraft. This is quite useful for flight testing human powered aircraft since it is often desirable to determine the power reduction obtained by flying at the optimal airspeed and altitude, by reducing the weight of the aircraft, and by making various minor changes to the airframe.

b. Though the classical ground effect may be present when the Daedalus aircraft is flying at extremely low altitudes, there is insufficient data to fully substantiate this finding. However, the results from the flight tests do indicate that the power required to fly the aircraft actually tends to decrease with altitude. This is contrary to classical ground effect theories;

however, it correlates with the subjective observations of Kanellos Kanellopoulos during his 119 km flight between Crete and Santorini, Greece and of Bryan Allen during his flight across the English Channel in the Gossamer Albatross.

It is hypothesized that this inverse ground effect is caused by turbulence in the Earth's boundary layer. The diameters of the largest boundary layer eddies (which represent most of the turbulent kinetic energy) are proportional to altitude; thus, closer to the ground, the energy in the boundary layer becomes concentrated in eddies of smaller and smaller diameter. Eventually the eddies become sufficiently small (approximately 0.5 cm) that they trip the laminar boundary layer on the wing. As a result, a greater percentage of the wing area is covered with turbulent flow. Consequently, the aircraft's drag and the power required both increase as the aircraft flies closer to the ground.

c. From the power data it is obvious that the airspeed at which the aircraft is flown at has a significant effect on the power required; however, due to the distortion of the data from inverse ground effect, it is difficult to obtain a consistent relationship between airspeed and power. The power for the Daedalus aircraft does increase as the airspeed increases; however, there is not sufficient data to observe the increase in power when the aircraft is flying slower than the optimum airspeed.

References

[1] Drela M., "Low Reynolds Number Airfoil Design for the MIT Daedalus Prototype, A Case Study", AIAA Journal of Aircraft, 1987.

[2] Bussolari, S.R., Langford J.S., Youngren H.H., "Flight Research with the Daedalus Prototype, Phase II Report", Massachusetts Institute of Technology, Spring 1987.

[3] Boyd W.N., Effect of Chordwise Forces and Deformations and Deformations due to Steady Lift on Wing Flutter, Ph.D. Thesis Stanford University, SUDAAR No. 508, December 1977.

[4] Hill, M.L., "Introducing the Electrostatic Autopilot", Astronautics and Aeronautics, Vol. 10, No. 1, Nov 1972, pp 22-31.

[5] Murray J.E., Maine R.E., pEst Version 2.1 User's Manual, NASA TM 88280, September 1987.

[6] Maine R.E., Iliff K.W., MMLE 3 User's Manual, NASA TP 1563, November 1980.

[7] Youngren, H. H. , Bouchard, E. E., Coopersmith, R. M., Quadrilateral Element Panel Method Users Manual, Lockheed California Company Report 30563, 1984.

[8] Fung Y.C., An Introduction to the Theory of Aeroelasticity, Dover, 1969.

[9] Allen, Bryan, National Geographic, Nov 1979, Vol 156, No 5, p 643.

Appendix A Finite Element Model of the Light Eagle Aircraft

Element Material Property Data

Element #	E-Mod.	ν	ρ	J	I_s	I_t	A
	[N/m^2]	[ ]	[kg/m^3]	[m^4]	[m^4]	[m^4]	[m^2]
1	5.5E11	0.3	1.4E03	4.0E-06	2.96E-11	2.96E-06	1.4E-04
2	1.49E11	0.3	1.73E03	1.65E-07	1.59E-06	2.96E-07	2.85E-04
3	6.8E11	0.3	4.08E03	1.94E-08	1.0E-06	1.3E-08	6.36E-05
4	1.49E11	0.3	1.73E03	1.65E-07	1.59E-06	2.96E-07	2.85E-04
5	6.8E11	0.3	4.08E03	1.94E-08	1.0E-06	1.3E-08	6.36E-05
6	4.35E12	0.3	1.4E03	4.0E-08	6.59E-04	6.59E-04	2.85E-04
7	7.82E10	0.3	1.4E03	4.0E-08	2.96E-07	2.96E-07	2.85E-04
8	5.5E13	0.3	1.4E03	4.0E-08	2.96E-07	2.96E-07	1.4E-04
9	5.7E11	0.3	1.4E03	1.1E-08	1.67E-06	5.0E-09	4.6E-05
10	5.7E11	0.3	1.4E03	1.1E-08	1.67E-06	5.0E-09	4.6E-05
11	1.1E12	0.3	1.6E03	4.0E-08	2.96E-04	2.96E-04	1.4E-04
12	5.5E13	0.3	1.4E03	4.0E-08	2.96E-07	2.96E-07	1.4E-04
13	5.7E11	0.3	1.4E03	1.1E-08	5.0E-09	1.67E-06	4.6E-05
14	5.7E11	0.3	1.4E03	1.1E-08	5.0E-09	1.67E-06	4.6E-05
15	1.1E12	0.3	1.4E02	1.0E-06	1.0E-06	1.0E-06	1.4E-04
16	2.1E11	0.3	7.8E03	1.0E-12	5.2E-13	5.2E-13	3.5E-06
17	2.1E11	0.3	7.8E03	1.0E-12	5.2E-13	5.2E-13	3.5E-06
18	1.39E12	0.3	1.73E03	3.79E-08	1.14E-07	1.3E-08	6.36E-03
19	1.72E11	0.3	1.73E03	7.75E-08	1.69E-06	2.96E-07	2.85E-04
20	1.95E10	0.3	1.4E03	4.0E-08	2.96E-07	2.96E-07	2.85E-04

Apparent Mass Terms

m_{app} of the main wing and elevator in z-direction = $\rho_{air} A_{z,i} b_i$

$$A_{z,i} = \frac{\pi \bar{c}_i^2}{4}$$

where $A_{z,i}$ is the cross-sectional area of the cylinder with the diameter equal to the average chord length of the profile section to which the apparent mass term is added, ρ_{air} is the air density at sealevel, and b_i is the spanwise length.

Element #	m_{app} [kg]	c_i [m]	b_i [m]
2	5.51	1.202	3.96
3	4.53	0.998	4.72
4	5.51	1.202	3.96
5	4.53	0.998	4.72
9	0.19	0.415	1.14
10	0.19	0.415	1.14
18	4.53	0.998	4.72
19	5.51	1.202	3.96
20	5.51	1.202	3.96
21	4.53	0.998	4.72
22	0.19	0.415	1.14
23	0.19	0.415	1.14

Rudder apparent mass terms in the y-direction:

$m_{app} = \rho_{air} A_{y,i} b_i$

$$A_{y,i} = \frac{\pi \bar{c}_i^2}{4}$$

i=1; $A_i = 0.448\ m^2$

i=2; $A_i = 0.552\ m^2$

Similar to the above mentioned procedure the apparent mass terms in the y-direction were added to the nodal point mass loading of the Finite-Element program.

Additional apparent mass terms of all aerodynamic surfaces.

m_{add} in x, y, and z-direction = $\rho_{air} A_{x,y,z,i} b_i$

These apparent mass terms have to be consistently included in all directions, because the enclosed volume of air inside of the aerodynamic surfaces affects motions in all directions.

Appendix B Mode Shapes

The mode shapes were derived from eigen-analysis of the free-free aircraft. Reference condition for the eigen-analysis was the pre-loaded aircraft (1-g level flight) with apparent mass loading on the main wings and empennage.

Natural Structural Modal Frequencies at Different Load Factors

	Load Factor	Frequency [Hz]
Mode 7	1.0	0.625
	2.0	0.605
	2.5	0.592
	3.0	0.579
	3.5	0.561
Mode 8	1.0	0.838
	2.0	0.838
	2.5	0.837
	3.0	0.836
	3.5	0.834
Mode 9	1.0	0.985
	2.0	0.964
	2.5	0.948

	3.0	0.934
	3.5	0.907
Mode 10	1.0	1.352
	2.0	1.311
	2.5	1.278
	3.0	1.231
	3.5	1.170
Mode 11	1.0	1.552
	2.0	1.334
	2.5	1.228
	3.0	1.133
	3.5	1.170
Mode 12	1.0	2.547
	2.0	2.449
	2.5	2.388
	3.0	2.362
	3.5	2.250
Mode 13	1.0	2.824
	2.0	2.768

	2.5	2.727
	3.0	2.702
	3.5	2.630
Mode 14	1.0	2.998
	2.0	2.896
	2.5	2.834
	3.0	2.788
	3.5	2.630
Mode 15	1.0	3.904
	2.0	2.659
	2.5	2.271
	3.0	1.976
	3.5	1.811

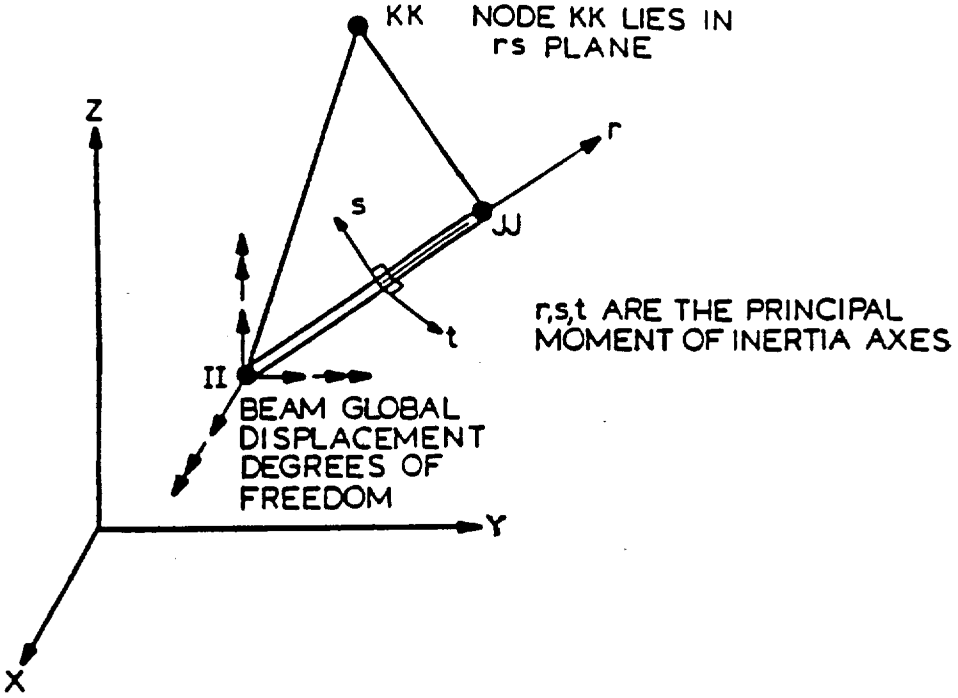

Figure A1 Beam Element Coordinate System

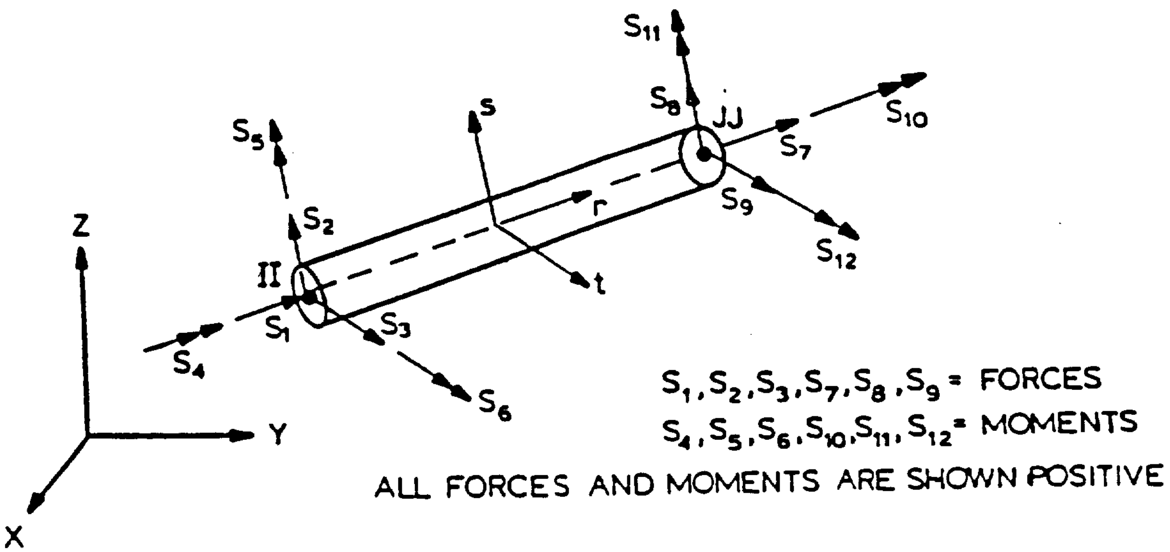

Figure A2 Beam Element End Forces and Moments

ELEMENT NUMBERING

DYNAMIC ANALYSIS OF DAEDALUS AIRFRAME

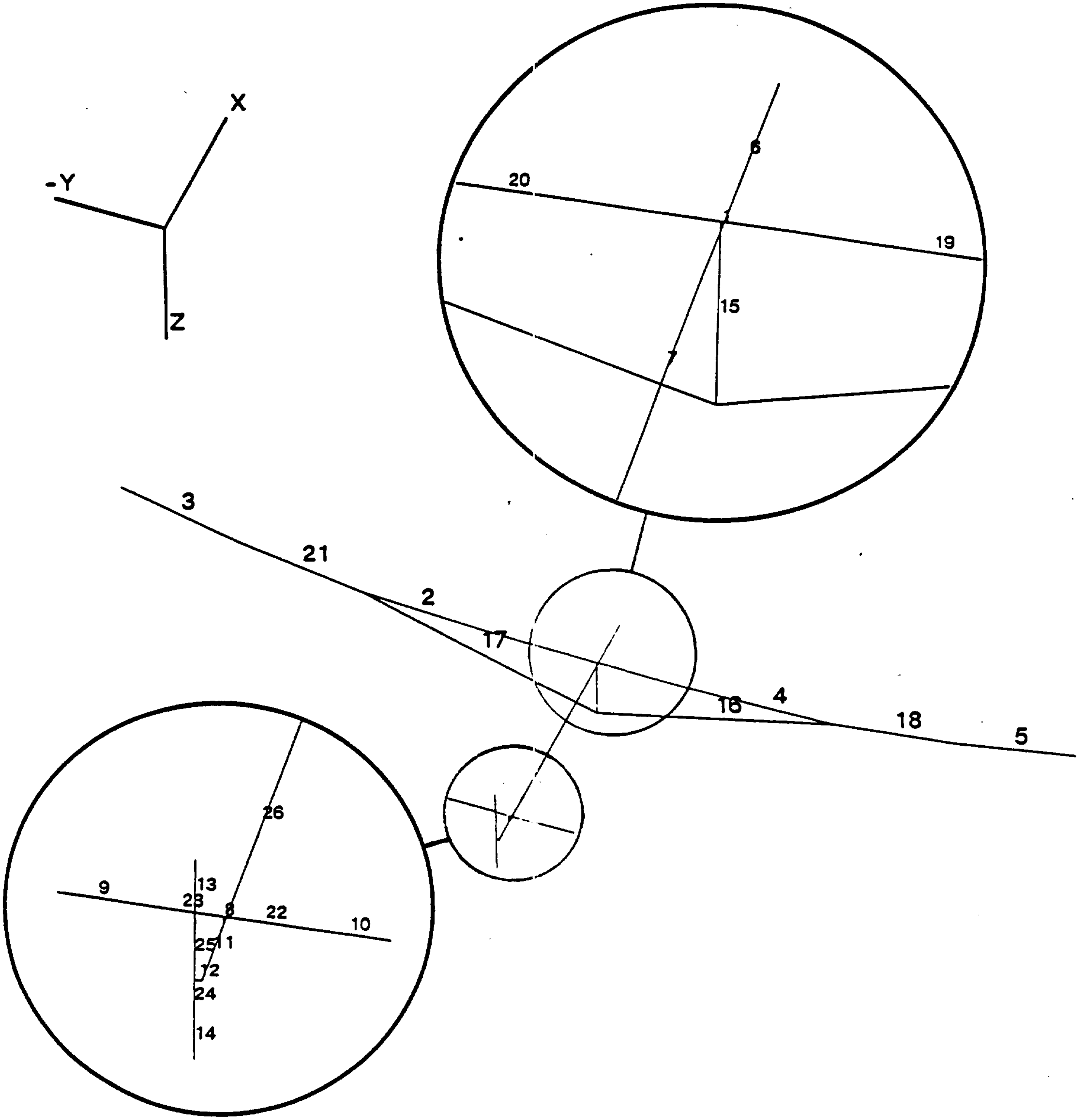

MODE SHAPE OF MODE 7 WITH FREQUENCY = 0.625 Hz
DYNAMIC ANALYSIS OF DAEDALUS AIRFRAME

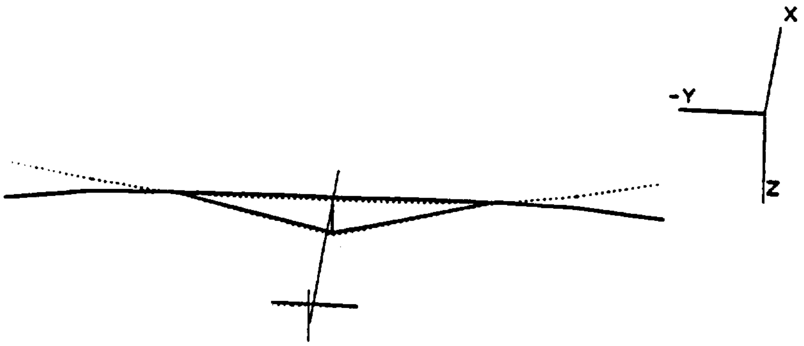

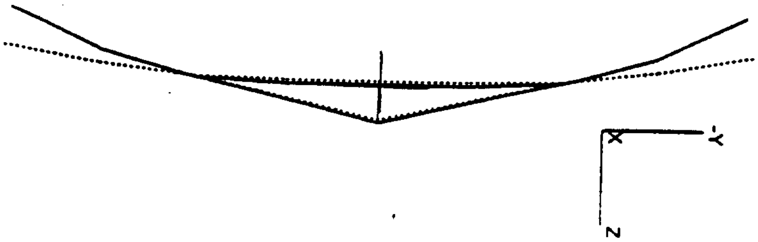

FRONT VIEW

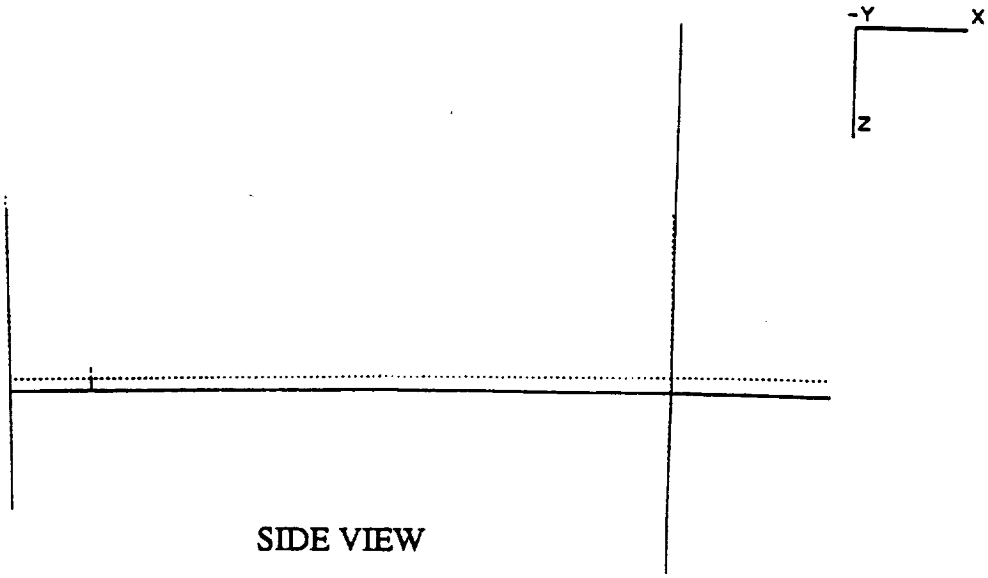

SIDE VIEW

MODE SHAPE OF MODE 8 WITH FREQUENCY = 0.838 Hz

DYNAMIC ANALYSIS OF DAEDALUS AIRFRAME

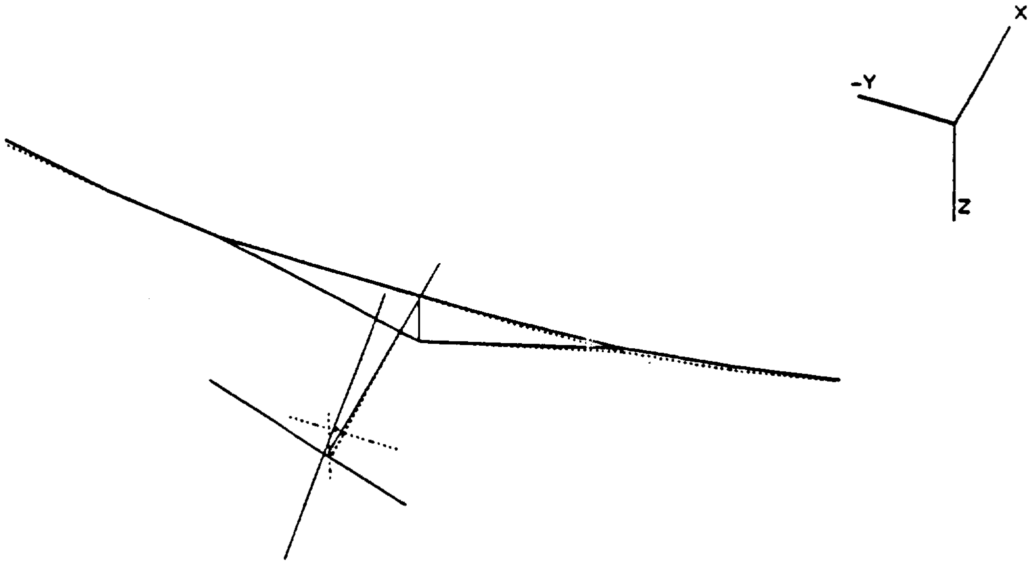

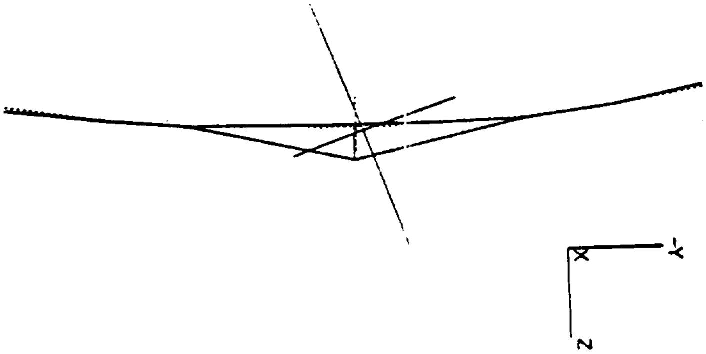

FRONT VIEW

MODE SHAPE OF MODE 8 WITH FREQUENCY - 0.985 Hz
DYNAMIC ANALYSIS OF DAEDALUS AIRFRAME

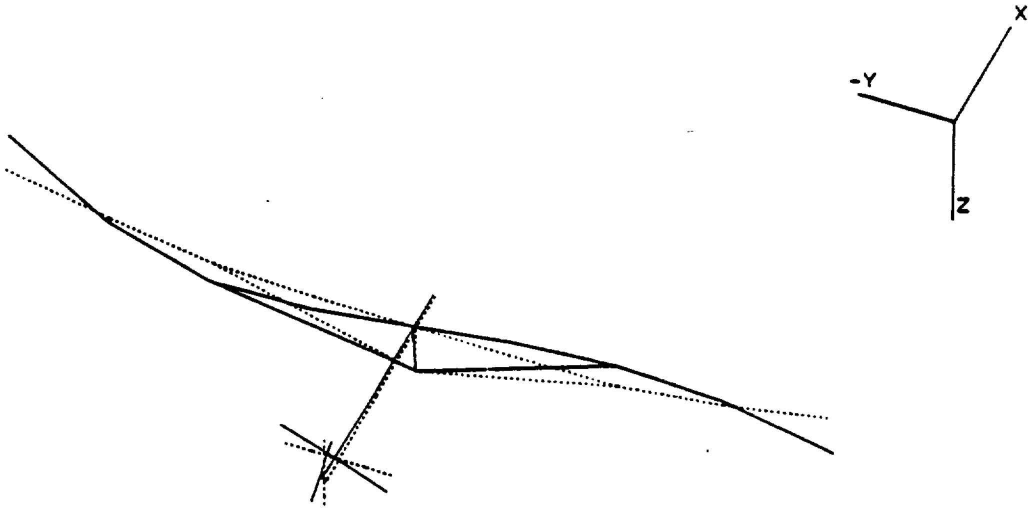

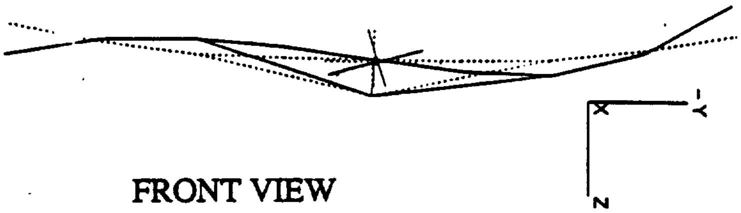

FRONT VIEW

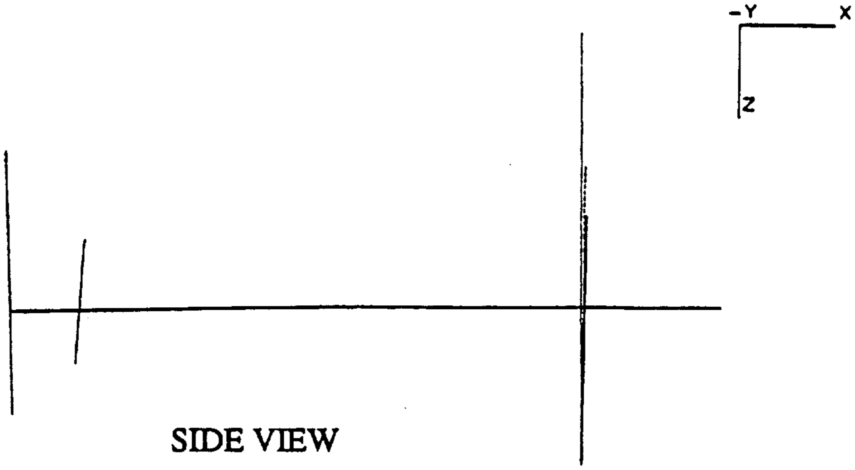

SIDE VIEW

MODE SHAPE OF MODE 10 WITH FREQUENCY - 1.352 Hz
DYNAMIC ANALYSIS OF DAEDALUS AIRFRAME

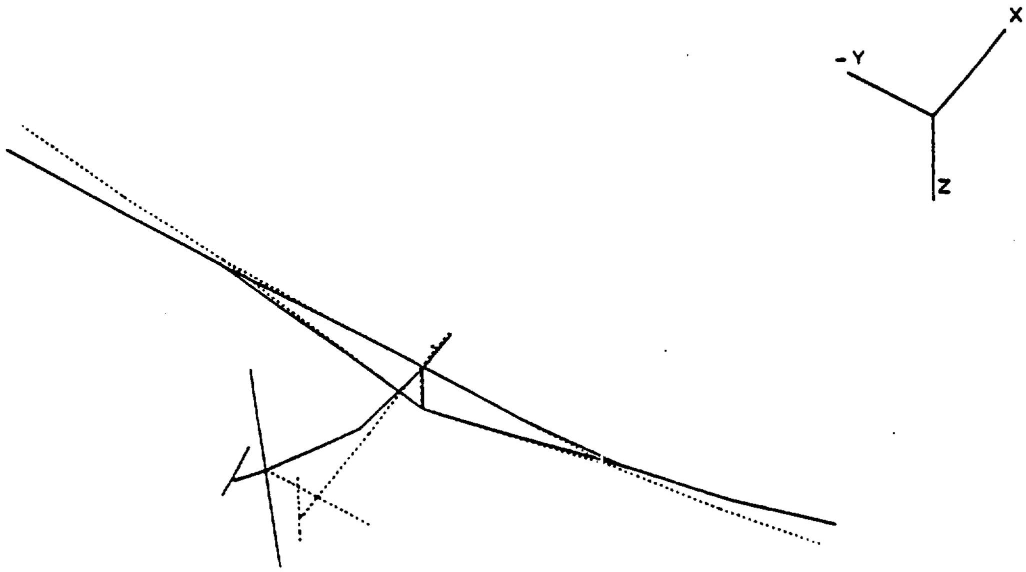

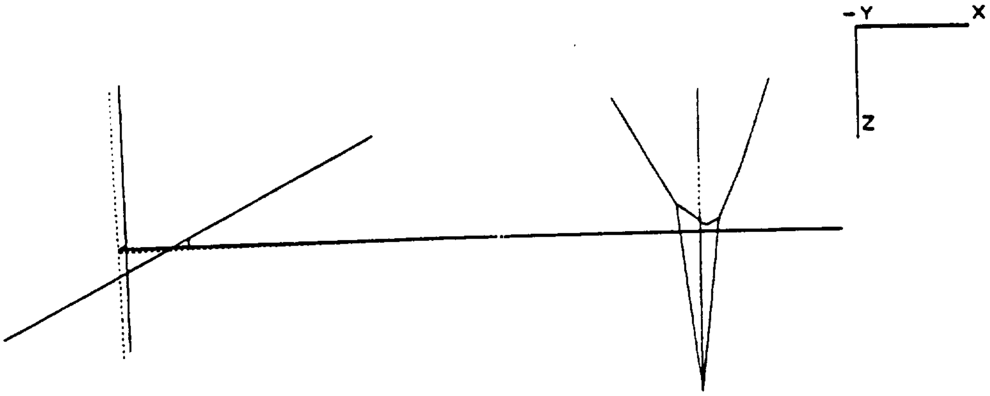

SIDE VIEW

MODE SHAPE OF MODE 11 WITH FREQUENCY - 1.552 Hz
DYNAMIC ANALYSIS OF DAEDALUS AIRFRAME

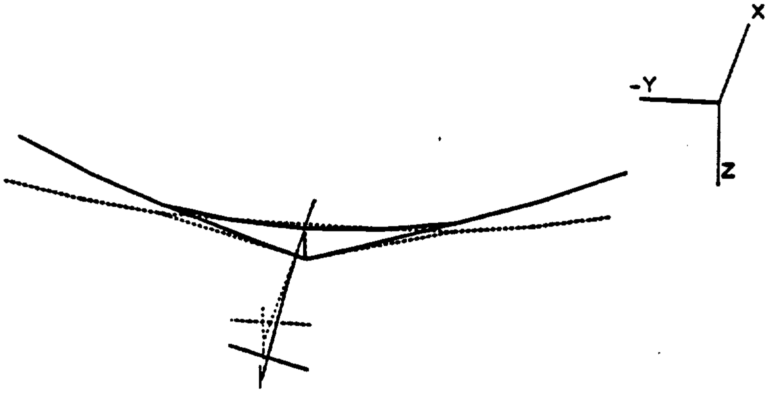

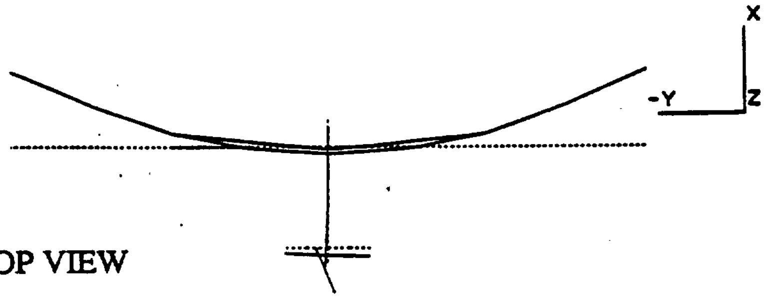

TOP VIEW

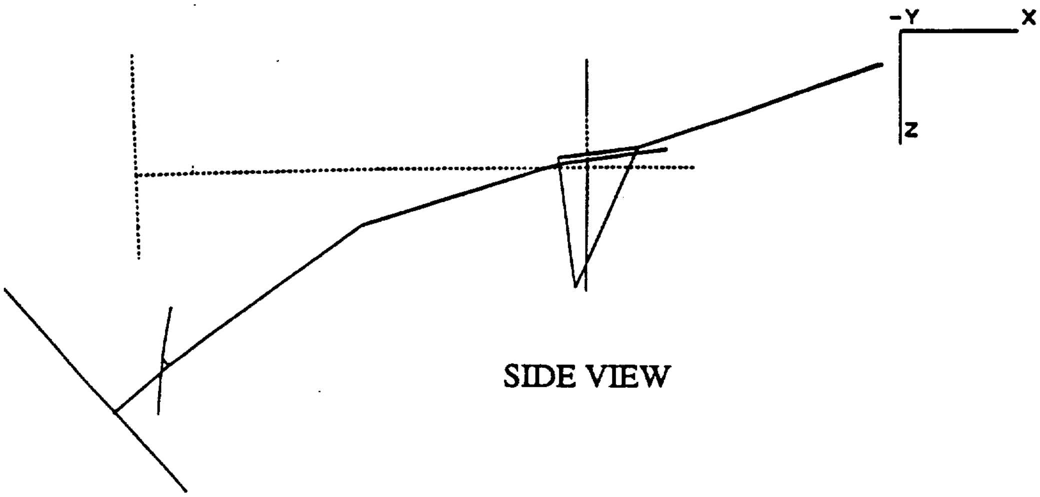

SIDE VIEW

MODE SHAPE OF MODE 12 WITH FREQUENCY - 2.547 Hz

DYNAMIC ANALYSIS OF DAEDALUS AIRFRAME

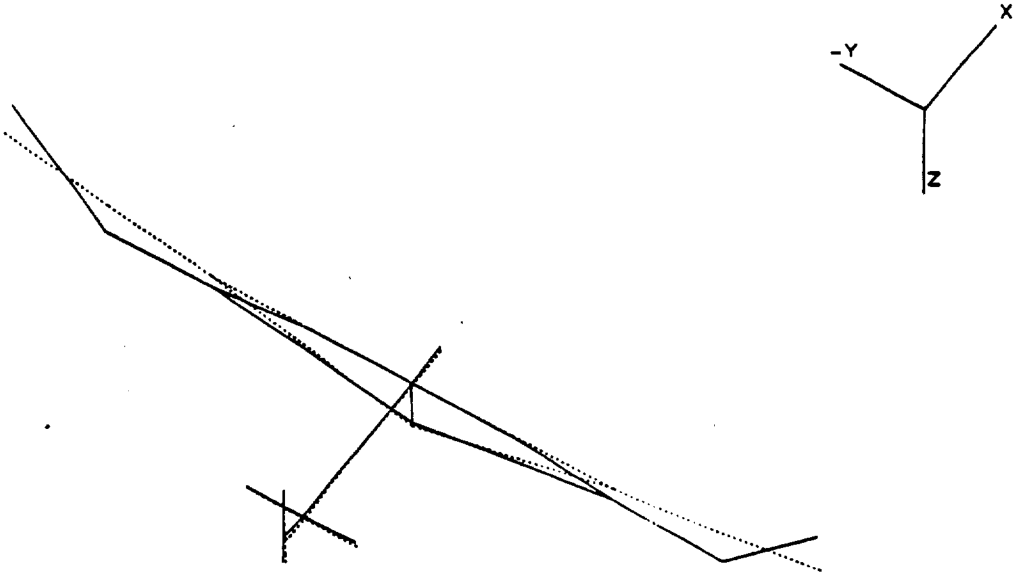

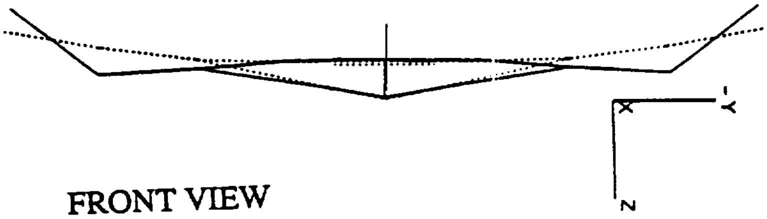

FRONT VIEW

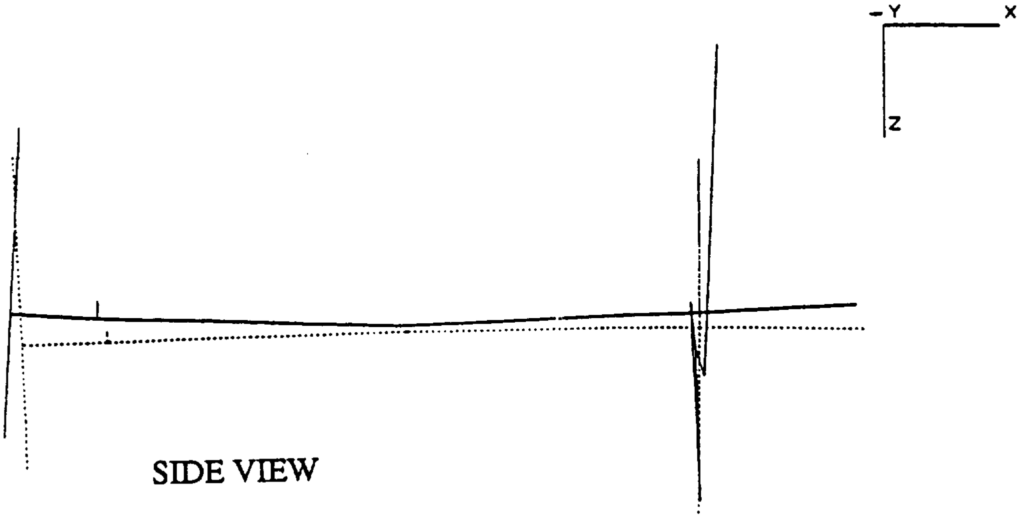

SIDE VIEW

MODE SHAPE OF MODE 13 WITH FREQUENCY - 2.824 Hz
DYNAMIC ANALYSIS OF DAEDALUS AIRFRAME

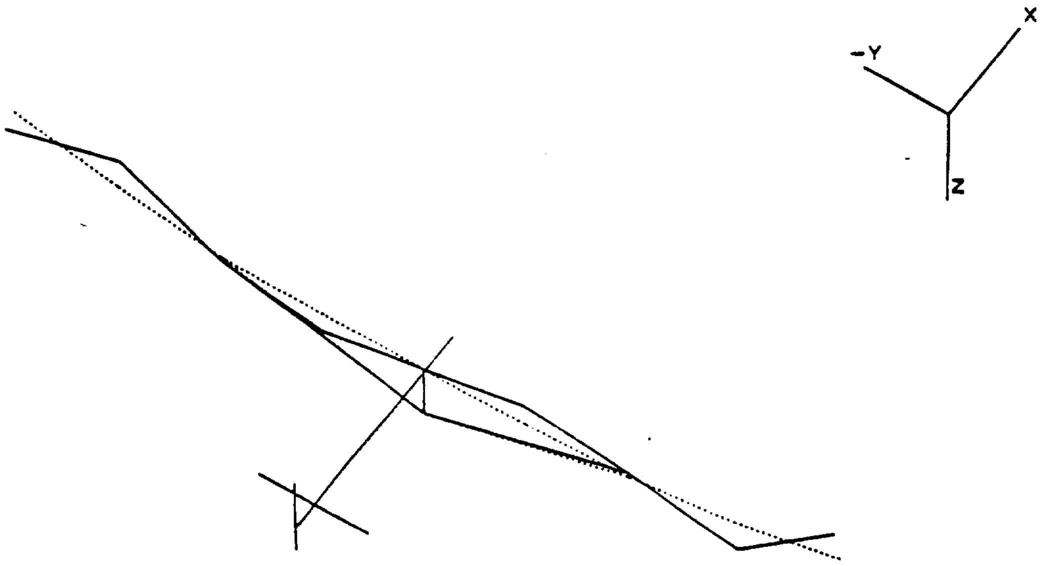

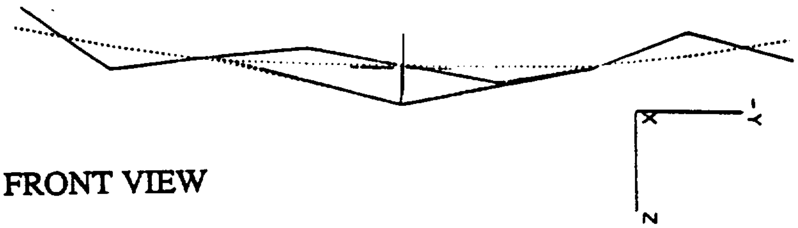

FRONT VIEW

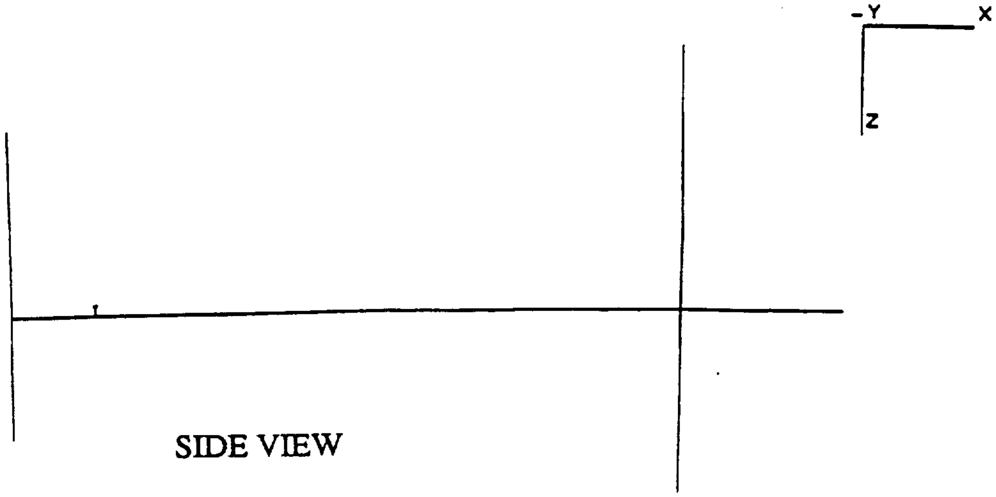

SIDE VIEW

MODE SHAPE OF MODE 14 WITH FREQUENCY = 2.998 Hz
DYNAMIC ANALYSIS OF DAEDALUS AIRFRAME

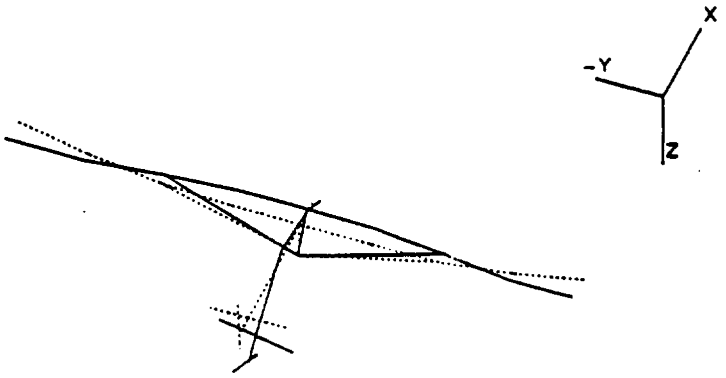

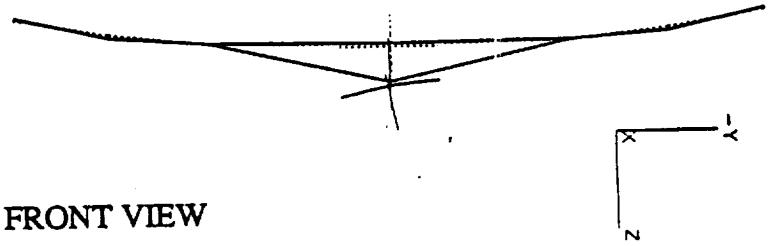

FRONT VIEW

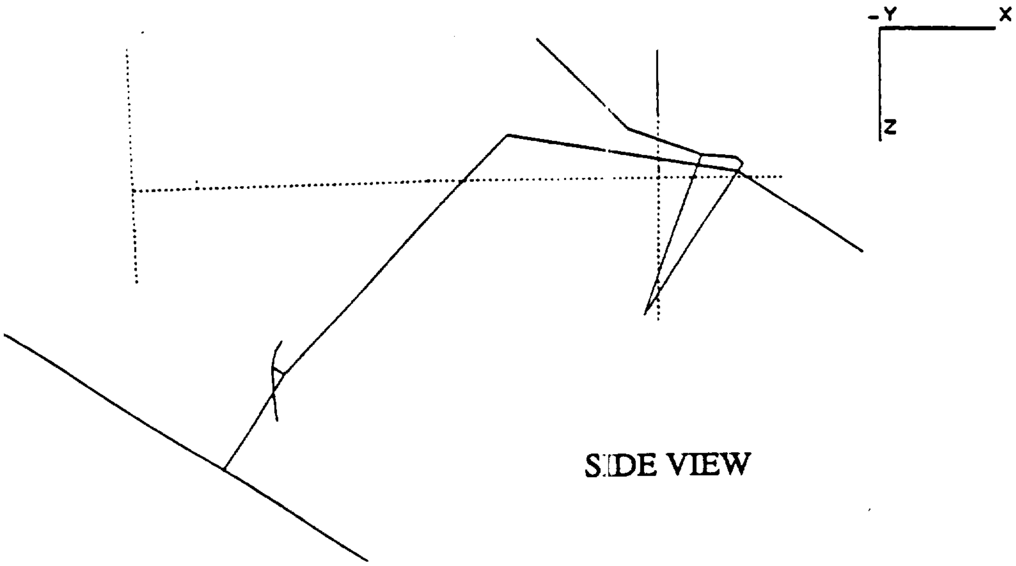

SIDE VIEW

MODE SHAPE OF MODE 15 WITH FREQUENCY = 3.904 Hz
DYNAMIC ANALYSIS OF DAEDALUS AIRFRAME

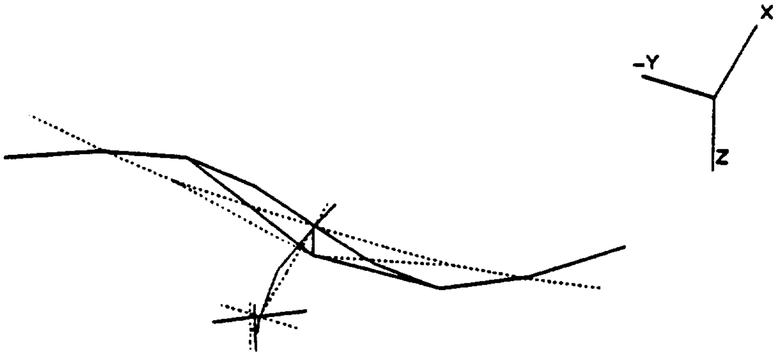

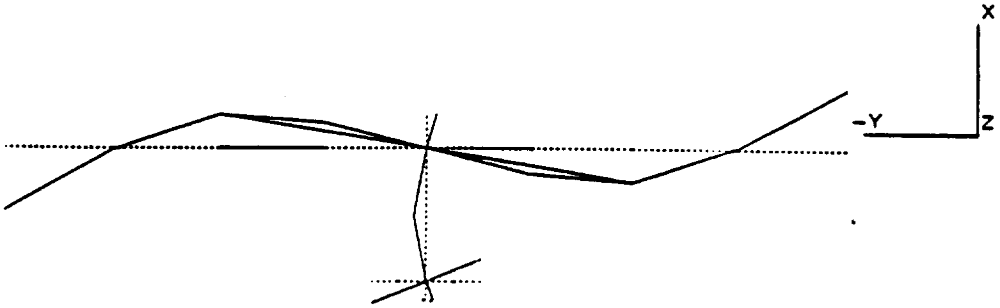

TOP VIEW

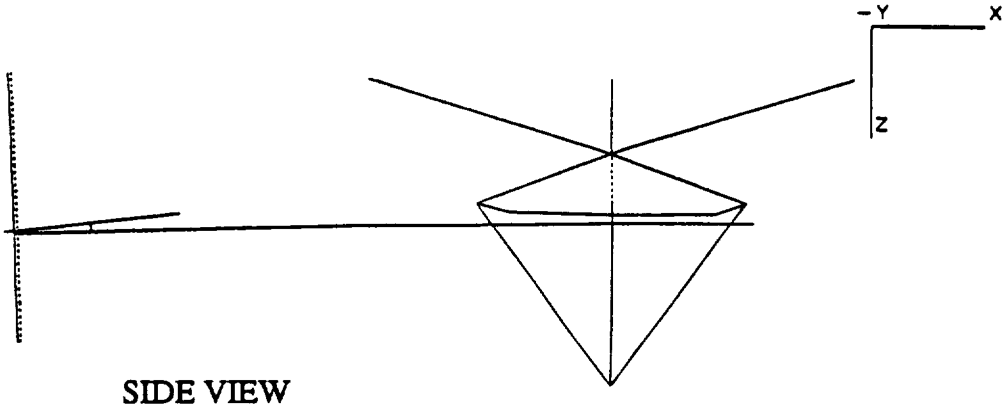

SIDE VIEW

Appendix C

Raw Data from Flights 307C, 307D, and 307E

Data From Flight 307C

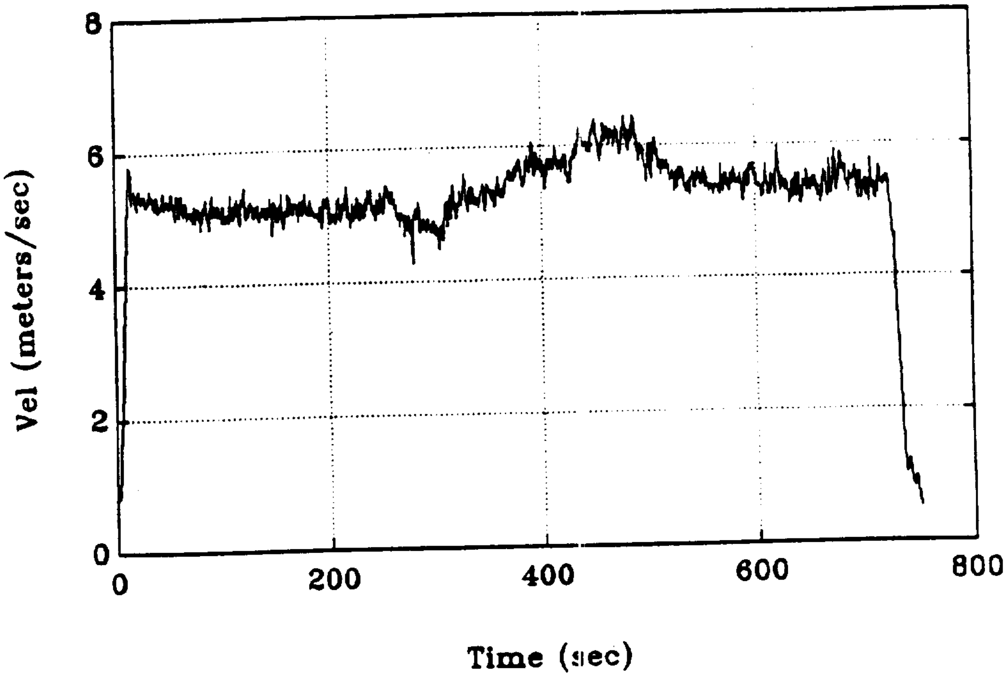

Vel (meters/sec)
0
2
4
6
8
0
200
400
600
800
Time (sec)

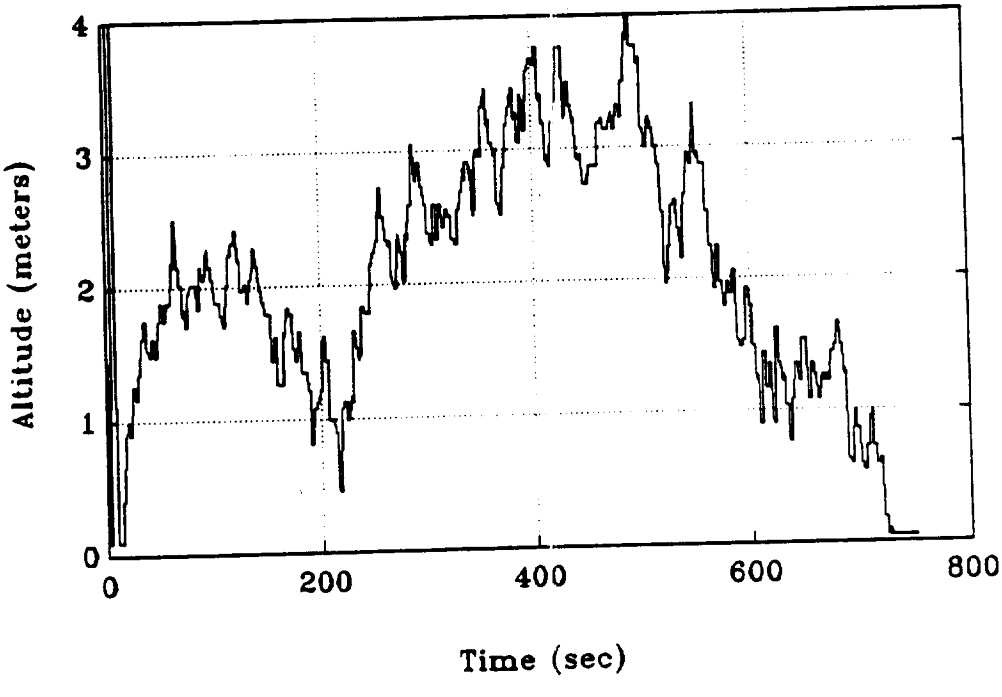

Altitude (meters)
0
1
2
3
4
0
200
400
600
800
Time (sec)

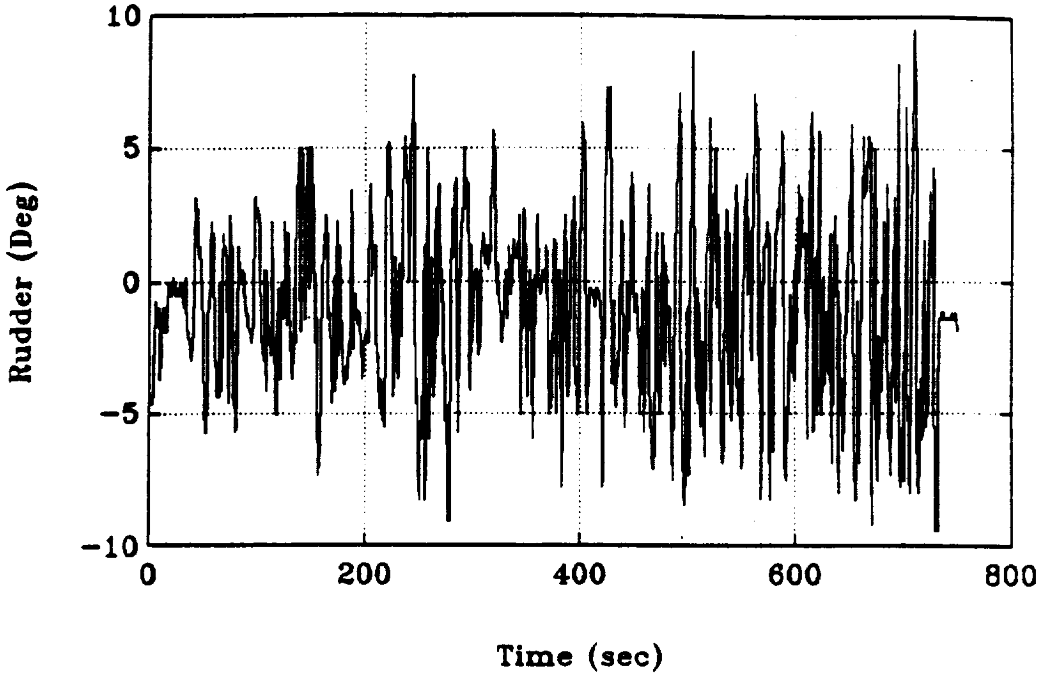
10
5
0
-5
-10
Rudder (Deg)
0
200
400
600
800
Time (sec)

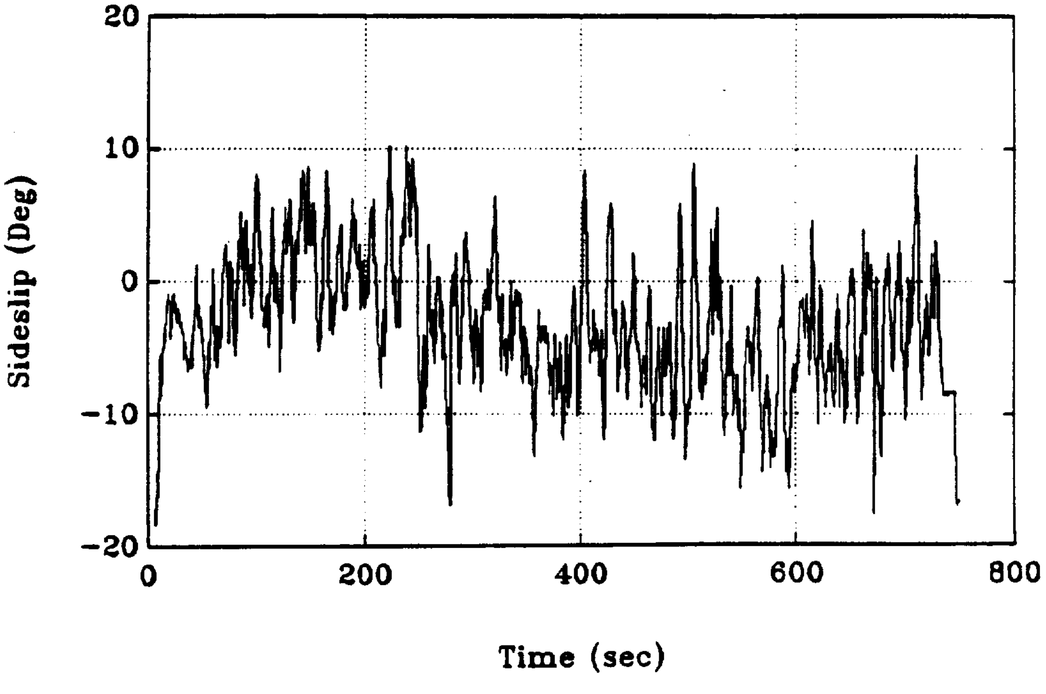
20
10
0
-10
-20
Sideslip (Deg)
0
200
400
600
800
Time (sec)

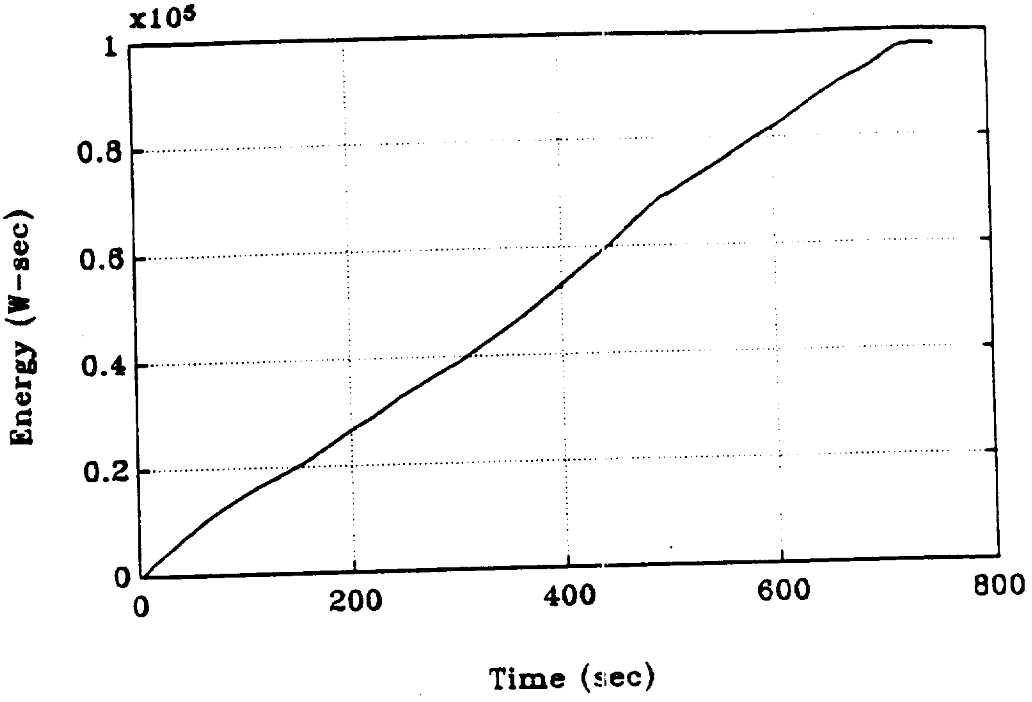
x10^5
1
0.8
0.6
0.4
0.2
0
Energy (W-sec)
0
200
400
600
800
Time (sec)

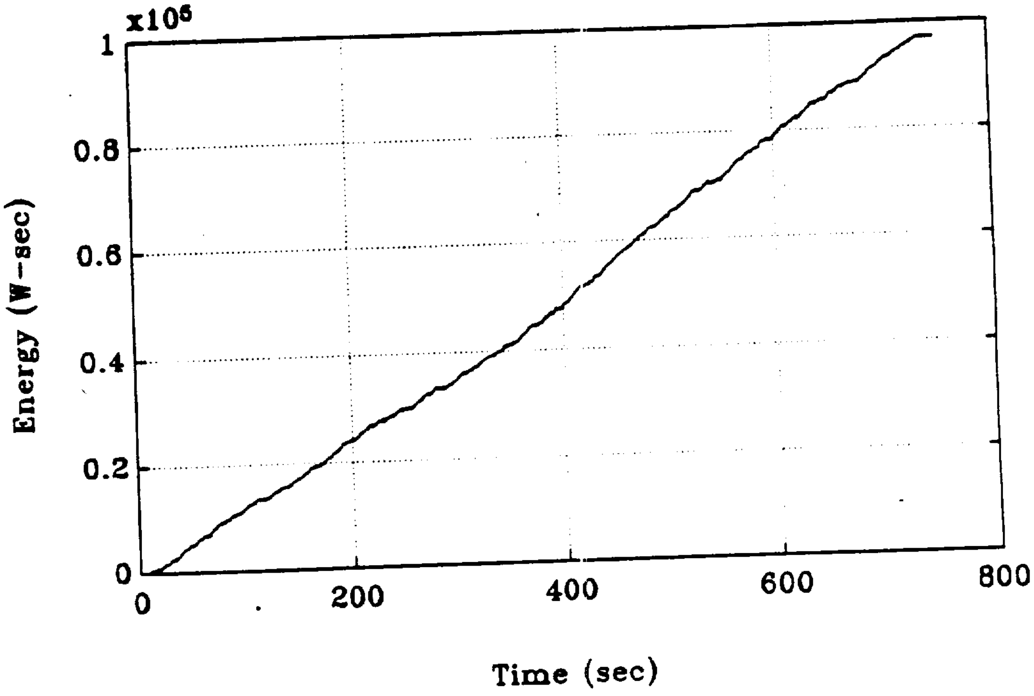
x10^5
1
0.8
0.6
0.4
0.2
0
Energy (W-sec)
0
200
400
600
800
Time (sec)

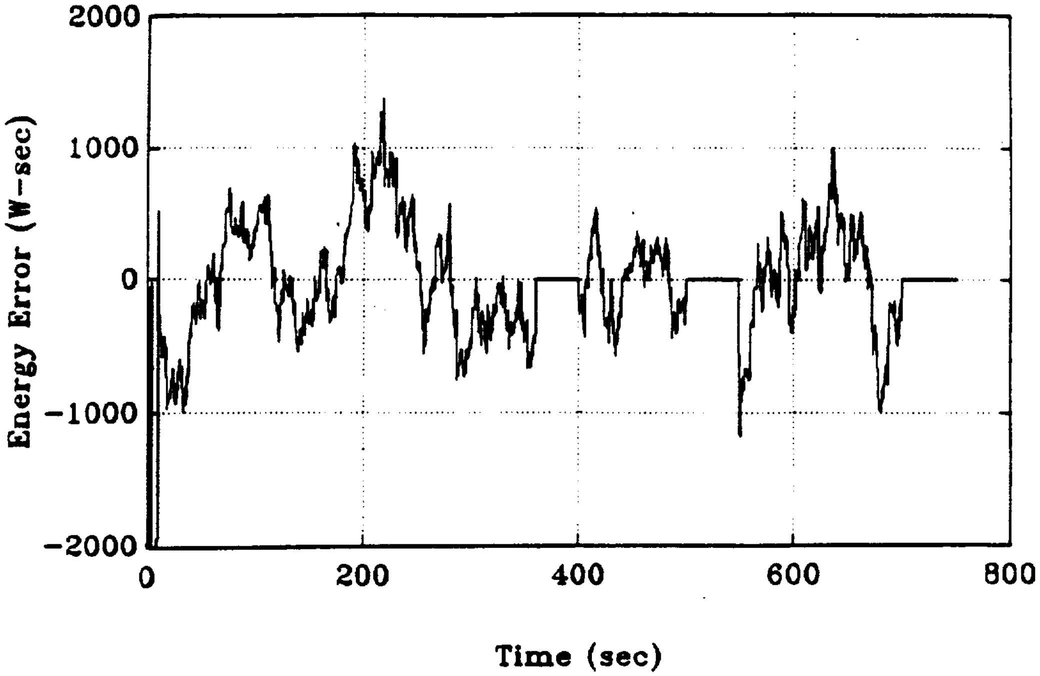

2000
1000
0
-1000
-2000
0
200
400
600
800
Energy Error (W-sec)
Time (sec)

Data From Flight 307D

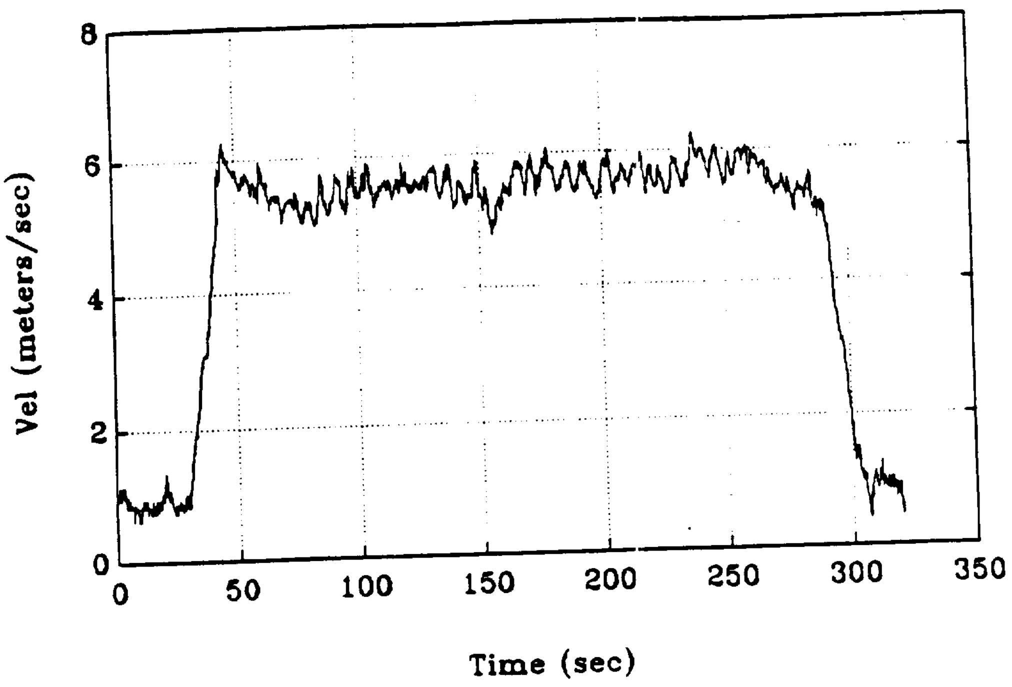
Vel (meters/sec)
0
2
4
6
8
0
50
100
150
200
250
300
350
Time (sec)

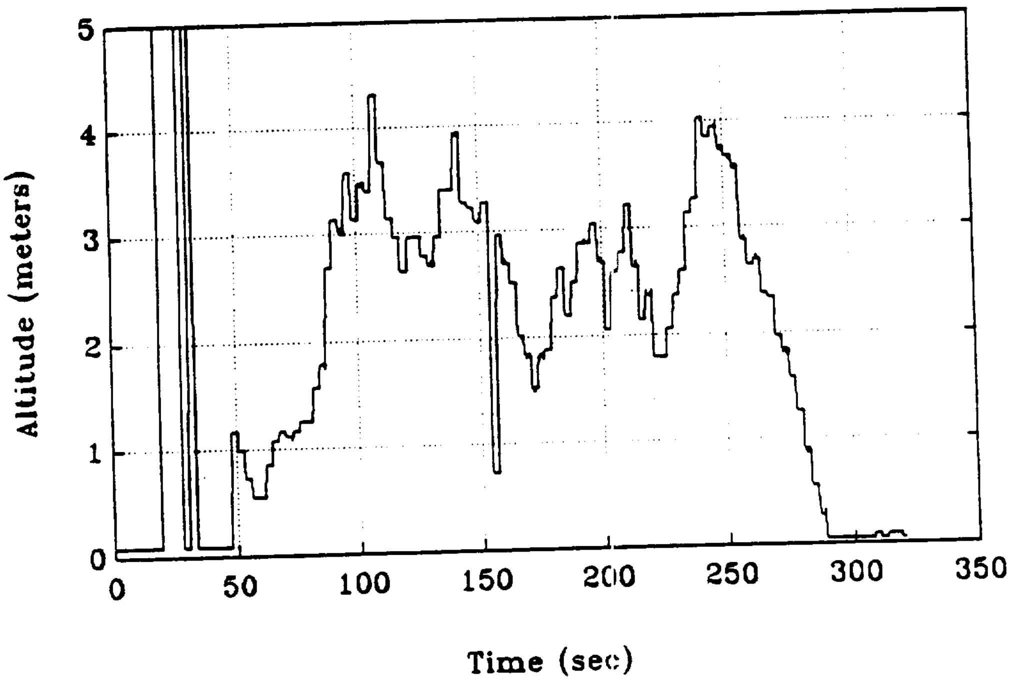
Altitude (meters)
0
1
2
3
4
5
0
50
100
150
200
250
300
350
Time (sec)

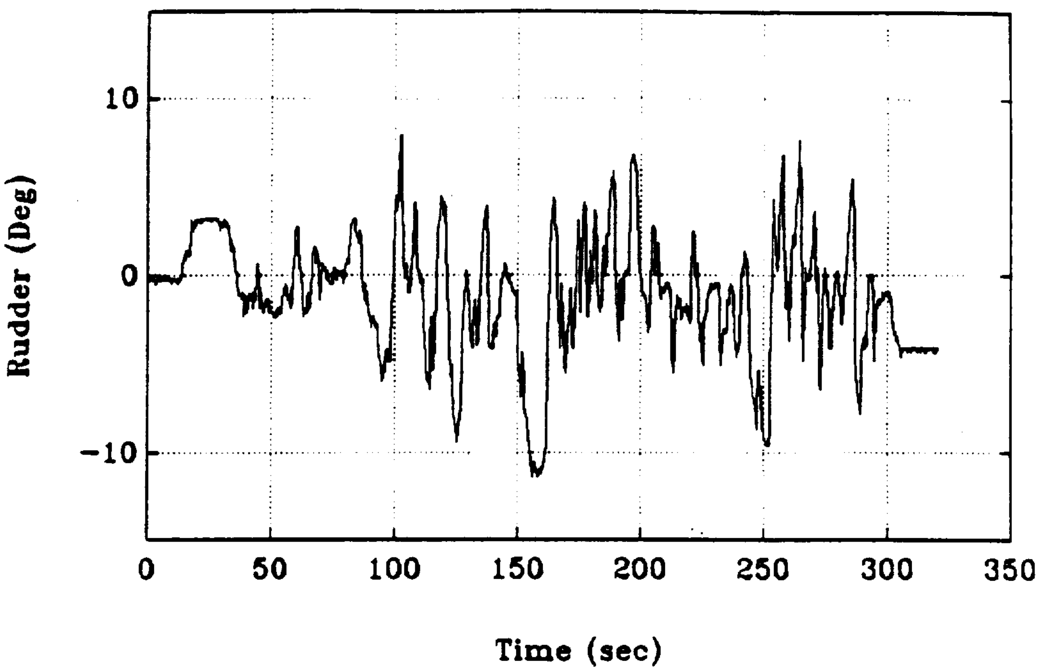
Rudder (Deg)
10
0
−10
0
50
100
150
200
250
300
350
Time (sec)

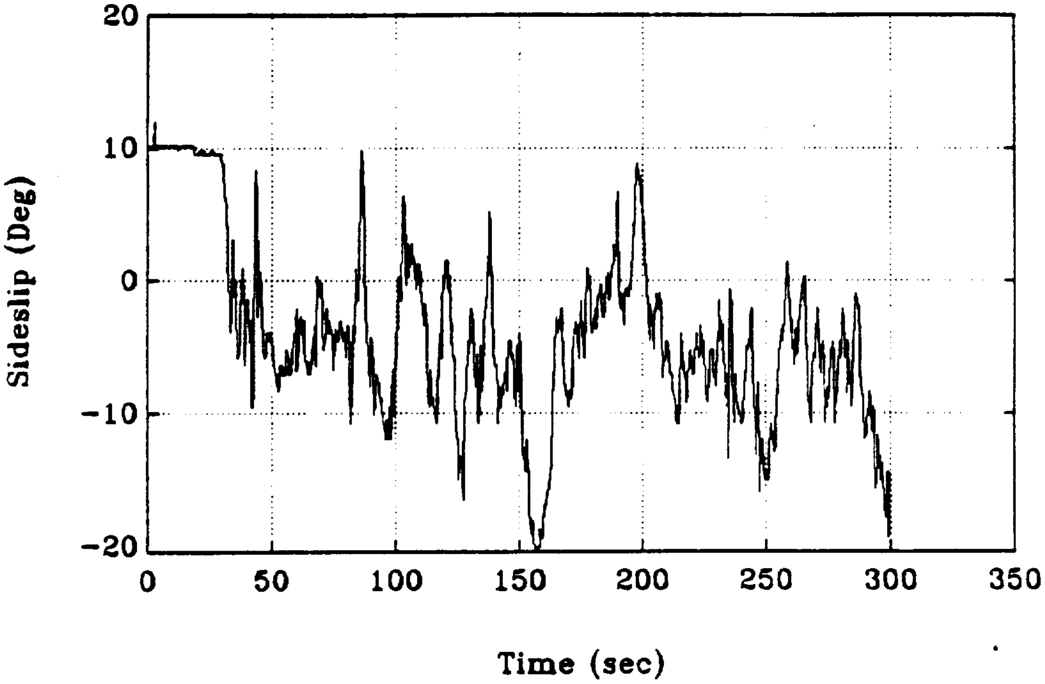
Sideslip (Deg)
20
10
0
−10
−20
0
50
100
150
200
250
300
350
Time (sec)

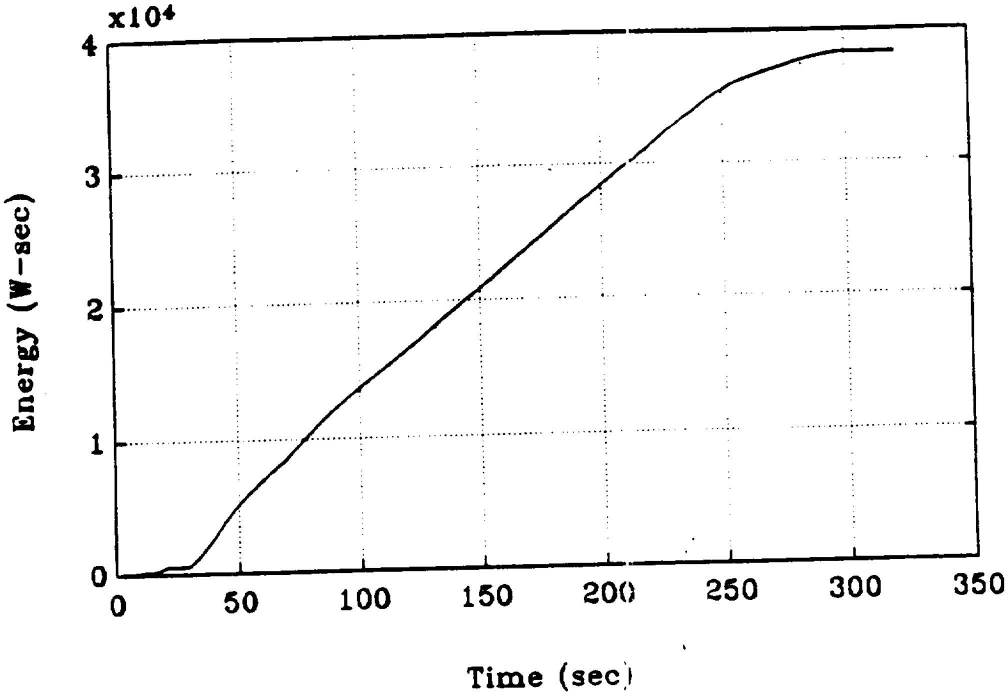
x10⁴
4
3
2
1
0
Energy (W-sec)
0
50
100
150
200
250
300
350
Time (sec)

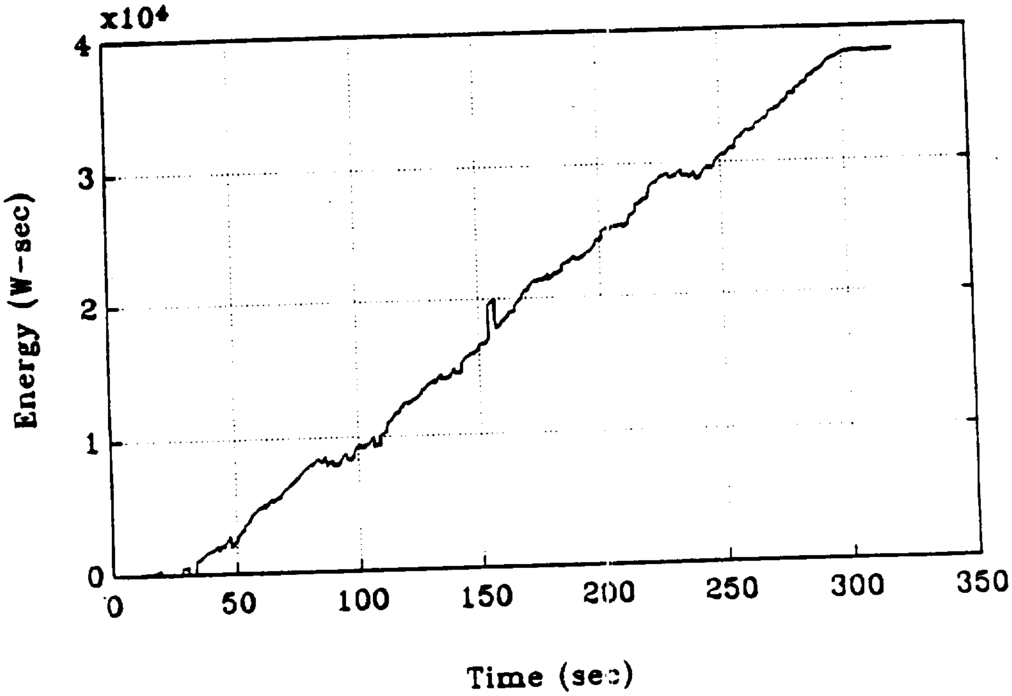
x10⁴
4
3
2
1
0
Energy (W-sec)
0
50
100
150
200
250
300
350
Time (sec)

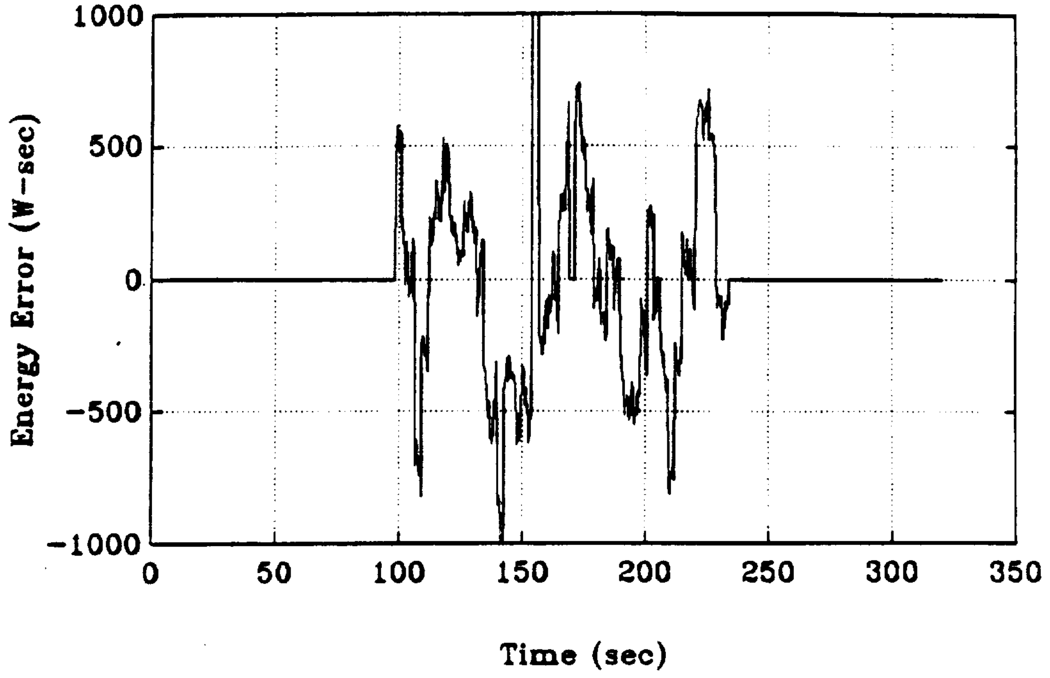

1000
500
0
-500
-1000
Energy Error (W-sec)
0
50
100
150
200
250
300
350
Time (sec)

Data From Flight 307E

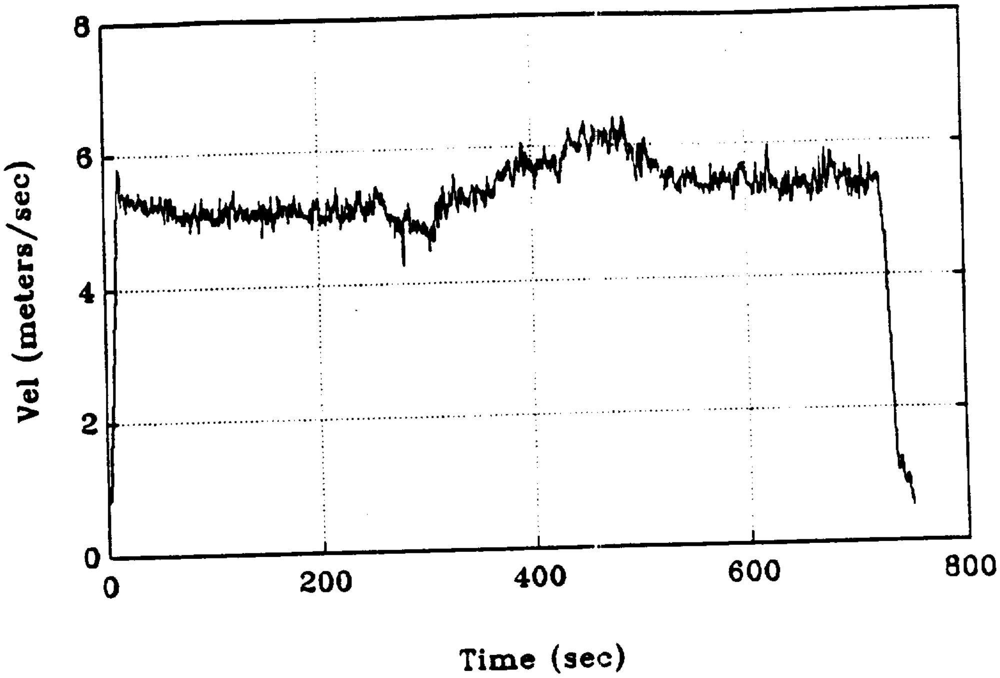

Vel (meters/sec)
0
2
4
6
8
0
200
400
600
800
Time (sec)

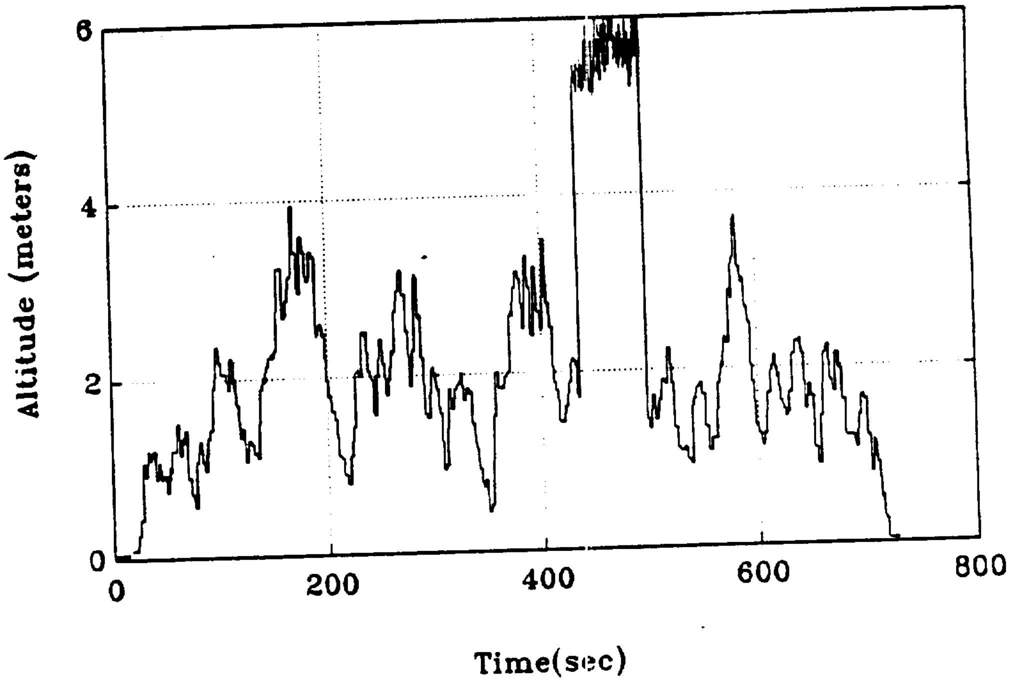

Altitude (meters)
0
2
4
6
0
200
400
600
800
Time(sec)

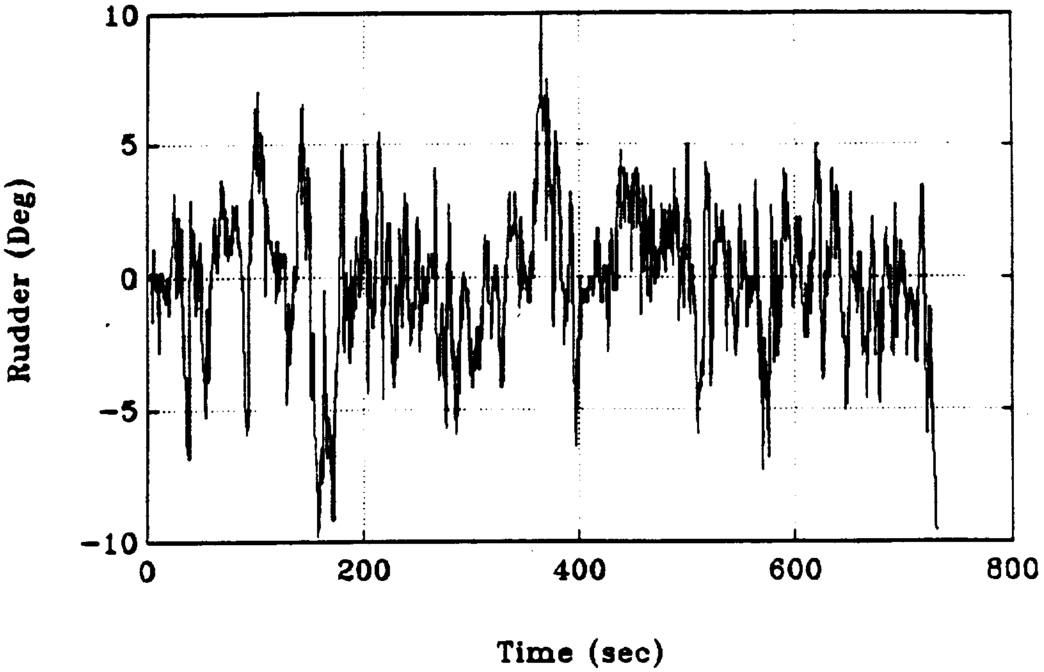

10
5
0
-5
-10
0
200
400
600
800
Rudder (Deg)
Time (sec)

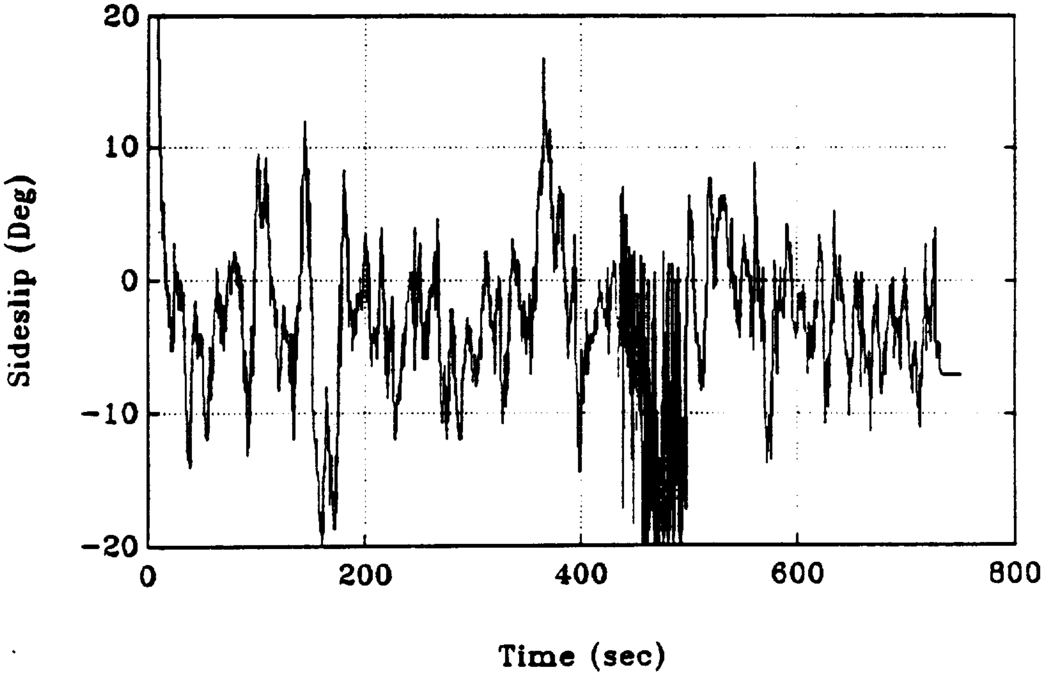

20
10
0
-10
-20
0
200
400
600
800
Sideslip (Deg)
Time (sec)

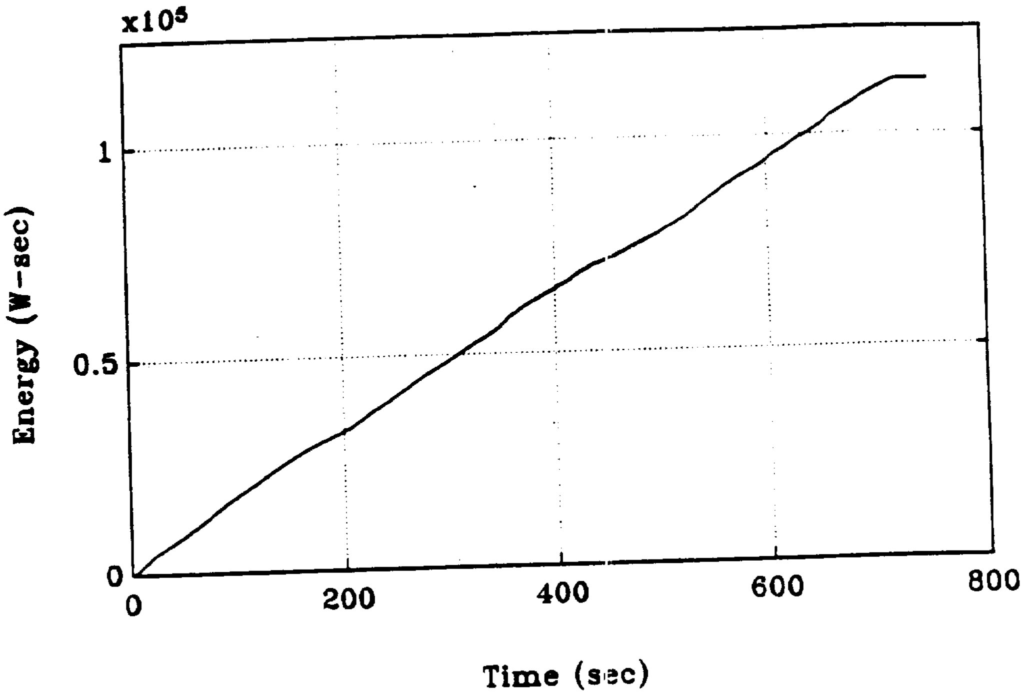
x10^5
Energy (W-sec)
1
0.5
0
0
200
400
600
800
Time (sec)

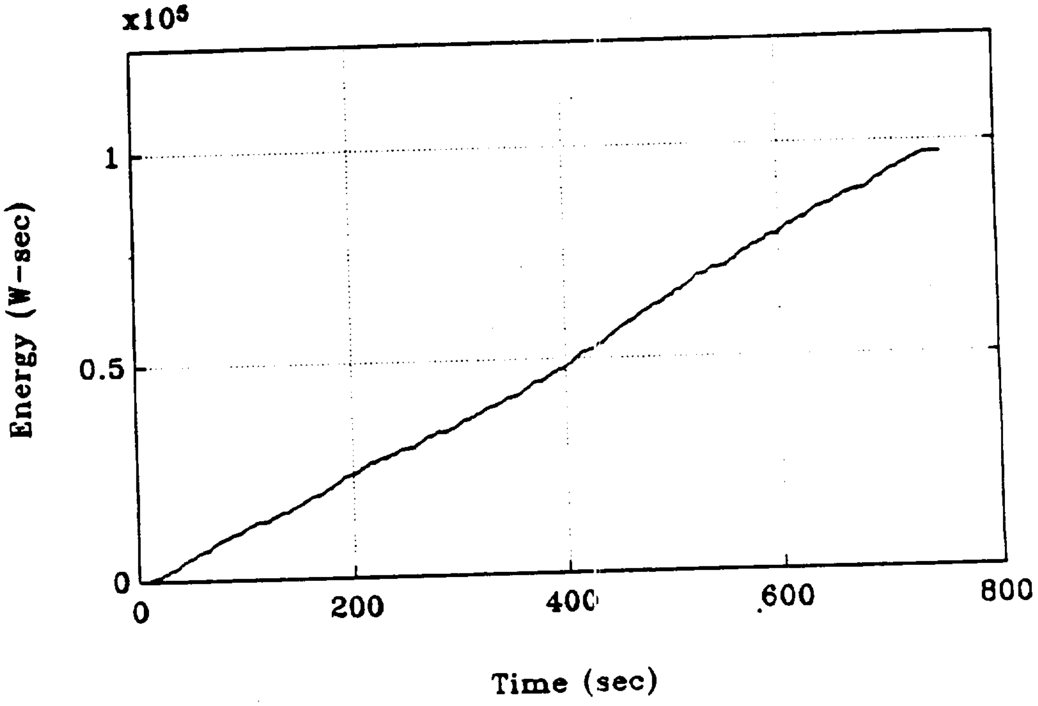
x10^5
Energy (W-sec)
1
0.5
0
0
200
400
600
800
Time (sec)

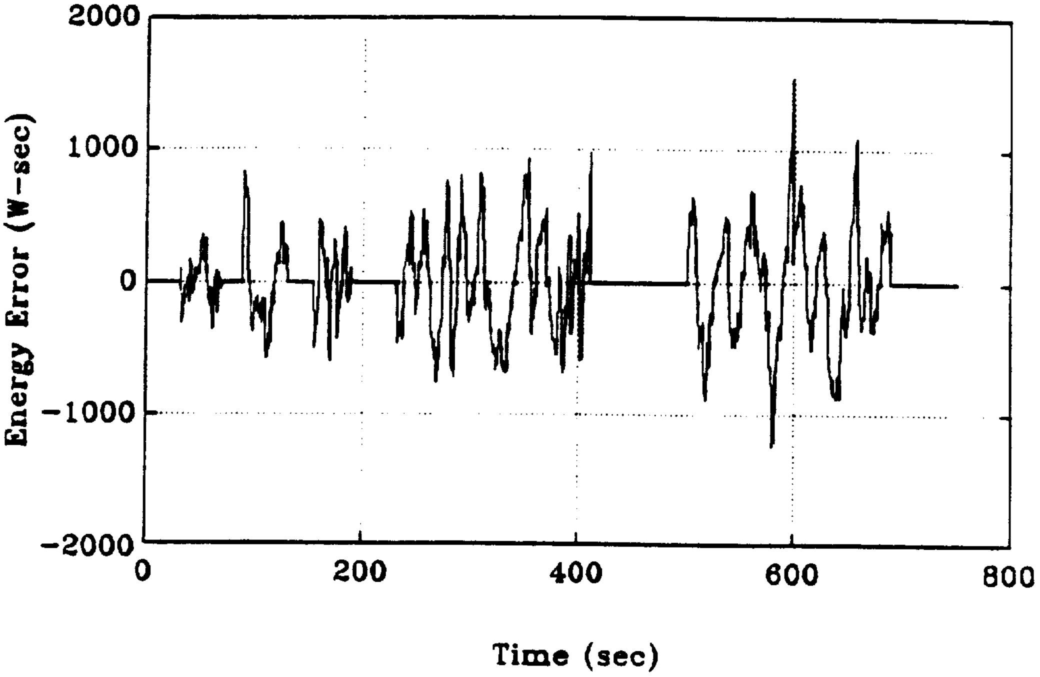
2000
1000
0
-1000
-2000
Energy Error (W-sec)
0
200
400
600
800
Time (sec)